Sapienza
Università di Roma

Scuola di Dottorato "Vito Volterra"
Dottorato di Ricerca in Fisica – XXII ciclo

Model of the Response Function of CUORE Bolometers

Thesis submitted to obtain the degree of
Doctor of Philosophy ("Dottore di Ricerca") in Physics
10 December 2009

by

Marco Vignati

Program Coordinator
Prof. Enzo Marinari

Thesis Advisor
Prof. Fernando Ferroni

Contents

Introduction

In the last decade much progress has been made in neutrino physics. Oscillation experiments provided a clearer picture of this elusive particle and we are now entering the era of precision measurements. There are however questions that cannot be addressed by oscillation experiments. The absolute mass scale of the neutrino is one of these, and it is considered a key quantity in many theories beyond the Standard Model of particle physics. Being only sensitive to squared mass differences, oscillation experiments are not able to measure this parameter.
Moreover, the mechanism responsible for the generation of neutrino masses is still unknown. Neutrinos are electrically neutral particles, and the only carried charge is that of weak interactions. In the Standard Model there is no symmetry requiring conservation of lepton number, even though a violation has never been observed. If lepton number is not conserved, neutrinos could be their own antiparticles, thus being Majorana particles.

The double beta decay without emission of neutrinos violates the lepton number by two units, and has never been observed. Observation of this nuclear decay would imply that lepton number is not conserved and that neutrinos are Majorana particles, a breakthrough in our understanding of nature. Moreover it could provide information on the absolute mass scale of neutrinos because a virtual neutrino is exchanged and the propagator is proportional to it.
Being a very rare process the experimental search for this decay demands a large amount of mass operating in low background conditions. Current limits on the half-life of this process range between 10^{21} and 10^{25} years, depending on the source isotope. Next generation experiments will improve the sensitivity to the half-life by two orders of magnitude with respect to the present imits.

This Ph.D. work was performed within the CUORE collaboration, which will be ready to start a 1-ton experiment within a couple of years. This experiment will probe neutrinoless double beta decay in ^{130}Te using TeO_2 bolometers.
Bolometers are calorimeters that operate at low temperatures, able to measure the temperature rise produced by the energy release of an impinging particle. The response function of these detectors is not yet fully understood. Measuring the energy deposited by a particle is complicated and the shape of the signal depends on the energy. Moreover the response function varies with operating temperature. This thesis concerns a study of the response function of TeO_2 bolometers, performed in order to build simulations of the detector and provide new data analysis tools with the aim of building the neutrinoless double beta decay measurement at CUORE.

This thesis is divided into five chapters. After an overview of neutrino physics, in chapter 1 the scientific motivations for the search of neutrinoless double beta decay are introduced, followed by a description of the experimental status. In chapter 2 the bolometric technique is described, the experimental technique used by the CUORE experiment to search for neutrinoless double beta decay. Chapter 3 is devoted to the development of a model of the response function of CUORE bolometers, that includes an understanding of the main sources of non linearities. In chapter 4 an algorithm to remove the non linearities is proposed. The data analysis based on this algorithm is compared with the standard analysis used so far with bolometers. In chapter 5 the analysis is repeated on a larger number of bolometers, including precision measurements of the model parameters.

Chapter 1

Neutrino masses and double beta decay

In 1914 Chadwick observed that the electrons emitted in β decays have a continuous spectrum, unlike what happens in α and γ decays. Nevertheless, if the decay products were only an electron and a nucleus, electrons would have necessarily a monochromatic spectrum. To overcome this paradox, Pauli proposed a 'desperate way out' to save energy conservation, introducing a new particle that was not detected in the decay, the "neutron". After that the true neutron was identified by Chadwick, the new particle was renamed by Fermi "neutrino" (ν).
Electron neutrinos were detected for the first time by Cowan and Reines in 1956 and found to be left-handed in 1957. The muon neutrino was discovered in 1962, while the tau neutrino was not discovered until 2000.

Great interest in neutrino physics was raised by the discovery of flavor non-conservation. The first hints for this phenomenon date back to the late '60, when a deficit in the solar neutrino flux was observed. It took about thirty years to completely understand that neutrinos change flavor along the path from the sun to the earth. This phenomenon, named "oscillation", was predicted by Pontecorvo in 1956 and shows that neutrinos have mass. Oscillations were then observed also in neutrinos produced in the atmosphere by cosmic rays and in neutrinos produced in nuclear reactors and accelerators.

In the last decade almost all oscillation parameters have been measured, giving a much clearer picture of neutrino physics. Most of the remaining open questions concerns its mass, which absolute value and nature cannot be determined by oscillation experiments. The search for neutrinoless double beta decay is currently the only experimental technique able to probe neutrino mass and nature.

1.1 Oscillations

The first indication of neutrino oscillations came from the Chlorine solar neutrino experiment conducted by Raymond Davis, Jr, in the Homestake mine in South Dakota [1]. This experiment observed only one third of the neutrinos coming from the sun predicted by the Standard Solar Model. The "solar neutrino problem", as it came to be known, was bolstered by the findings of the Gallium experiments

GALLEX [2] and SAGE [3]. Finally the SNO experiment confirmed that electron neutrinos were being converted into other neutrino flavors through the comparison of charged current reactions (sensitive only to ν_e) to neutral current reactions (sensitive to all three flavors) [4]. Finally, in 2002, the KamLAND collaboration published [5] the first observation of the oscillation effect in neutrinos emitted by nuclear reactors. The oscillation pattern is clearly visible in the last KamLAND publication (see figure 1.1).

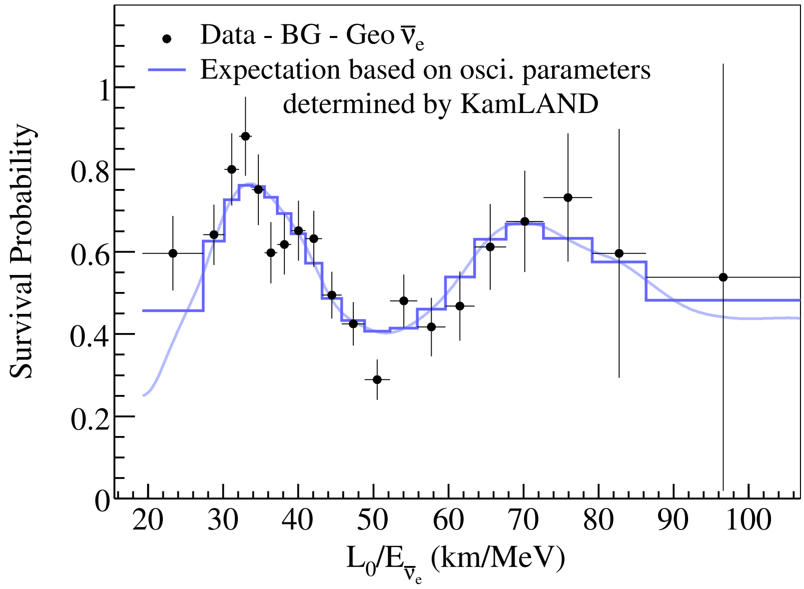

Figure 1.1. Electron anti-neutrino survival probability as a function of L/E measured by the KamLAND experiment. L_0 is the effective baseline taken as a flux-weighted average ($L_0 = 180\,\mathrm{Km}$). Picture taken from [6].

Moreover an anomaly in the atmospheric neutrino flux was observed by Super-Kamiokande [7]. The anomaly consisted in a difference between the flux of downward-going and upward-going ν_μ. The explanation for this observation is that the ν_μs were oscillating into ν_τs.

Neutrino oscillations occur because the weak flavor eigenstates (ν_e, ν_μ and ν_τ) are not aligned with the neutrino mass eigenstates (m_1, m_2 and m_3). Flavor eigenstates $|\nu_f\rangle$ are related to mass eigenstates $|\nu_k\rangle$ by the Pontecorvo-Maki-Nakagawa-Sakata (PMNS) neutrino mixing matrix:

$$|\nu_f\rangle = \sum_{k=1}^{3} U^*_{fk}\,|\nu_k\rangle\,, \qquad f=(e,\mu,\tau), \quad k=(1,2,3) \quad . \tag{1.1}$$

The PMNS matrix U_{fk} can be parameterized as [8]:

$$
\begin{aligned}
U &= \begin{bmatrix} 1 & 0 & 0 \\ 0 & c_{23} & s_{23} \\ 0 & -s_{23} & c_{23} \end{bmatrix} \times \begin{bmatrix} c_{13} & 0 & s_{13}e^{-i\delta} \\ 0 & 1 & 0 \\ -s_{13}e^{i\delta} & 0 & c_{13} \end{bmatrix} \times \begin{bmatrix} c_{12} & s_{12} & 0 \\ -s_{12} & c_{12} & 0 \\ 0 & 0 & 1 \end{bmatrix} \\
&\times \begin{bmatrix} e^{i\phi_1/2} & 0 & 0 \\ 0 & e^{i\phi_2/2} & 0 \\ 0 & 0 & 1 \end{bmatrix} .
\end{aligned}
\tag{1.2}
$$

where s_{12} and c_{12} indicate $\sin\theta_{12}$ and $\cos\theta_{12}$ for example. The angles θ_{12}, θ_{23} and θ_{13} are known as the mixing angles, and the parameter δ is a phase which account for the CP violation. In addition the parameters ϕ_1 and ϕ_2 are Majorana phases. These phases can also violate CP, but they are not observable in neutrino oscillations.

In the simple case with only two neutrino flavors (ν_f,ν'_f) and two mass eigenstates (ν_1,ν_2) the mixing matrix can be expressed in terms of a single mixing angle θ without phases (CP violation can occur only when there are three or more states). In this approximation the probability of detecting a neutrino with flavor f' at a distance L from the source, where they were produced with flavor f, is:

$$
P(\nu_f \to \nu_{f'};\, t) \;=\; \sin^2 2\theta \, \sin^2\left(\frac{\Delta m^2}{4E} L\right) \tag{1.3}
$$

where $\Delta m^2 = m_2^2 - m_1^2$ and E is the neutrino energy. As this equation clearly shows, oscillation experiments can extract the mixing angles and the squared mass differences but not the absolute mass value. The current results are summarized in table 1.1, where it can be seen that the two mass splittings, as well as two over the three mixing angles have been measured with reasonable precision, while the small mixing angle θ_{13} is compatible with zero. If this angle vanishes the mixing matrix could be reduced to two independent 2×2 matrices, excluding the possibility of CP violation with neutrinos.

Table 1.1. Measured oscillation parameters [9].

Oscillation Parameter			Value
solar mass splitting	Δm^2_{21}	$=$	$7.65^{+0.23}_{-0.20} \times 10^{-5}\,\mathrm{eV}^2$
atmospheric mass splitting	$\lvert\Delta m^2_{23}\rvert$	$=$	$2.40^{+0.12}_{-0.11} \times 10^{-3}\,\mathrm{eV}^2$
solar mixing angle	$\sin^2\theta_{12}$	$=$	$0.304^{+0.022}_{-0.016}$
atmospheric mixing angle	$\sin^2\theta_{23}$	$=$	$0.50^{+0.07}_{-0.06}$
'CHOOZ' mixing angle	$\sin^2\theta_{13}$	$=$	$0.010^{+0.016}_{-0.011}$

While the solar mass splitting is known with sign (e.g. $m_2 > m_1$), the atmospheric mass splitting is known only as absolute value. This implies that we do not know if the mass hierarchy is normal ($m_3 > m_{1,2}$), following the pattern of the charged leptons, or inverted ($m_3 < m_{1,2}$). These possible scenarios are depicted in figure 1.2.

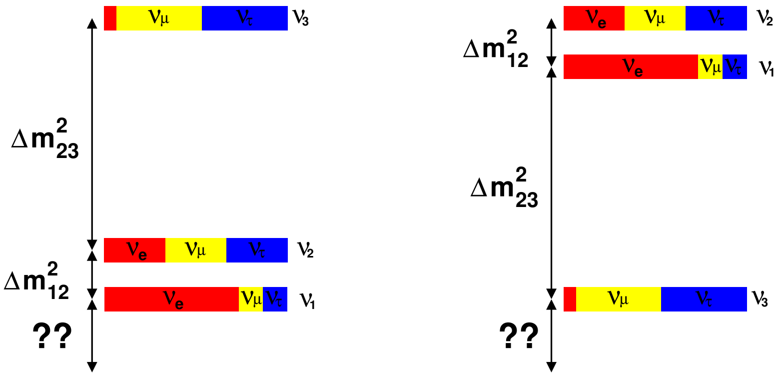

(a) normal hierarchy (b) inverted hierarchy

Figure 1.2. Neutrino mass hierarchies. The colored bands represent the contribution of each flavor to the mass eigenstate. The absolute mass scale is still unknown.

1.2 Masses

Even if the mass differences between neutrino states have been measured, the absolute values are still unknown. Limits on absolute neutrino masses come from cosmological constraints and from non oscillation experiments. Non oscillation experiments are mainly based on two methods. One method is the double beta decay and will be discussed later. The other method consist in the study of the endpoint of the beta decay spectrum, where the finite mass of the neutrino modifies the shape of the spectrum. The parameter that β-decay experiments measure is:

$$m_\beta^2 \;=\; \sum_{i=1}^{3} |U_{ei}|^2 m_i^2 \;. \tag{1.4}$$

Current best limits on m_β come from the Mainz [10] and Troitsk [11] tritium β-decay experiments ($m_\beta < 2.1\,\mathrm{eV}$). Next generation experiments plan to further constraint m_β in the sub-eV range, studying β-decay of tritium (KATRIN [12]) and ^{187}Re (MARE [13]).
Cosmological constraints on neutrino masses come from the observation of the Cosmic Microwave Background anisotropies and from the study of large scale structures. These observations are sensitive to the sum of the three neutrino masses. Limits range from few eV to few hundreds of meV, depending on the data being considered. However these constraints are less trustworthy, as they depend on cosmological models.

From the theoretical point of view the neutrino is a massless particle in the Standard Model of particle physics, as there was no evidence for neutrino masses when this theory was formulated. Oscillation experiments have now changed this scenario, calling for an extension of the theory. The mass can be included as a Dirac mass term, as for all other fermions:

$$\mathcal{L}^{\mathrm{D}}_{\mathrm{mass}} = -m_D\, \overline{\nu_R}\, \nu_L + \mathrm{H.c.} \tag{1.5}$$

where m_D is the Dirac mass that couple left-handed and right-handed neutrino. However, once the right-handed neutrino is introduced, due to the lack of electric charge, there is no reason not to include a Majorana mass term, where the neutrino is coupled to its charge conjugate:

$$\mathcal{L}^{\mathrm{M}}_{\mathrm{mass}} = \frac{1}{2}\, M_R\, \nu_R^T\, \mathcal{C}^\dagger\, \nu_R + \mathrm{H.c.} \tag{1.6}$$

where M_R is the Majorana mass term and $\mathcal{C}$ is the charge conjugation operator. The Majorana mass term for ν_L is not allowed by the symmetries of the Standard Model because it is not invariant under $\mathrm{SU}(2)_L \times \mathrm{U}(1)_Y$ transformations. On the other hand, the Majorana mass term for ν_R is allowed, being ν_R a singlet of $\mathrm{SU}(3)_C \times \mathrm{SU}(2)_L \times \mathrm{U}(1)_Y$. Therefore a Dirac-Majorana mass term:

$$\mathcal{L}^{\mathrm{D+M}}_{\mathrm{mass}} = \mathcal{L}^{\mathrm{D}}_{\mathrm{mass}} + \mathcal{L}^{\mathrm{M}}_{\mathrm{mass}} \tag{1.7}$$

is allowed in the Standard Model. In order to understand the implications of the Dirac-Majorana mass term, it is useful to define the column matrix of left-handed chiral fields:

$$N_L = \begin{pmatrix} \nu_L \\ \nu_R^c \end{pmatrix} \tag{1.8}$$

so that $\mathcal{L}^{\mathrm{D+M}}_{\mathrm{mass}}$ can be rewritten as

$$\mathcal{L}^{\mathrm{D+M}}_{\mathrm{mass}} = \frac{1}{2} N_L^T\, \mathcal{C}^\dagger\, M\, N_L + \mathrm{H.c.} \tag{1.9}$$

with

$$M = \begin{pmatrix} 0 & m_D \\ m_D & M_R \end{pmatrix}\ . \tag{1.10}$$

While both Majorana and Dirac mass terms are not excluded by any symmetry arguments, it is natural to ask the question why the neutrino is so much lighter than the other fermions. The See-saw mechanism provides a compelling mechanism to account for this discrepancy (for a detailed description see for example [18]). While the Dirac mass m_D, being generated by the Higgs mechanisms, is expected to be of the same order of magnitude of other fermions, there are no bounds for the Majorana mass M_R. In particular it can assume arbitrarily large values. If $M_R \gg m_D$ the two mass eigenstates of the Lagrangian (1.9) are:

$$\begin{aligned} \nu_1 &\simeq \nu_L, \qquad m_1 \simeq \tfrac{m_D^2}{M_R} \\ \nu_2 &\simeq \nu_R^c, \qquad m_2 \simeq M_R\ . \end{aligned} \tag{1.11}$$

If this condition is verified, the heavy neutrino ν_2 is predominantly ν_R^c and the light neutrino ν_1 is essentially the observed particle ν_L. Thus the introduction of the Majorana mass term in the Lagrangian leads to a natural explanation for the smallness of neutrino masses: the bigger is the mass of the unseen particle ν_R, the smaller is the mass of ν_L. Currently the only experimental method for determining the quantum nature of the neutrino is the search for neutrinoless double beta decay.

1.3 Double beta decay

Double Beta Decay (DBD) is a second-order weak process in which a nucleus changes its atomic number by two units:

$$(\mathrm{A}, \mathrm{Z}) \rightarrow (\mathrm{A}, \mathrm{Z} \pm 2) \ . \tag{1.12}$$

It occurs for some even-even nuclei for which the single beta decay is energetically forbidden, or suppressed by large change in angular momentum. Double beta decay accompanied by two neutrinos is allowed in the Standard Model (see figure 1.3(a)) and it was detected for the first time in ^{82}Se in 1987 [14]. Now, it has been observed on several other nuclei and the half-lives range from $\sim 10^{18}$ to $\sim 10^{22}$ years.

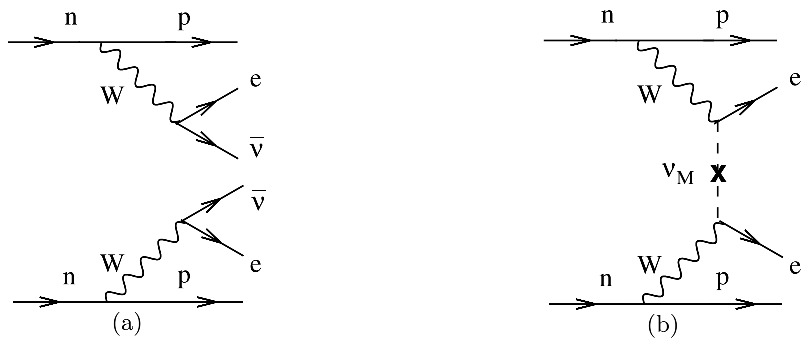

Figure 1.3. Double beta decay diagrams for the DBD mode (left) and the 0νDBD mode (right). The 0νDBD diagram assumes that the process is mediated by the exchange of a Majorana neutrino.

The double beta decay without emission of neutrinos (0νDBD) is instead forbidden in the Standard Model, since it violates the lepton number by two units. Neutrinoless double beta decay can proceed through many different mechanisms: almost any physics that violates the total lepton number can generate it [15]. The simplest way to obtain neutrinoless double beta decay is by the exchange of a massive Majorana neutrino (see figure 1.3(b)). However, no matter which particular mechanism holds, this decay would imply the existence of a Majorana neutrino mass term [16]. This is shown in figure 1.4: the 0νDBD decay can be inverted to produce a $\bar{\nu}_e$ going into a ν_e or, in other words, a Majorana mass term.

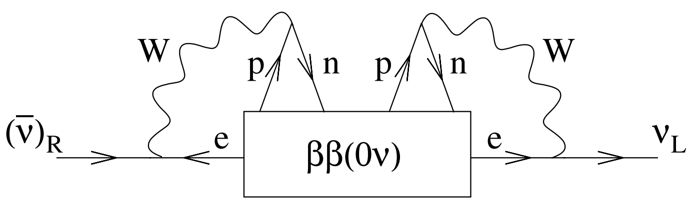

Figure 1.4. Conversion from $\bar{\nu}_e$ to ν_e by a 0νDBD interaction. This diagram proves that the existence of 0νDBD-decay would imply a Majorana mass for neutrino, no matter what is the mechanism that gives rise to the transition.

The rate of this process can be written as [17]

$$\left[T_{1/2}^{0\nu}\right]^{-1} = G_{0\nu} \left|M_{0\nu}\right|^2 \langle m_{\beta\beta} \rangle^2 \tag{1.13}$$

where $G_{0\nu}$ and $M_{0\nu}$ are respectively the phase space factor and the nuclear matrix element (NME) for the 0νDBD transition, and $m_{\beta\beta}$ is the effective Majorana mass:

$$m_{\beta\beta} = \left| \sum_{j=1}^{3} U_{ej}^2 \, m_j \right| = \left| \sum_{j=1}^{3} |U_{ej}|^2 \, e^{i\phi_j} \, m_j \right| . \quad (1.14)$$

In contrast to single beta decay, where m_β was a function of the three $|U_{ei}|^2$, $m_{\beta\beta}$ is a function of the U_{ei}^2 and is therefore sensitive to the two Majorana phases. Since the U_{ei} and the two squared mass differences are known from oscillation experiments, $m_{\beta\beta}$ can be written in terms of only three unknown parameters, the mass of the lightest neutrino and the two Majorana CP phases. The result is shown in figure 1.5, where the allowed values for $m_{\beta\beta}$ are plotted as a function of the lightest neutrino mass.

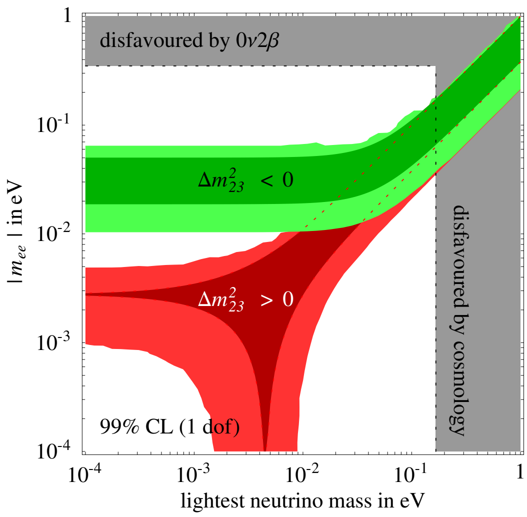

Figure 1.5. Allowed values for the effective Majorana mass as a function of the mass of the lightest neutrino. The green band represents the allowed value in the case of inverted neutrino mass hierarchy, while the red band is for the normal hierarchy case. The region where the green and the red bands overlap is known as “degenerate mass hierarchy”. The darker bands represent the allowed regions that would be obtained if the parameters from oscillation experiments were measured with infinite precision. The gray regions represent the parameter space that is excluded by double current double beta decay experiments and by cosmological observations. Picture taken from [18].

Apart for a controversial claim, later discussed, neutrinoless double beta decay has never been observed. Current experimental limits are reported in table 1.2.

1.3.1 Nuclear matrix elements

Even if the observation of neutrinoless double beta decay of an isotope is enough to make the discovery, the confirmation and the comparison with different isotopes is needed. Different isotopes have different phase space factors and nuclear matrix elements (see equation 1.13), so these quantities must be known to combine and compare the results of different experiments. While the phase space factor can be

Table 1.2. Commonly studied double beta decay isotopes and best lower limits for the 0νDBD half lives. The claim of observation in ^{76}Ge will be discussed later.

Parent Isotope	$T^{0\nu}_{1/2}(y)$	Reference
^{48}Ca	$> 1.4 \times 10^{22}$	[19]
^{76}Ge	$> 1.9 \times 10^{25}$	[20]
^{76}Ge	1.19×10^{25}	[21]
^{82}Se	$> 1 \times 10^{23}$	[22]
^{96}Zr	$> 1.0 \times 10^{21}$	[23]
^{100}Mo	$> 4.6 \times 10^{23}$	[22]
^{116}Cd	$> 1.7 \times 10^{23}$	[24]
^{130}Te	$> 3.0 \times 10^{24}$	[25]
^{136}Xe	$> 1.2 \times 10^{24}$	[26]
^{150}Nd	$> 1.8 \times 10^{22}$	[27]

evaluated exactly, NME represents the biggest source of theoretical uncertainty and cannot be determined experimentally, as it occurs only in the 0νDBD.

Nuclear matrix elements depend on the structure of the parent and daughter nuclei, as well as the intermediate one. Since a many bodies problem must be solved, the calculation cannot be carried out analytically, but requires numerical computations in which several approximations are introduced. There are two basic approaches for the evaluation of nuclear matrix elements, the quasi-particle random phase approximation (QRPA) and the nuclear shell model (NSM). In NSM interactions are described by an effective Hamiltonian which is diagonalized over all configurations of a chosen subset of valence single-particle states. In principle NSM calculations are more reliable, as they require few approximations. However such calculations are computationally intensive, which places a practical limit on the number of single-particle valence states that can be considered. For this reason the QRPA approach is usually preferred. QRPA calculations use a larger valence space with respect to NSM, but the interaction strengths are parameterized, and only a subset of the possible configurations are taken into account. In QRPA particle-particle interactions are fixed by a parameter, g_{pp}, which is derived in various ways by different authors and lead in the past to a significant spread in the results.

Recently, thanks to improvements in the treatment of short-range correlations in the nucleon-nucleon interactions, and to the use of the DBD NME to constraint some parameters in the 0νDBD NME calculations, the spread in the results of different research groups was significantly reduced, and now the NSM and the various QRPA calculations lie within a factor of two to each other. Figure 1.6 shows the nuclear matrix element calculations for various 0νDBD isotopes using the QRPA and the NSM approach.

1.4 Experimental searches for neutrinoless double beta decay

The amount of kinetic energy released in double beta decay, called Q-value, is given by the difference between the mass of the parent nucleus and the mass of the

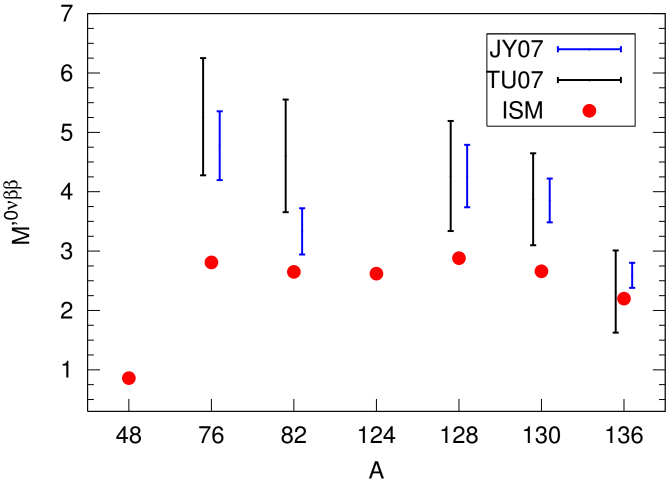

Figure 1.6. Nuclear matrix element calculations for several 0νDBD isotopes using QRPA (black and blue bars) and NSM (red dots). The bars represent the spread introduced in QRPA calculations by the different choices for the coupling constant g_A. Picture taken from [28].

daughter nucleus plus the mass of the two emitted electrons:

$$Q_{\beta\beta} = M_p - (M_d + 2\,m_e)\ . \tag{1.15}$$

In the double beta decay the two neutrinos carry away part of the energy, giving rise to a continuous spectrum of the sum energy of the two electrons. In the neutrinoless decay all the energy goes into the electrons, so that the signature is a monochromatic line in the energy spectrum (see figure 1.7).
The sensitivity of an experiment is defined as the half-life corresponding to the minimum number of signal events observable above background at a given statistical significance. For experiments in which the background counts scales as the total mass of the detector it can be expressed as [17]

$$S^{0\nu}\left(n_\sigma\right) \;=\; \frac{\ln 2}{n_\sigma}\,\epsilon\, N_a\, \frac{\eta}{A}\,\sqrt{\frac{M \cdot t}{b \cdot \Delta E}}\ , \tag{1.16}$$

where n_σ is the statistical significance, ϵ is the detection efficiency, N_a is the Avogadro number, η is the isotopic abundance of the studied nucleus, A is the atomic mass number, M is the total detector mass, t is the live time of the experiment, ΔE is the resolution and b is the background, expressed in counts/(keV $\cdot$ kg $\cdot$ years). To compare the discovery potential of experiments using different isotopes it is convenient to define the nuclear factor of merit F_N:

$$F_N = m_e^2\, G_{0\nu}\, |M_{0\nu}|^2 \tag{1.17}$$

where m_e is the electron mass and F_N has dimension of years^{-1}. Using equation (1.13) and replacing the half-life with the sensitivity, the Majorana mass that an experiment is able to measure can be expressed as:

$$m_{\beta\beta} = \frac{m_e}{\sqrt{S^{0\nu} \cdot F_N}} \tag{1.18}$$

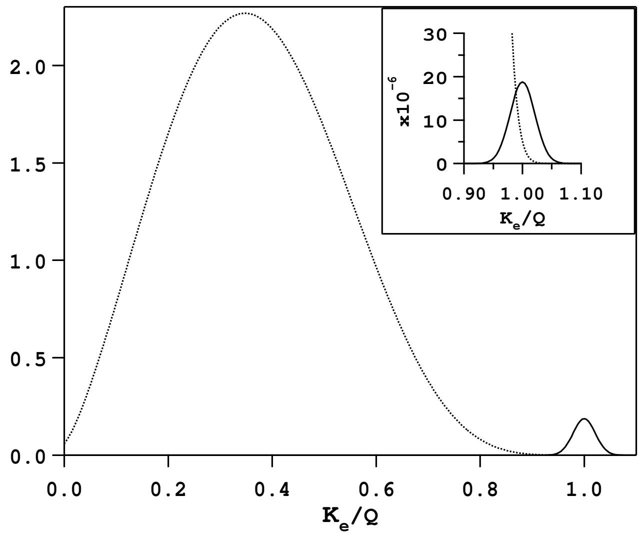

Figure 1.7. Illustration of the spectra of the sum of the electron kinetic energies K_e (Q is the endpoint) for the DBD (dotted curve) and the 0νDBD (solid curve). The spectra are convolved with an energy resolution of 5%. The small insert shows how a poor energy resolution can lead to the confusion of the 0νDBD peak with the tail of the DBD spectrum.

where the sensitivity accounts for the experimental features and the nuclear factor of merit account for the 0νDBD isotope. In table 1.3 the nuclear factor of merit, the Q-value and the natural abundance of the most used 0νDBD candidates is reported.

Table 1.3. Nuclear factor of merit, Q-value and natural abundance (η) for several double beta decay isotopes of experimental interest. The values of F_N are taken from [29].

Parent Isotope	F_N $[y^{-1}]$	$Q_{\beta\beta}$ [keV]	η [%]
^{48}Ca	$0.54 \cdot 10^{-13}$	4271	0.19
^{76}Ge	$0.73 \cdot 10^{-13}$	2039	7.4
^{82}Se	$1.7 \cdot 10^{-13}$	2995	8.7
^{100}Mo	$5.0 \cdot 10^{-13}$	3034	9.6
^{116}Cd	$1.3 \cdot 10^{-13}$	2902	7.5
^{130}Te	$4.2 \cdot 10^{-13}$	2527	34.
^{136}Xe	$0.28 \cdot 10^{-13}$	2479	8.9
^{150}Nd	$57. \cdot 10^{-13}$	3367	5.6

Isotopes with high Q-values are preferred for several reasons. First the background from natural radioactivity decreases with increasing Q. A marking point is represented by the 2615 keV line from ^{208}Tl, the γ-line from natural radioactivity with the highest energy. Isotopes with Q-values above this energy benefit from a much lower background level. Other reasons to prefer big Q-values are represented by the fact that the phase space factor that appears in the formula for the decay rate scales as $G_{0\nu} \sim Q^5$ [15], and that the fraction F of the DBD counts in the region of the 0νDBD peak scales as $F \sim 1/Q^5$ [31].

1.4.1 Past and present experiments

Past and running double beta decay experiments have typical sensitivities that allow to span the effective Majorana mass corresponding to the degenerate neutrino mass hierarchy pattern (see figure 1.5). There are mainly two experimental approaches. In the *source = detector* approach the DBD emitter is part of or constitute the detector. In this way particles are fully absorbed in the detector, allowing high detection efficiency (of order 90%) and high resolution (few keV). Nevertheless there is no sensitivity to the event topology and nature, reducing the background rejection capability. In the *source ≠ detector* approach the DBD emitter is passive and is surrounded by an active detector. Exploiting the typical signature of a two electrons event, the background rejection is very high. On the other hand the resolution is poor (hundreds of keV) as well as the detection efficiency (of order 30%). Examples of the *source = detector* approach are the Heidelberg-Moscow and the CUORICINO experiments. An example of the *source ≠ detector* approach is the NEMO 3 experiment.

The best half life limit on 0νDBD (a complete list is in table 1.2) has been obtained so far in ^{76}Ge by the Heidelberg-Moscow collaboration, using High Purity Germanium semiconductors (HPGe) as detectors. Similar results were also achieved in the IGEX experiment [32]. The big advantage of semiconductor detectors is their excellent energy resolution (about 4 keV at 2 MeV). Even if these devices can only measure the sum energy of the two electrons emitted in the decay, some background reduction can be obtained by exploiting pulse shape analysis. The Heidelberg-Moscow experiment took data in the period 1999-2003 in the Laboratori Nazionali del Gran Sasso (LNGS) using five HPGe detectors. The total detector mass was 11 kg, enriched to about 86% in ^{76}Ge. A background of 0.12 counts/keV/kg/y was obtained around the Q-value of the decay, the best ever so far. With a statistics of 35.5 $\mathrm{kg \cdot y}$ in ^{76}Ge the half life limit obtained by the Heidelberg-Moscow collaboration is $T^{0\nu}_{1/2} > 1.9 \times 10^{25} y$ at 90% C.L. [20]. Using NME calculations from [33] this corresponds to a limit for the effective Majorana mass of $m_{\beta\beta} < 0.35\,\mathrm{eV}$. In 2001 a subgroup of the collaboration found a small peak at the expected position [34, 21] (see figure 1.8) and reported an evidence for neutrinoless double beta decay in ^{76}Ge with an half life in the range $0.7 \div 4.2 \times 10^{25}$y ($3\ \sigma$). Using NME from [33], this result would convert into a value for $m_{\beta\beta}$ in the range $0.2 \div 0.6$ eV. However, the discussion concerning the possible evidence is quite controversial, mainly because the understanding of the background in the region of the peak is not so clear.

Competitive limits on neutrinoless double beta decay come also from the Neutrino Ettore Majorana Observatory (NEMO 3 [35]). Being a tracking experiment, NEMO 3 is not only able to measure the total released energy, but also the energy of the single electrons, their angular distribution and the position where they are produced. NEMO 3 is located in the Frejus Underground Laboratory (France) under a 4800 m w.e. rock shield. The detector has a cylindrical structure composed by 20 identical sectors. In each sector a thin foil 0νDBD source (30-60 g/cm^2) is surrounded by a He-filled tracking detector consisting in drift cells operating in Geiger mode. A magnetic field facilitates identification of the background produced by electron-positron pairs. The tracking chambers are surrounded by plastic scintillators to measure the energy of the two electrons. Thanks to the easy way in which the source foils can

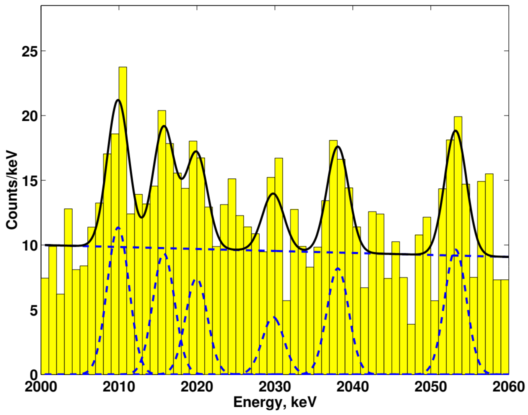

Figure 1.8. Energy spectrum measured by the Heidelberg-Moscow experiment around the Q-value of ^{76}Ge (2039 keV). Picture taken from [21].

be replaced in the detector, NEMO 3 can be used to study any kind of 0νDBD isotope. Its great background rejection capabilities make this detector an ideal tool to study the two neutrino double beta decay mode. At present seven isotopes have been investigated, ^{100}Mo, ^{82}Se, ^{116}Cd, ^{150}Nd, ^{96}Zr, ^{130}Te and ^{48}Ca, but the source mass (about 10 kg) is fairly dominated by ^{100}Mo (about 7 kg) and ^{82}Se (about 1 kg). Figure 1.9 gives an idea of the background rejection capabilities of this experiment. It represent the measured DBD spectra for ^{100}Mo and ^{82}Se. The corresponding values for the 0νDBD half lives are $T^{2\nu}_{1/2} = [7.11 \pm 0.02(stat) \pm 0.54(syst)] \times 10^{18}\,y$ for ^{100}Mo and $[9.6 \pm 0.3(stat) \pm 1.0(syst)] \times 10^{19}\,y$ for ^{82}Se. Limits on the 0νDBD decay channel have also been obtained by NEMO 3: $T^{0\nu}_{1/2} > 4.6 \times 10^{23}\,y$ (^{100}Mo) and $T^{0\nu}_{1/2} > 1.0 \times 10^{23}\,y$ (^{82}Se). The corresponding upper limits for the effective Majorana mass range from 0.7 to 2.8 eV for ^{100}Mo and from 1.7 to 4.9 eV for ^{82}Se (see references in [22] for the NME used to obtain these limits).

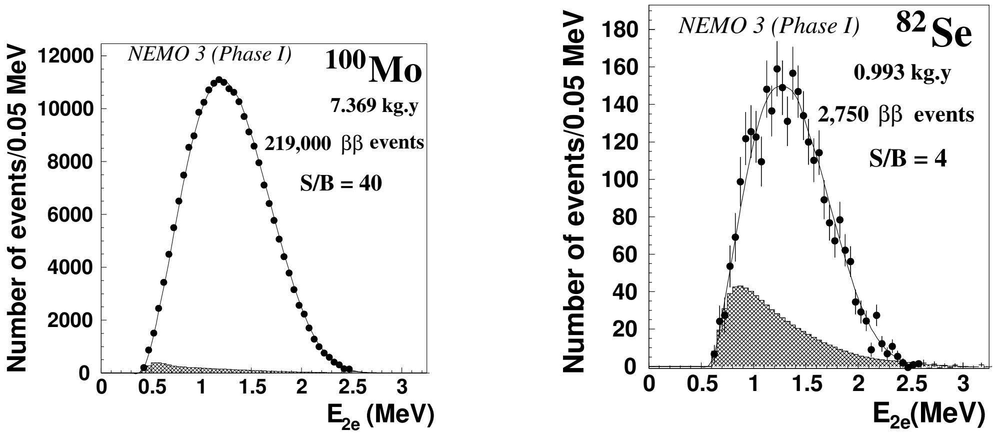

Figure 1.9. Two neutrino double beta decay spectra after background subtraction for ^{100}Mo (left) and ^{82}Se (right) measured by NEMO 3. The black dots represent the data, the solid line is the DBD spectrum expected from simulations and the shaded histogram is the subtracted background. Picture taken from [22].

The CUORICINO experiment [25] will be discussed in the following chapter. It uses TeO_2 bolometers operating at $\sim$ 10 mK to search for neutrinoless double beta decay in ^{130}Te. The detector is located at LNGS, under a 3400 m.w.e. rock shield. With a background level in the region of the 0νDBD peak of 0.2 counts/keV/kg/y, an energy resolution of $\sim$7 keV and a statistics of 11.83 kg $\cdot$ y, CUORICINO obtained a limit on the ^{130}Te 0νDBD half life of $T^{0\nu}_{1/2} > 3.0 \times 10^{24}$ y. Using NME from [36] this translates into a limit on the effective Majorana mass of $m_{\beta\beta} < 0.19 \div 0.68$ eV.

1.4.2 Future experiments

In this section a brief description of the experiments that will start in the next years is presented (see table 1.4). Next generation experiments aim at the investigation of the effective neutrino Majorana mass in the range corresponding to the inverted mass hierarchy region. This corresponds to an increase of about one order of magnitude in the $m_{\beta\beta}$ sensitivity, that in terms of half-life corresponds to an increase of two orders of magnitude. The projected sensitivity will be achieved mainly by an increase of the detector mass and by a reduction of the background.

Table 1.4. Experimental technique, isotope under investigation, source mass, expected half life sensitivity, $m_{\beta\beta}$ sensitivity and current status are reported for the most sensitive next generation 0νDBD experiments. Expected sensitivities are those predicted by the authors (see references in the text).

Experiment	Technique	Isotope	Mass [kg]	$T^{0\nu}_{1/2}$ [y]	$m_{\beta\beta}$ [eV]	Status
Gerda	HPGe	^{76}Ge	40	$2 \cdot 10^{26}$	$0.07 \div 0.3$	in progress
Gerda			1000	$6 \cdot 10^{27}$	$0.01 \div 0.04$	R&D
Majorana	HPGe	^{76}Ge	40	$2 \cdot 10^{26}$	$0.07 \div 0.3$	R&D
Majorana			1000	$6 \cdot 10^{27}$	$0.01 \div 0.04$	R&D
CUORE	bolometers	^{130}Te	200	$2 \cdot 10^{26}$	$0.02 \div 0.09$	in progress
EXO	TPC	^{136}Xe	200	$6 \cdot 10^{25}$	$0.1 \div 0.2$	in progress
EXO			1000	$2 \cdot 10^{27}$	$0.02 \div 0.03$	R&D
Super-NEMO	tracking	^{82}Se	200	$2 \cdot 10^{26}$	$0.05 \div 0.1$	R&D

Gerda [37] (GERmanium Detector Array) is one of the two planned experiments devoted to the study of 0νDBD decay of ^{76}Ge. The detector, which will be operated at LNGS, will be composed by bare HPGe semiconductor detectors immersed in liquid Argon. This cryogenic liquid will serve both as cooling medium for detector operation and as passive and active shield. The liquid Argon cryostat and its content will be protected from environmental radioactivity by a 3 m thick layer of highly purified water. Thanks to these shielding and to pulse shape analysis, the Gerda collaboration plan to reach a background as low as 10^{-4} counts/keV/kg/y in the 0νDBD region. The experiment will be divided in two phases of increasing mass. In the first phase, which will start data taking in 2009, the detectors previously operated by the IGEX and Heidelberg-Moscow experiments will be redeployed. With a total detector mass of $\sim$ 18 kg enriched in ^{76}Ge at 86%, the first phase of Gerda is foreseen to reach a sensitivity of $3 \times 10^{25}\,y$ after one year of data taking, thus being able to confirm or reject the claim of observation in ^{76}Ge. In the second phase, when the total detector mass will be of the order of 40 kg, a sensitivity of $2 \times 10^{26}\,y$ (corresponding to $m_{\beta\beta}$ in the range 0.07$\div$0.3 eV) will be reached in three years of data taking. Depending on the results that will be achieved in the first two phases, a third phase with a mass of the order of one ton could be supported.

MAJORANA [38, 39] will search for neutrinoless double beta decay of ^{76}Ge using semiconductor detectors. The ultimate goal of this experiment is to deploy an array of segmented HPGe detectors enriched at 86% in ^{76}Ge for a total mass of the order of one ton. The detectors will be installed in several separate cryostats that will be hosted in the Deep Underground Science and Engineering Laboratories (DUSEL, 4200 m w.e.) in South Dakota. The MAJORANA collaboration plan to reach a background level smaller than 10^{-3} counts/keV/kg/y in the 0νDBD region. The expected sensitivity after ten years of data taking is $6 \times 10^{27}\,y$ ($m_{\beta\beta} < 0.01 \div 0.04\,$eV). A demonstrator experiment with a total mass of 60 kg will be operated in three cryostats starting from 2010. About 50% of the detectors will be enriched at 86% in ^{76}Ge while the remaining part will have natural abundance and will be used for background studies. Despite its main purpose is the R&D for the ton scale detector, with a sensitivity of $\sim 10^{26}\,y$ the MAJORANA demonstrator will be able in three years to confirm or reject the ^{76}Ge claim of observation.

With the same technique used in CUORICINO, the CUORE experiment [40, 41] will operate an array of 988 TeO_2 bolometers with a total mass of 760 kg (204 kg in ^{130}Te). In the assumption of a background level of 10^{-2} counts/keV/kg/y a sensitivity of $2 \times 10^{26}\,y$ in five years of data taking is expected ($m_{\beta\beta} < 0.02 \div 0.1\,$eV). CUORE is expected to start data taking in 2012.

SuperNEMO [42] is a proposed upgrade of NEMO 3. It is currently in the R&D phase. Main efforts are being spent to achieve a source mass of ∼100 kg of ^{82}Se, but an equivalent mass of other isotopes, such as ^{150}Nd, could be investigated as well. The projected sensitivity for the half life is of $\sim 2 \times 10^{26}\,y$, corresponding to an upper limit on the effective Majorana mass in the range $0.05 \div 0.1\,$eV. Compared to other experiments, SuperNEMO has the unique capability to accommodate several different 0νDBD isotopes in the detector and to change the source foils rather easily. This feature could be of great importance to check for a possible positive signal seen by other experiments.

EXO [43] (Enriched Xenon Observatory) will search for double beta decay in ^{136}Xe using an approach that is rather different from other experiments [44]. The detector will consist of a time projection chamber filled with liquid Xe enriched at 80% in ^{136}Xe, able to detect both ionization and scintillation light produced by the two electrons emitted in double beta decay. In addition to energy measurement and position reconstruction the EXO collaboration plan to identify the daughter ion produced in the decay (^{136}Ba^{++}), which would reduce the background to a negligible level. Once a 0νDBD candidate event is identified, the ion is extracted from the detector and is put into a trap where it is identified by laser spectroscopy. In the first phase of the experiment a 200 kg detector prototype will be operated without ion tagging (EXO-200). The expected sensitivity in this phase will be of $\sim 6 \times 10^{25}\,y$ ($m_{\beta\beta} < 0.1 \div 0.2\,$eV). With a total mass of 1 ton, the final EXO detector will reach a sensitivity of $2 \times 10^{27}\,y$ ($m_{\beta\beta} < 0.02 \div 0.03\,$eV).

Chapter 2

TeO_2 bolometric detectors for 0νDBD search

The use of bolometric detectors for the search of neutrinoless double beta decay was proposed by Fiorini in 1984 [45]. The successful operation of a 340 g Tellurium dioxide crystal was followed by the construction of a detector array composed by 20 crystals, for a total mass of 6.8 kg of TeO_2 [46]. A further mass increase was obtained with the recently completed CUORICINO experiment [25]. Operated in the Laboratori Nazionali del Gran Sasso in the years 2003-2008, CUORICINO was composed by a tower of 62 TeO_2 bolometers, with a total mass of $\sim$ 41 kg. At present the CUORICINO result represents one of the most competitive limits, comparable with the ones obtained with Germanium detectors. The excellent performance obtained with CUORICINO demonstrates the feasibility of a ton scale bolometric experiment, CUORE [40, 41], aiming at the investigation of the effective neutrino mass in the inverted hierarchy range.
In this chapter the TeO_2 bolometric detectors will be presented.

2.1 Bolometric detectors

Bolometers are calorimeters working at low temperatures in which the energy of particle interactions is converted into phonons and measured via temperature variation. Conventional techniques for energy deposition measurements are based on the detection of the energy released in the form of ionization and excitation of the atoms in the detector. Unfortunately, the amount of energy lost in channels different from the detected ones is quite large. Most of the energy is converted in phonon excitations inside the detector and is not measured. Thermal detectors on the other hand measure the portion of the deposited energy converted into phonons and guarantee a better intrinsic energy resolution. Nevertheless they are slow detectors so that they are suitable only for experiments working at low rates. Bolometers consist of two main components: an energy absorber, where particles deposit their energy and a sensor, which converts the excitations produced by the particle into a signal (see figure 2.1).

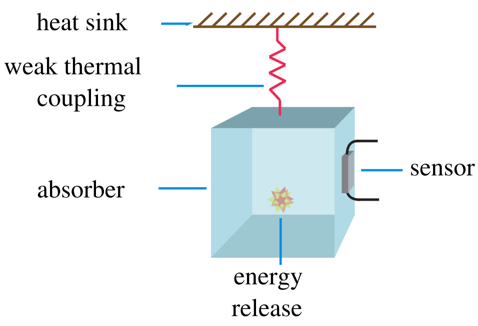

Figure 2.1. Schematic representation of a bolometric detector: an absorber is connected to a heat sink through a weak thermal coupling and a sensor for signal readout is attached to the absorber.

2.1.1 The energy absorber

The absorber can be roughly sketched as a capacitance C connected to an heat bath through a conductance K. Therefore the temperature variation induced by a deposit of energy E, assuming that C does not depend on temperature, is:

$$\Delta T = \frac{E}{C} \ . \tag{2.1}$$

The absorbed heat then flows trough the conductance until an equilibrium condition with the heat sink is reached:

$$\Delta T(t) = \frac{E}{C} \exp\left(-\frac{t}{\tau}\right) \tag{2.2}$$

where $\tau = C/K$ is the time constant of the bolometer. With these simple considerations, it is clear that to obtain big and fast signals the capacitance of the absorber must be small. This requirement can be fulfilled only operating at cryogenic temperatures, between 10 and 100 mK.
The specific heat of a material at low temperatures is the sum of the lattice and the electron specific heats:

$$c(T) = c_l(T) + c_e(T) \tag{2.3}$$

The lattice specific heat is described by the Debye law:

$$c_l(T) = \frac{12}{5}\pi^4 N_a k_B \left(\frac{T}{\Theta_D}\right) \quad T < \Theta_D \tag{2.4}$$

where N_a, k_B and Θ_D are the Avogadro number, the Boltzmann constant and the Debye temperature respectively. In metals the specific heat of the electrons is:

$$c_e(T) = \frac{ZR}{\Theta_D}\pi^2 \frac{T}{\Theta_F} \tag{2.5}$$

where Z, R and Θ_F are the number of conduction electrons, the gas constant and the Fermi temperature respectively. Given the different temperature dependence of c_l and c_e, the electron specific heat dominates at low temperatures. Dielectric and diamagnetic materials, lacking in electron contribution, have then low capacitance and are preferred.

Particles can interact with the absorber by scattering on nuclei or on electrons, in both cases the energy is finally converted into phonons. When particles interact with

nuclei the released energy produces vibrational excitations but could also produce structural damages of the lattice, where the energy can be stored. If this energy is not converted into phonons, the statistical fluctuation of the number of produced defects can worsen the energy resolution. The fraction of lost energy depends on the incident particle: for electrons and photons it is negligible, whereas for particles having some MeV of energy it can cause a FWHM resolution of hundreds of eV.
When instead the particle interacts with the electrons of the crystal, it is slowed down in few μm (heavy particles) or mm (electrons) from its interaction point and normally stops in the crystal. Along its track it produces many electron-hole pairs having at the beginning very high spatial density and energy. These charge carriers interact with each other and spread very quickly inside the crystal. As a quasi-equilibrium situation is reached, they undergo their final degradation via direct interaction with the lattice site: these interactions produce phonons. During this step undesirable processes can take place, indeed a fraction of the pair energy can leave the crystal or can be stored in stable or metastable states instead of going into the crystal lattice.

In a very simplified model in which all the thermal phonons are detected, a rough estimate of the energy resolution can be derived. The thermodynamic equilibrium between the absorber and the heat sink is hold by a continuum exchange of phonons trough the conductance K. The fluctuation of the number of phonons in the absorber produces a temperature variation that in turns affects the energy resolution. The energy E in the absorber is:

$$E = C(T) \cdot T \tag{2.6}$$

or in terms of the energy of each phonon $\epsilon = k_B T$:

$$E = N \cdot \epsilon \; . \tag{2.7}$$

Assuming that the number of phonons obeys the Poisson statistics, the energy fluctuation is:

$$\Delta E = \Delta N \cdot \epsilon = \sqrt{k_B C(T) T^2} \; . \tag{2.8}$$

It should be stressed that, at least for CUORE bolometers, the thermodynamic fluctuations give a negligible contribution to the energy resolution. From the above expression, using typical values of CUORE bolometers ($C = 10^{-9}$ J/K, $T = 10$ mK), a resolution of ~ 10 eV is predicted, that is well below the measured resolution (few keV). The thermodynamic limit can be obtained only when the statistical fluctuations of the physical processes coming before the thermalization are negligible, when the temperature of the heat sink is constant enough, and when the noise of the detector is minimized (see section 2.6).

2.1.2 The choice of TeO_2

CUORE uses TeO_2 crystals as absorbers. The use of TeO_2 is motivated by various reasons, some of them related to the 0νDBD candidate isotope (^{130}Te) and others related to the cryogenic properties of the material. Double beta decay of ^{130}Te occurs through the transition:

$$^{130}\mathrm{Te} \rightarrow ^{130}\mathrm{Xe} + 2\mathrm{e}^- + (2\,\bar{\nu}) \, . \tag{2.9}$$

The most striking feature of ^{130}Te compared to other 0νDBD isotopes is the high natural abundance (see table 1.3). Compared to other materials that usually need to be enriched, the abundance of ^{130}Te allows to build an experiment with natural Tellurium. This is an advantage both in terms of costs and material cleanliness, as enrichment procedures often introduce radioactive contaminations. The transition energy of ^{130}Te ($Q_{\beta\beta} = 2527.0 \pm 0.3\,\mathrm{keV}$ [30]) is not very high. It has been shown in section 1.4 that experiments using isotopes with Q-values above 2615 keV are affected by a much lower radioactivity background. However, this transition energy happens to be situated between the peak and the Compton edge of the 2615 keV line of ^{208}Tl which leaves a clean window to look for the signal.

The possibility to use pure tellurium crystals as absorbers was taken into account but it was ruled out mainly because of the poor mechanical properties at low temperatures. Stresses caused by the thermal contractions revealed to produce excessive damages on pure Te crystals. TeO_2 has instead a good mechanical behavior, and has an higher Debye temperature, implying lower specific heat and thus a higher sensitivity to thermal pulses.

2.1.3 The sensor

The phonon sensor is usually a thermistor, a resistive device that converts temperature variations into resistance variations. There are basically two types of thermistors, Transition Edge Thermistors (TES) and Semiconductor Thermistors (ST). TES are superconducting films kept at the critical temperature, they have a rather fast response ($\sim \mu$s) but can only work in a narrow range of temperatures. On the other hand ST have a slower response ($\sim$ ms) but can be used in a wider range of temperatures. A parameter characterizing the sensor is the logarithmic sensitivity η:

$$\eta = \left| \frac{d \log R(T)}{dT} \right|. \tag{2.10}$$

The above expression implies that (apart signs):

$$\frac{dR}{R} = \eta \frac{dT}{T} \tag{2.11}$$

where it is evident that the larger is η the higher is the response of the device. Typical values of η are 10 for ST and 100 for TES. Despite the lower sensitivity, ST have been preferred for CUORE bolometers because of their wider range of operating temperature. In the following, the operating principles of semiconductor thermistor will be presented.

Semiconductors are covalent solids that behaves as insulators because the valence band is full and the conduction band is empty, nevertheless the energy gap between valence and conduction band is less than 2 eV. The conduction can then happen only with an activation energy greater than the energy gap. Since at room temperature $kT \simeq 0.025\,\mathrm{eV}$, the conduction can only happen at higher temperatures. If instead the semiconductor lattice has impurities (extrinsic or doped semiconductors), then new energy levels are introduced slightly above the valence band or below the conduction band, depending on the type of atoms inserted. With this technique the conduction can also happen at lower temperatures. The dopant concentration determines the

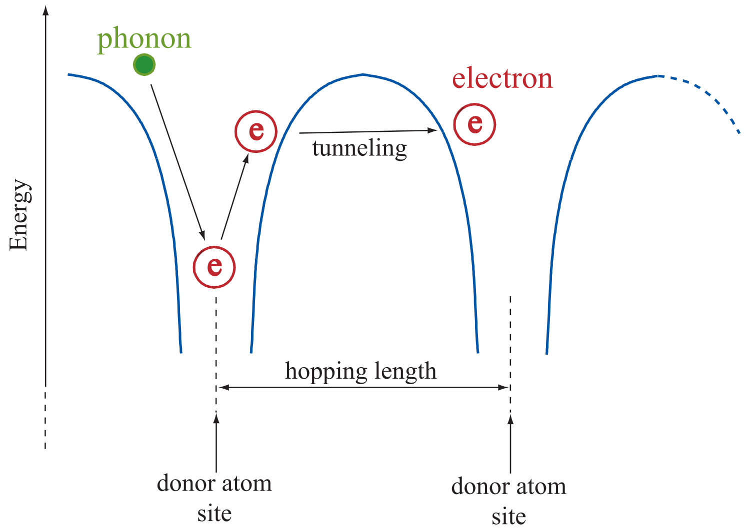

Figure 2.2. Schematic representation of the hopping conduction mechanism

behavior of the solid and there is a critical concentration that characterizes the transition from metal to insulator. The region near this concentration is named metal-insulator transition region (MIT) [47], where the material resistivity exhibits a dependence on the temperature.

At temperatures lower than 10 K the conduction is dominated by the migration of the charge carries between impurity sites. In this situation electrons are not localized and the conduction happens when an electron jumps from a donor site to another, without using the conduction band (*hopping mechanism*). This migration is due to the tunnelling through the potential barrier separating the two dopant sites and it is activated by phonons (see figure 2.2). At even lower temperature, the energy of the phonons that are responsible for the conduction mechanism is low, and charge carriers migrate also to far impurity sites with free energy levels that are close to the Fermi energy. In this conduction regime, called Variable Range Hopping [48] (VRH), the concentration of minority charge carriers determines the density of states close to the Fermi level. The MIT is set not only varying the concentration of dopant but also varying the ratio of acceptor and donor concentrations.

In the VRH conduction regime the resistivity dependence on temperature is described by the law:

$$\rho(T) = \rho_0 \exp\left(\frac{T_0}{T}\right)^\gamma \tag{2.12}$$

where ρ_0, T_0 depend on the doping concentration and $\gamma = 1/2$. The expression of the logarithmic sensitivity can be easily derived from the above equation using (2.10):

$$\eta = \gamma \left(\frac{T_0}{T}\right)^\gamma . \tag{2.13}$$

2.1.4 NTD-Ge thermistors

The thermal sensor used in CUORICINO and CUORE bolometers is a Neutron Transmutation Doped (NTD) germanium thermistor operating in the VRH regime [49].

Melt-doped Ge crystals cannot achieve the necessary uniformity due to the effect of dopant segregation. The only technique available for producing uniform doping is NTD: Ge wafers are bombarded with thermal neutron beams that, inducing nuclear reactions, create donor (As and Se) and acceptor (Ga) impurities. The natural abundances of Germanium are such that this doping technique allows to obtain the right dopant concentration, which determines the sensor performances. Wafers are then cut into pieces, each of them is a thermistor and its resistance can be expressed as:

$$R = R_0 \exp \left(\frac{T_0}{T} \right)^{\gamma} \tag{2.14}$$

where R_0 depends on the geometry and is roughly $R_0 = \rho_0\, l/S$, being l and S the length and the section of the piece respectively. The parameters R_0, T_0 and γ are determined experimentally. The measurement is made coupling the sensor to a low temperature heat sink using an high conductivity epoxy, so that the electrothermal feedback is negligible (see next section). The heat sink temperature is then varied (15-50 mK) while a steady current flows through the thermistor. Using a calibrated thermometer the parameters can be extracted from a fit to the $R(T)$ characteristic. Typical parmeters of CUORE NTD's are:

$$R_0 = 1.15\ \Omega\,, \qquad T_0 = 3.35\,\mathrm{K} \qquad \text{and} \qquad \gamma = 1/2 \tag{2.15}$$

Using these values we can calculate the static resistance (R_S) at the working temperature $T_S = 10\,\mathrm{mK}$ to be approximately $100\,\mathrm{M}\,\Omega$.

2.2 Bolometer operation

To measure the resistance variation the thermistor is biased with the circuit shown in figure 2.3(a). A bias voltage V_B is produced by a voltage generator closed on a load resistor that is put in series with the thermistor. The load resistance R_L is chosen much higher than the thermistor resistance R_{bol} so that the current in the circuit I is constant and the voltage across the thermistor V_{bol} is proportional to R_{bol}:

$$V_{bol}(T) = I \cdot R_{bol}(T)\ . \tag{2.16}$$

This current produces a power dissipation $P = VI$ that in turns heat the thermistor decreasing its resistance, this phenomenon is known as "electrothermal feedback". In static conditions the thermistor temperature T_S is

$$T_S = T_{hs} + \frac{P}{K} \tag{2.17}$$

where T_{hs} is the temperature of the heat sink and K is the conductance to it. The $R - P$ dependence is depicted in figure 2.3(b). The electrothermal feedback makes the $I - V$ relation deviate from linearity and leads to a non-ohmic behavior (see figure 2.4(a)). Increasing the bias current the slope of the curve increases until it crosses the so called inversion point (IP) and then decreases. In static conditions the thermistor electric and thermal parameters are described by a point on the load curve.

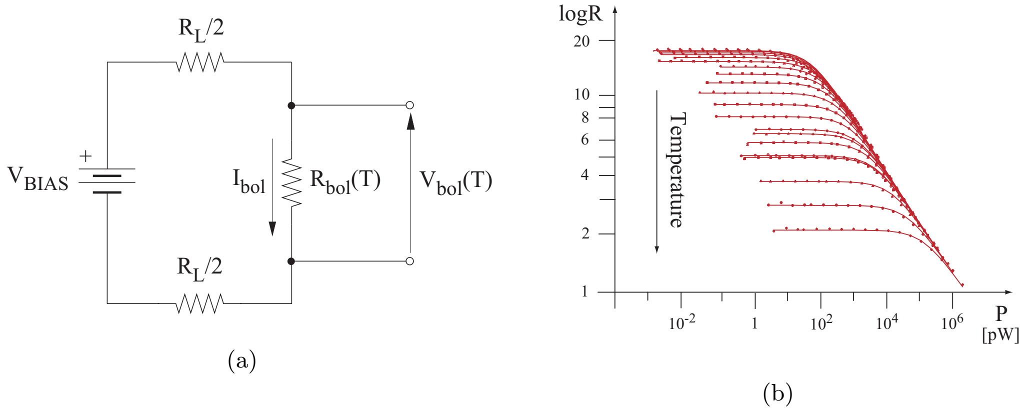

Figure 2.3. The left picture shows the electric scheme of the bias circuit used for thermistor readout. The right picture shows the dependence of the resistance on the power dissipation for various values of the base temperature. Curves with lower resistance at P=0 correspond to higher base temperatures.

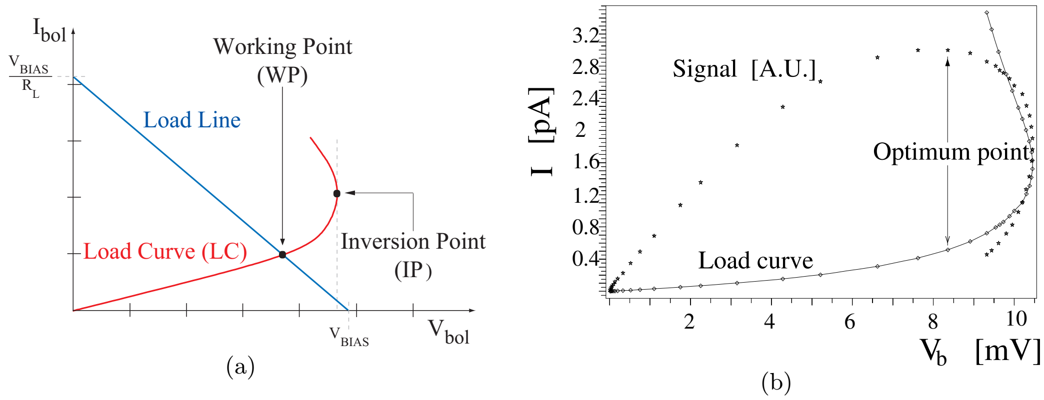

Figure 2.4. Load curve of a semiconductor thermistor. On the left picture the working point is determined by intersection of the sensor characteristic curve with the bias circuit load line. On the right the load curve is shown together with the corresponding signal amplitude.

When particles release an amount of energy E in the absorber the voltage across the thermistor varies leading to a signal. A rough estimate of the voltage increase is:

$$\Delta V = \eta V \frac{\Delta T}{T_S} = \eta \sqrt{P \cdot R_S}\, \frac{E}{C\, T_S} \tag{2.18}$$

where R_S is the static resistance and we used $R_L \gg R_S$. This expression vanishes both for $P \to 0$ and $P \to \infty$ because the resistance vanishes at high temperatures, then a maximum signal amplitude must exists somewhere. If all the detector parameters were known, the optimal working point could be determined analytically. Nevertheless, it happens often that not all of them are known with accuracy and the working point has to be determined experimentally. The procedure consist in scanning the amplitude of a pulse of fixed energy varying the bias current, and selecting the point where the signal is maximum (see figure 2.4(b)) .

2.3 Arrays of TeO_2 bolometers

The single module is the elementary unit of arrays of TeO_2 detectors. Its component are: the absorber crystal of TeO_2 the NTD thermistor, the heater, the PTFE supports and the copper structure. The NTD-Ge thermistors are glued onto the TeO_2 crystals by nine spots of Araldit Rapid epoxy (diameter 0.5 mm, height 50 μm). The crystal is held by PTFE supports that are connected to a copper frame. The copper frame is connected to the mixing chamber of a dilution refrigerator that provides the base low temperature ($\sim$ 10 mK) to operate the bolometers. Heaters [50] are heavily doped silicon chips with a resistance between 50 and 100 kΩ. They are used as Joule heaters to inject a controllable energy in the crystal to emulate the effect produced by real particles for calibration purposes (see section 4.1). The single modules are usually packed into floors that in turn are piled up to form a tower. As an example, the CUORICINO tower is represented in figure 2.5(a).

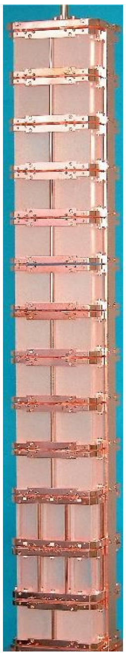

(a)

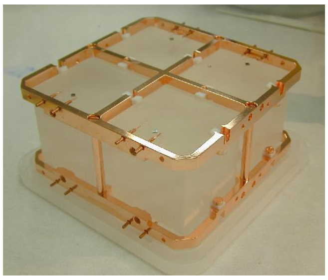

(b)

(c)

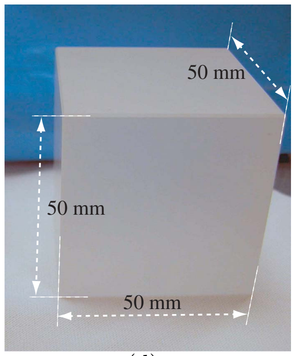

(d)

Figure 2.5. On the left the entire CUORICINO tower is shown. The top right picture shows one of the eleven floors composed by four crystals, while the bottom left picture shows one of the two nine crystals floors. The picture over the caption shows a $5 \times 5 \times 5\,\mathrm{cm}^3$ TeO_2 crystal.

2.4 Cryogenic setups

To reach the temperature of 10 mK the TeO_2 bolometric experiments need a cryogenic setup. Two cryogenic setups were installed in the ’80 at Laboratori Nazionali del Gran Sasso (LNGS) in Italy. The first one, hosted in the A hall of the laboratory, was used for CUORICINO and is now used for R&D activities. The second one, hosted in the C hall, has been always dedicated to R&D activities for CUORE. Both of them are dilution refrigerators housed inside Faraday cages to suppress electromagnetic interferences. The experimental volume in the hall A cryostat is about 16 liters while in the hall C one is less then a third. The dilution refrigerators are equipped with heavy shields against environmental radioactivity. In particular, the hall A one is shielded with two layers of lead of 10 cm minimum thickness each. The outer layer is made of commercial low radioactivity lead, while the internal one is made with special lead with a ^{210}Pb contamination of 16 Bq/kg (see figure 2.6). The external lead shields are surrounded by an air-tight box flushed with fresh

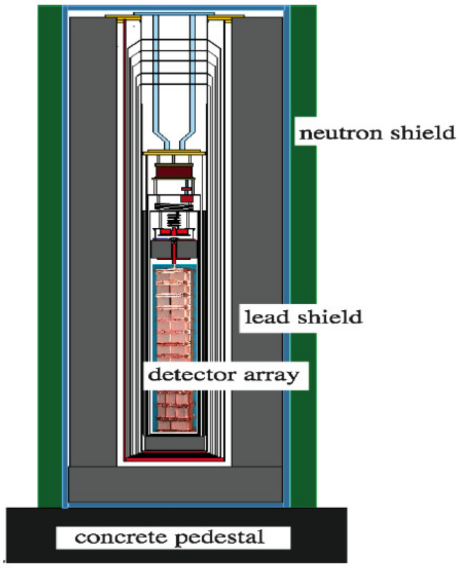

Figure 2.6. Sketch of the CUORICINO apparatus showing the tower hanging from the mixing chamber of the dilution refrigerator and the detector shields.

nitrogen from a dedicated evaporator to avoid radon contamination of the gas close to the cryostat. In order to shield the detectors against the unavoidable radioactive contamination from some fundamental components of the dilution refrigerator, thick layers of Roman lead are placed inside the cryostat just around the detectors. A borated polyethylene neutron shield (10 cm) was added in 2001 to the hall A cryostat.

2.5 Signal readout

The electrical connection of the bolometric signal from 10 mK to room temperature is divided in two parts. After coming out from the single module, the signal runs along the tower over a twisted pair of wires, until it reaches the mixing chamber. From this point on, the signal is delivered over a pair of twisted coaxial cables: passing through several thermalization stages these wires reach the exterior of the cryostat. These wires are made of constantan, an electric conductor that has the rare property of not conducting heat. The cryostat is finally plugged to the front-end electronic boards through a set of Fisher connectors. The analog part of the readout system performs mainly three operations: thermistor biasing, signal amplification and signal filtering. The front-end boards contain the biasing circuit and the amplification stages, and their parameters are remotely programmable [51].
As stated in section 2.2 the load resistors must be large compared to the sensor resistance; since the typical thermistor resistance R_S is of order 100 M Ω at 10 mK, their value is 27 G Ω each. The bias voltage V_B can be set in the range $0 \div 10$ V and

for a typical bias $V_B = 5\,\mathrm{V}$ the output voltage of the thermistor when no energy is released in the crystal is:

$$V_{R_S} = V_B \frac{R_S}{R_S + R_L} \simeq 10\,\mathrm{mV}. \tag{2.19}$$

where R_L represent the series of the two load resistors. The signal observed when particles impinge on the detector leads to a voltage variation of about 200 μV/MeV that in turn is amplified. The gain (G) of the amplifier is then adjusted to fit the energy region of interest into the ADC range with G ranging between 450 and 10000 V/V. The drift current of the amplifier generates an offset voltage that summed to $V_{R_S} \cdot G$ can shift the signal out of the ADC range. To correct for this effect an additional offset is added to the output signal.

After the amplification and the offset correction the signal goes through an anti-aliasing 6-pole Bessel Filter with an attenuation of 120 dB/decade and a programmable cutoff ranging between 8 and 20 Hz. Finally the signal is acquired by an ADC (range $[-10.5, 10.5]$ V, 18 bits) with a typical sampling period of 8 ms (125 Hz). Given the low event rate, it was possible to implement a software trigger. When a trigger is found the signal is recorded in a window of ~ 3 seconds. In order to have an estimate of the bolometer temperature at the time of the pulse (see section 4.1), about one second of baseline before the trigger is recorded, leading the total window length to ~ 4 seconds. Selected events are then written to disk for offline processing. A typical event generated by a 2615 keV γ particle is shown in figure 2.7.

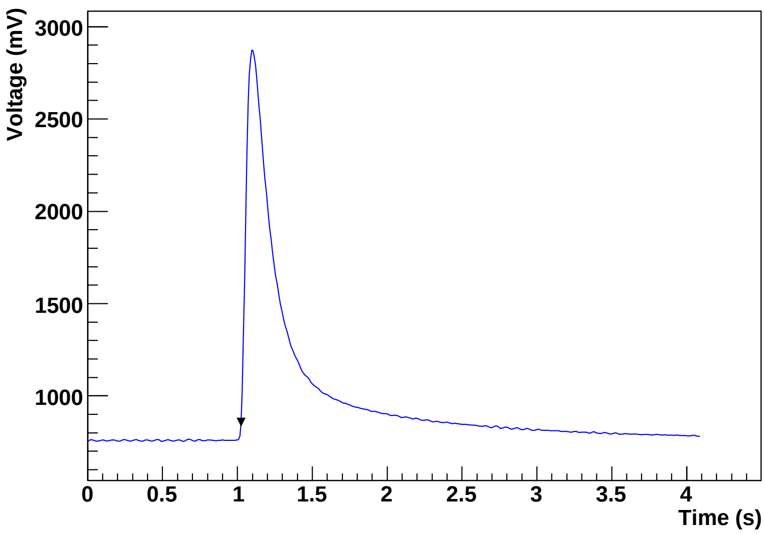

Figure 2.7. Acquired signal generated by a 2615 keV γ particle.

2.5.1 Measurement of the static resistance

The thermistor static resistance (R_S) is measured right after the detector cooling to estimate the working temperature of each detector. This parameter is also one of the ingredients of the model developed in the next chapters. In this section we describe the procedure to measure the value of R_S that is extracted from equation (2.19) by measuring V_{R_S}.

The voltage measured at the end of the readout chain is not only the amplified thermistor voltage but contains also an unknown offset V_h generated by the amplifier itself and by the front-end board:

$$V = V_{R_S} G + V_h \,. \tag{2.20}$$

To cancel this contribution the thermistor is biased with an opposite voltage $-V_B$ so that V_{R_S} changes sign while V_h does not:

$$V^+ \quad = V_B \tfrac{R_S}{R_S+R_L} G + V_h = V_{R_S} G + V_h \tag{2.21}$$

$$V^- \quad = -V_B \tfrac{R_S}{R_S+R_L} G + V_h = -V_{R_S} G + V_h \,. \tag{2.22}$$

It is important to notice that the gain used during normal acquisition runs is almost always too high to contain both these voltages into the ADC range. The gain is therefore lowered to a smaller value G_S (where the S subscript is related to the R_S measurement). The voltage across the thermistor is then evaluated as:

$$V_{R_S} = \frac{V^+ - V^-}{2G_S} \tag{2.23}$$

and the corresponding resistance is:

$$R_S = \frac{R_L}{V_B / V_{R_S} - 1} \,. \tag{2.24}$$

2.6 Detector noise

The thermodynamic fluctuations of the crystal described in section 2.1.1 represent the ultimate noise source because in practical applications they give a negligible contribution compared to the noise coming from the electronics and the cryogenic apparatus. In this section the principal noise sources will be presented. Every resistance R working at temperature T generates a white noise due to the fluctuations of the charge carriers. For load resistors the spectral density can be expressed as:

$$\Delta V_L^2 = 4kT_{R_L} R_L \tag{2.25}$$

that on the output voltage of the bolometer becomes:

$$\Delta V_b^2 = \frac{\Delta V_L^2}{(R_L{}^2)} \left(\frac{R_S R_L}{R_S + R_L} \right)^2 \simeq 4kT \frac{R_S^2}{R_L} \,. \tag{2.26}$$

Using the detector typical parameters the above equation translates into a noise of order 300 eV rms. The preamplifier noise is of three types: *series*, generated by the JFET resistances, having a value around 10 eV rms, *series 1/f* that amounts to 15 eV rms and *parallel shot*, that at room temperature amounts to 130 eV rms. To reduce this noise, load resistors and preamplifiers of some channels were housed in the cryostat at $\sim 110\,\mathrm{K}$. This cold electronics setup however did not improve the resolution of the detector.

The dominant noise contribution comes from the vibrations of the cryogenic apparatus. These vibrations are transmitted to crystals and wires producing two different types of noise. The crystal vibrations generates an energy dissipation that in turn changes the temperature. These temperature instabilities have a frequency spectrum similar to the signal one, and then they are the most dangerous source of noise. The wires vibrations change the wire-wire capacitance and the wire-ground capacitance, generating the so called *microphonic* noise.
Quantifying the amount of vibrational noise is difficult, and it strictly depends on the cryogenic setup and on the detector assembly. These vibrations are anyway reduced hanging the detector to the cryostat by means of a spring, and mechanically decoupling the cryostat from the outer environment.

2.7 CUORICINO and CUORE

The CUORICINO detector was a tower like structure. It was composed by eleven floors of four modules each ($5 \times 5 \times 5\,\mathrm{cm}^3$ crystals) and two additional floors of nine modules each ($3 \times 3 \times 6\,\mathrm{cm}^3$ crystals). The small crystals came from the previous MiDBD experiment while the big crystals were made explicitly for CUORICINO. Two of these smaller crystals were enriched in ^{130}Te and two were enriched in ^{128}Te. These crystals were designed to measure the DBD spectrum of ^{130}Te by subtracting the background seen in the crystals enriched in ^{128}Te. The result of this analysis was a measurement of the DBD half-life of $6.1 \cdot 10^{20}$ years [52].
The collected statistics was about $18\,\mathrm{kg \cdot y}$ of ^{130}Te in five years of data taking. Part of this data ($11.83\,\mathrm{kg \cdot y}$) have been analyzed assuming a Q-value of $2530\,\mathrm{keV}$. The background rates in the 0νDBD region were 0.18 ± 0.01 counts/keV/kg/y for the $5 \times 5 \times 5$ crystals, and 0.20 ± 0.04 counts/keV/kg/y for the small crystals. The energy resolution was evaluated to be $7\,\mathrm{keV}$ and $12\,\mathrm{keV}$ FWHM for the big and the small crystals respectively. The single-hit spectrum is shown in figure 2.8. The experiment was able to set a lower limit of $3.0 \cdot 10^{24}\,\mathrm{y}$ for the 0νDBD half life of ^{130}Te corresponding to $m_{\beta\beta} < 0.19 \div 0.68\,\mathrm{eV}$, depending on the nuclear matrix element evaluation [36, 53, 54, 28].

The CUORE detector will be made of 19 towers of 13 floors each, with four $5 \times 5 \times 5\,\mathrm{cm}^3$ crystals per floor (see figure 2.9). The goal of this experiment is to achieve sensitivity to the inverted neutrino mass hierarchy. By increasing the mass by a factor twenty, and reducing the background by a similar factor, the CUORE collaboration will improve the sensitivity to the ^{130}Te by a factor twenty. The detector will be hosted in the A Hall of LNGS, the same experimental hall of CUORICINO, the construction is scheduled for completion in 2012.

Now that the mass of the detector is fixed, the collaboration is mainly working on improving the resolution and the background of the detector. The target resolution is $5\,\mathrm{keV}$ FWHM and will be realized reducing the detector noise. Given that the main noise contribution is generated by crystal vibrations, the new detector structure, known as “Gorla” configuration by the name of the proponent, includes a new design of the Teflon supports. These supports, thanks also to the tighter crystal size tolerances, clench the crystal reducing vibrations. The background coming from the cryostat and from the outside will be reduced including a thicker lead shield inside the cryostat. The background generated by radioactive contaminations of the

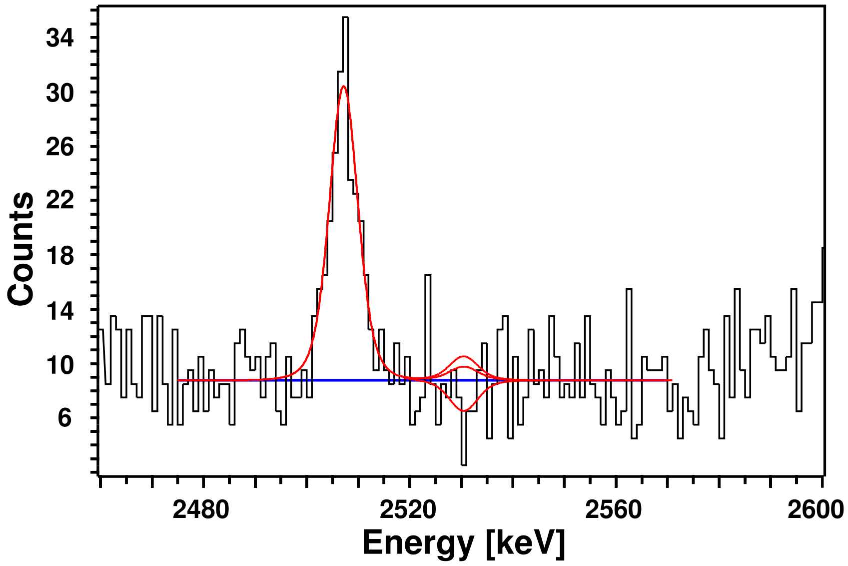

Figure 2.8. Single hit background spectrum of CUORICINO. The peak at 2505 keV is produced by the two gamma's emitted in the beta decay of ^{60}Co. It is about 7 σ away from the position where the 0νDBD peak is expected. The red lines represent the best fit to the number of 0νDBD events, 68 % and 90 % C.L. bounds.

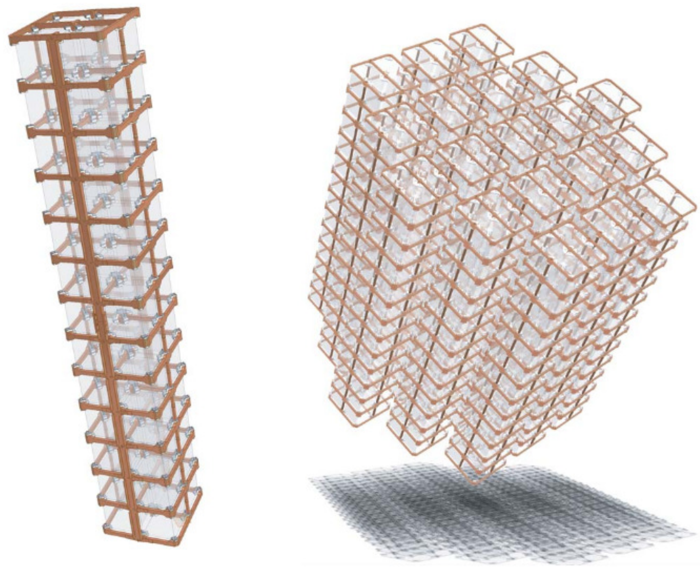

Figure 2.9. The CUORE detector array is roughly 19 times CUORICINO.

copper structure is currently under study, and different cleaning techniques of the copper are being tested (see section 5.1). In the hoped case, CUORE will have a background of 0.01 counts/keV/kg/y, corresponding to a half-life sensitivity of about $2.1 \cdot 10^{26}$ y in five years (see figure 2.10).

The main technical efforts concern the construction of the cryostat and the calibration system. The detector will be cooled by a ^{3}He/^{4}He dilution refrigerator that is being especially designed for CUORE by Leiden Cryogenics and is sketched

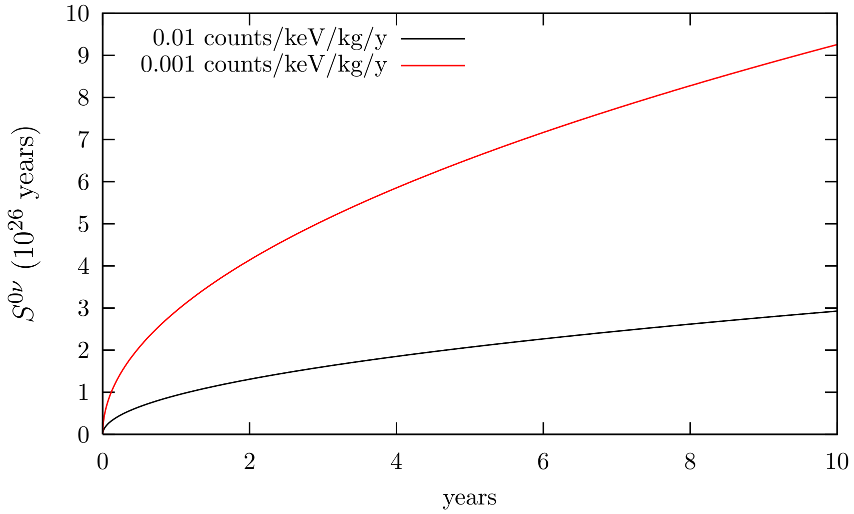

Figure 2.10. CUORE sensitivity to the 0νDBD half-life of ^{130}Te in two background scenarios, 0.01 counts/keV/kg/y and 0.001 counts/keV/kg/y.

in figure 2.11.
CUORICINO was calibrated facing Thorium sources to the detector from the outside of the cryostat (see section 4.4.1). The greater amount of TeO_2 in CUORE makes this technique not usable. If the detector were exposed to an external source, the innermost bolometers would experience a much lower rate of calibration events than the outermost. Sources of different intensity could be used to calibrate at different times inner and outer bolometers. Given that this procedure should last at least a week, and given that the calibration is repeated every month, the live time of the experiment could be significantly reduced. An alternative option consists in inserting the sources between the towers, in the 10 mK environment. The system to lower and raise the sources is currently being developed, taking into account the radioactivity constraints and the time needed to thermalize the sources from 300 K to 10 mK, that even in this case could not be negligible.

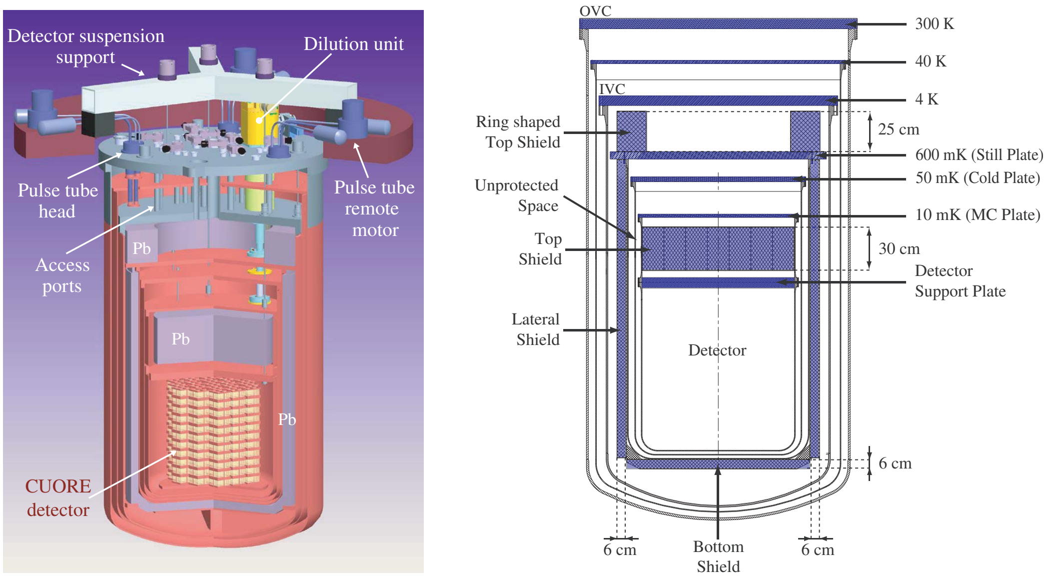

Figure 2.11. CUORE cryostat and internal shields.

Chapter 3

Model of the response function of CUORE bolometers

CUORE bolometers are used to detect particle energies from few keV up to several MeV measuring the temperature change due to the energy released. The response function of these detectors is not uniform in the energy range of interest: the rise and decay time of the signal change with energy as well as the pulse amplitude relationship with energy is complicated. Moreover the response function changes when the detector base temperature changes. A faithful modeling of these detectors is needed to improve the data-analysis and to build simulations of their signal.

The thermal process in bolometers involves many elements like the capacitance of the crystal, the conductance of the glue that attaches the thermistor to the crystal, the heat capacity of the crystal supports and their conductance to the main bath, the heat capacity of the thermistor and the conductance of its wires to the main bath (see figure 3.1). All these elements have a strong dependence on the working temperature and may vary among different bolometers.

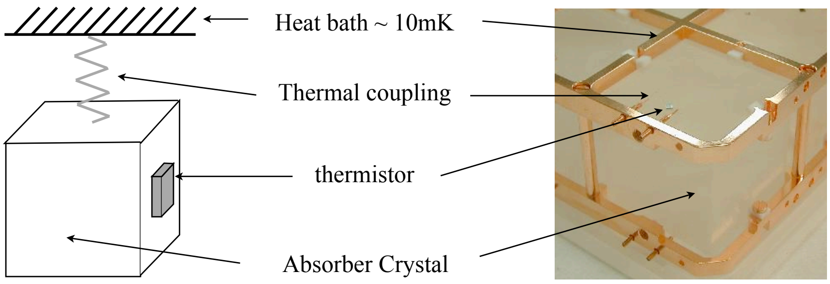

Figure 3.1. Sketch of a bolometer (left) and a Cuoricino bolometer (right).

In order to model the bolometer response function one has to take into account all the passages from the energy release into the crystal that contribute to shape the signal eventually sampled by the ADC. Unfortunately not all the detector parameters are measurable, and those that are measurable often do not have enough accuracy: the model will be then an effective theory of the bolometer, taking advantage of quantities that can be measured accurately. In this work particular emphasis will be placed on the thermistor and on the biasing circuit, which represent our probe to measure temperature variations.

3.1 The CCVR run

The model developed in the next sections has been tested on the data of a measurement that was done to check the first batch of CUORE crystals, the Chinese Crystals Validation Run (CCVR). The detector was made of an array of four crystals with two thermistors each, unfortunately one thermistor was lost during the cooling down, therefore the number of available channels is seven. The biasing circuit of thermistors has been described in section 2.2 and the read-out chain in section 2.5. For what concern the model that will be developed, we can treat the two load resistances as a single resistance (R_L), and we also consider the capacitance (c_p) of the wires that carry the signal from the thermistor to the front end boards. The biasing circuit scheme we will consider is depicted in figure 3.2.

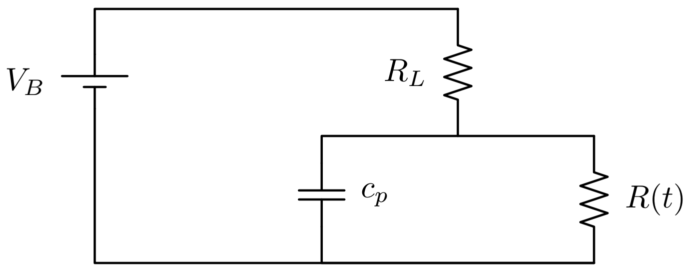

Figure 3.2. Biasing circuit of the thermistor. The thermistor resistance $R(t)$ is in series with a load resistance R_L. The couple of wires used to read the voltage across $R(t)$ has a non negligible capacitance c_p.

The values of the bias voltage (V_B), amplifier gain (G), load resistance (R_L) and wires capacitances (c_p) of each bolometer are reported in table 3.1 together with the measured thermistor resistance R_S (see section 2.5.1). The ADC sampling frequency, the duration of the acquisition window, and the Bessel cutoff frequency were set to 125 Hz, 5.008 s, 12 Hz respectively for all channels. The CCVR detector took data for two months, with calibration runs performed at the beginning and at the end of the measurement.

Table 3.1. Parameters of the CCVR bolometers.

Channel	Crystal	V_B (mV)	G	R_L (G Ω)	c_p (pF)	R_S (M Ω)
1	041	9636	5030	54	255.0	26.57
2	041	8962	3536	54	255.0	39.17
3	011	7685	2241	54	256.4	50.76
4	011	6152	2540	54	255.5	65.27
5	039	9291	2938	54	247.3	40.21
6	007	7364	2938	54	257.6	55.33
7	007	6152	2241	54	255.2	96.81

3.2 The Model

As already stated, when energy is released into the crystal the temperature variation is converted into resistance variation by the thermistor. The resistance variation is then converted by the biasing circuit into a voltage signal that is modified by the amplifier and by the Bessel filter and finally it is sampled by the ADC. The logical path to build a model of a bolometer is to understand each single item that contribute to shape the signal from the energy release up to the ADC. We split this path into three main steps. The first step is the thermal model of the bolometer, describing the physical processes from the energy release that lead to the thermistor temperature variations, the second step is the model of the thermistor, describing the temperature-resistance conversion and the third step is the biasing and read-out circuit model, involving the rest of the signal chain. Our knowledge of bolometer parameters increases along this path, therefore the thermistor, biasing circuit and read-out circuit models will be developed first and then the thermal model.

3.2.1 Thermistor model

The thermistor converts temperature variations into resistance variations according to the relation (see section 2.1.4):

$$R = R_0 \exp\left(\frac{T_0}{T}\right)^{\gamma} . \tag{3.1}$$

Thermistor parameters R_0 and T_0 are not known with the desired accuracy and cannot be measured independently unless a calibrated thermometer is used. The parameter γ instead comes from the quantum physics of the thermistor and can be assumed constant and equal to 1/2. The only parameter that can be measured precisely on the detector is the resistance R_S corresponding to the working temperature T_S (that conversely is not a measurable parameter):

$$R_S = R_0 e^{\left(\frac{T_0}{T_S}\right)^{\gamma}} . \tag{3.2}$$

As we are interested in describing temperature variations from T_S, we define the dynamic resistance as a function of the temperature change (ΔT) as:

$$\Delta R(\Delta T) = R(T_S + \Delta T) - R_S. \tag{3.3}$$

This quantity depends on the same unknown quantities of equation (3.2), therefore we will build the model making approximations of equation (3.3) using the only measurable parameter R_S. The performances of the approximations that will follow have been evaluated using the nominal parameters (2.15) and a nominal working temperature $T_S = 10\,\mathrm{mK}$.

The first thing needed is a rough estimation of the amount of temperature relative variation of the thermistor when energy is released into the crystal. From equation (3.3) we derive $\Delta T/T_S$ as a function of $\Delta R/R_S$:

$$\frac{\Delta T}{T_S} = \left[1 + \frac{\gamma}{\eta} \log\left(1 + \frac{\Delta R}{R_S}\right)\right]^{-\frac{1}{\gamma}} - 1 \tag{3.4}$$

where η is the logarithmic sensitivity (see section 2.1.3),

$$\eta = \left|\frac{d\log(R)}{d\log(T)}\right| = \gamma\left(\frac{T_0}{T_S}\right)^{\gamma} = \gamma \log\frac{R_S}{R_0} \tag{3.5}$$

a quite well measurable parameter that depends on γ and logarithmically on the unknown R_0. The advantage of using the expression (3.4) is that it does not depend on the unknown T_0, T_S and only logarithmically on R_0 through (3.5). Figure 3.3 shows that the error due to the uncertainty on R_0 is small and thus negligible in this case.

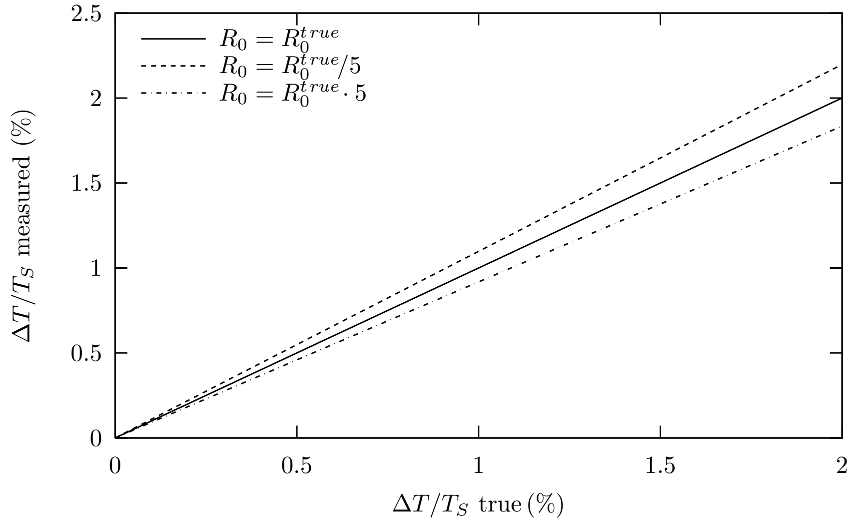

Figure 3.3. Temperature variation of the thermistor ($\Delta T/T_S$) estimated with equation 3.4. The error made using values of R_0 different from the real value R_0^{true} is still acceptable for a rough estimation of the temperature increase.

The value of $\Delta T/T_S$ can be derived from data through the resistance variation ΔR, that can be in turn extracted from the measured voltage variation ΔV (see the biasing circuit of figure 3.2). Neglecting the effect of the parasitic capacitances c_p and of the Bessel filter, it can be expressed as:

$$\Delta R = -\frac{(\Delta V/G)(R_S + R_L)^2}{(\Delta V/G)(R_S + R_L) - R_L V_B}\,. \tag{3.6}$$

In figure 3.4 we show the energy spectrum of a calibration run expressed in terms of $\Delta V/G$ (the voltage across the thermistor), $\Delta R/R_S$ and $\Delta T/T_S$. The tallest peak at $\Delta T/T_S \sim 1.75\%$ corresponds to 5407 keV α particles and the small peak at $\Delta T/T_s \sim 0.85\%$ is generated by 2615 keV γ particles. From the measured values for all channels listed in table 3.2, we conclude that the average $\Delta T/T_S$ is about 0.8% in the 0νDBD region and about 1.7% in the 5407 keV α region.

Given that $\Delta T/T_S \ll 1$, equation 3.3 can be expanded around $T = T_S$:

$$\Delta R = -R_S\left[\eta\frac{\Delta T}{T_S} - \frac{\eta(1+\gamma+\eta)}{2}\left(\frac{\Delta T}{T_S}\right)^2 + \ldots\right] \tag{3.7}$$

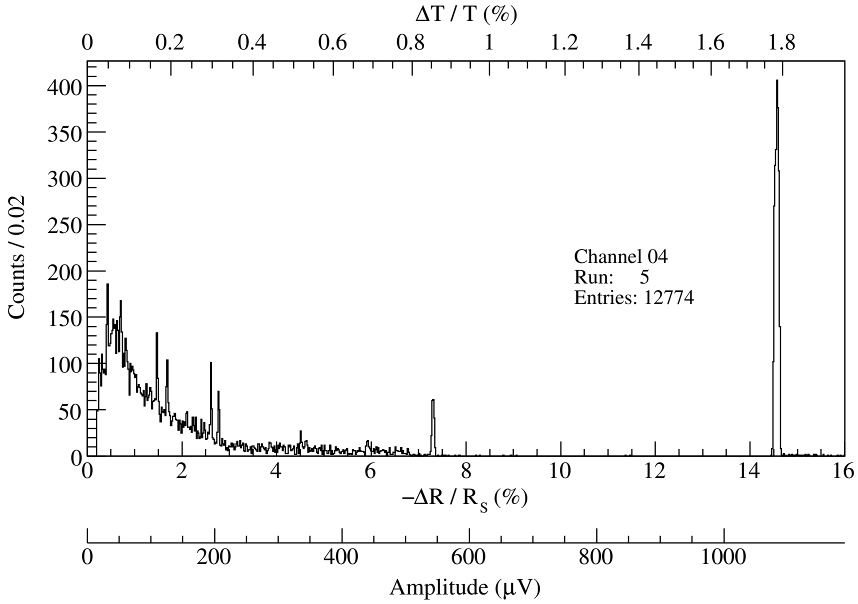

Figure 3.4. Spectrum of channel 4 in terms of $\Delta T/T_S$, $-\Delta R/R_S$, $\Delta V/G$. The tallest peak at $\Delta T/T_S \sim 1.75\%$ corresponds to 5407 keV α particles and the small peak at $\Delta T/T_s \sim 0.85\%$ is generated by 2615 keV γ particles.

Table 3.2. Measured $\Delta V/G, \Delta R/R_S, \Delta T/T_S$.

ch	Yield (μV/MeV)	$-\Delta R/R_S$ (%/MeV)	$\Delta T/T_S$ (%/MeV)	η
1	59	1.2	0.15	8.48
2	92	1.4	0.17	8.67
3	306	4.2	0.51	8.80
4	208	2.8	0.33	8.93
5	198	2.9	0.34	8.68
6	220	2.9	0.34	8.84
7	342	3.1	0.36	9.12

where we used a Taylor expansion up to the 2nd order. The comparison with ΔR calculated from the exact functional form (3.3) shows that the first order approximation has an error of about 5% in the 0νDBD region and that to achieve a smaller error we should take the second order (see figure 3.5). Nevertheless while at the first order the unknown η is just a scale factor of $\Delta T/T_S$, and then not relevant, the inclusion of the second order would imply the knowledge of this parameter. In this phase we do not want to include unknown parameters and since the bolometer resolution in the 0νDBD region is about 0.1% we conclude that this expression is not good.

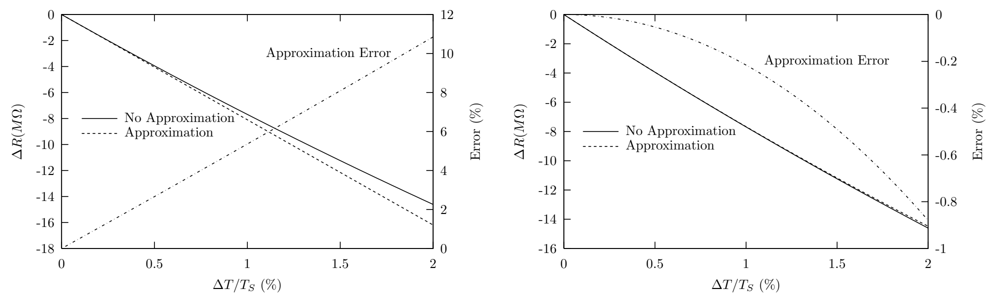

(a) 1st order (b) 2nd order

Figure 3.5. Taylor approximation of ΔR. The 0νDBD region corresponds to $\Delta T/T_S \simeq 0.8\%$.

A better reproduction can be achieved using the exponential approximation:

$$\Delta R = R_S \Big[e^{-\frac{\eta \Delta T}{T_S} + \frac{\eta(\gamma+1)}{2} \left(\frac{\Delta T}{T_S}\right)^2 + \dots} - 1 \Big] \tag{3.8}$$

that performs better than the linear approximation both at first and second order expansions, in particular stopping at the first order we still have an acceptable error ($\sim 0.5\%$) in the 0νDBD region (see figure 3.6). Therefore the approximation we will use for the thermistor model is :

$$\Delta R = R_S \left[e^{-\frac{\eta \Delta T}{T_S}} - 1 \right]. \tag{3.9}$$

These approximations have been tested at a nominal temperature $T_S = 10\,\mathrm{mK}$, but we do not know exactly the real temperature. We checked that expression (3.9) performs well also with T_S different from the nominal 10 mK (see figure 3.7). Moreover from equation (3.2) we see that an uncertainty on T_S has the same effect of an uncertainty T_0 and hence this test applies also to this parameter.
In conclusion, the model for the resistance variation we have developed reproduces the response of an ideal thermistor with an accuracy better than 1% in the 0νDBD region and its accuracy does not depend on the base temperature.
From equations (3.8,3.9) it turns out that the resistance variation is always proportional to the working resistance, hence it is convenient to define the quantity:

$$\Delta\theta = \frac{\Delta R}{R_S}\,. \tag{3.10}$$

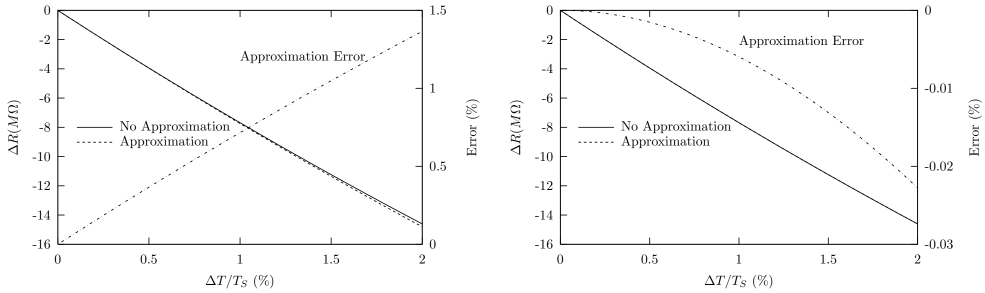

(a) 1st order

(b) 2nd order

Figure 3.6. Exponential approximation of ΔR. The 0νDBD region corresponds to $\Delta T/T_S \simeq 0.8\%$.

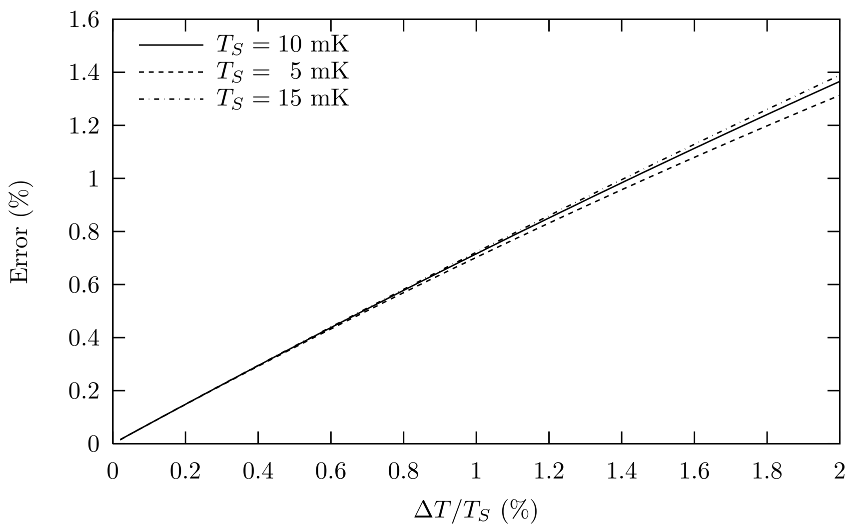

Figure 3.7. Error on ΔR of the 1st order exponential approximation (equation 3.9) at different base temperatures T_S.

3.2.2 Biasing circuit

Solving the electrical circuit of figure 3.2 we obtain the differential equation relating resistance and voltage:

$$\left[\frac{R_L + R(t)}{R(t)}\right] V_{bol}(t) - V_B + R_L c_p \frac{dV_{bol}(t)}{dt} = 0 \tag{3.11}$$

where:

$$V_{bol} = V/G\,, \tag{3.12}$$

is the voltage across the thermistor. The model we are building is based on the variations of the resistance from the measured R_S, these will in turn generate a voltage variation from the measured V_{R_S}. Splitting $R(t)$ and $V(t)$ into static and dynamic contributions

$$R(t) = R_S + \Delta R(t) \qquad\qquad V_{bol}(t) = V_{R_S} + \frac{\Delta V(t)}{G} \tag{3.13}$$

and using (2.19), we obtain the differential equation relating resistance and voltage variations:

$$\left[\frac{R_L + R_S + \Delta R(t)}{R_S + \Delta R(t)}\right]\left[V_B\, G \frac{R_S}{R_S + R_L} + \Delta V(t)\right] - V_B\, G + R_L c_p \frac{d\Delta V(t)}{dt} = 0 \tag{3.14}$$

The polarization circuit equation can be simplified noticing that from equation (2.24) the measured R_S is proportional to R_L:

$$R_S = \frac{R_L}{V_B/V_{R_S} - 1} = \rho R_L; \tag{3.15}$$

using also (3.10) we finally obtain:

$$\left[\frac{1/\rho + 1 + \Delta\theta(t)}{1 + \Delta\theta(t)}\right]\left[\frac{1}{1/\rho + 1} + \frac{\Delta V(t)}{V_B G}\right] - 1 + \frac{R_L c_p}{V_B G}\frac{d\Delta V(t)}{dt} = 0\,. \tag{3.16}$$

Solving this differential equation we get the voltage variation $\Delta V(t)$ corresponding to the resistance relative variation $\Delta\theta(t)$.
Noticing that $\rho \ll 1$ and that $\Delta\theta < 1$, a good approximation that will be used in next sections for rough calculations is:

$$\left[\frac{1/\rho + 1}{1 + \Delta\theta(t)}\right]\left[\frac{1}{1/\rho + 1} + \frac{\Delta V(t)}{V_B G}\right] - 1 + \frac{R_L c_p}{V_B G}\frac{d\Delta V(t)}{dt} = 0\,. \tag{3.17}$$

3.2.3 Bessel filter

As mentioned before the ADC is preceded by an analogical Bessel filter to prevent aliasing effects on the acquired signal. The ADC sampling frequency (f_s) is 125 Hz in order to have enough samples to describe the pulse shape and at the same time not compromise the signal to noise ratio. The Bessel 3dB cut-off (f_b) was set to 12 Hz in order to have enough signal and noise dump at the ADC Nyquist frequency

$(f_s/2)$, therefore its value depends strictly on the choice of f_s. The filter transfer function is:

$$B(\sigma) = \frac{10395}{\sigma^6 + 21\sigma^5 + 210\sigma^4 + 1260\sigma^3 + 4725\sigma^2 + 10395\sigma + 10395} \tag{3.18}$$

where σ is the normalized Laplace variable that expressed in terms of the standard Laplace variable $s = j\omega$ is:

$$\sigma = s\frac{2.703395061}{f_c} . \tag{3.19}$$

The transfer function and the impulse response of this filter are shown in figure 3.8.

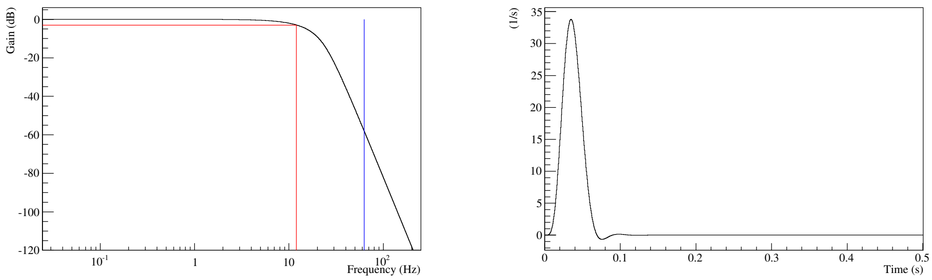

(a) Transfer function

(b) Impulse response

Figure 3.8. Characteristics of the 6-pole Bessel filter with cutoff f_b =12Hz (red line).The blue line corresponds to the Nyquist frequency $f_s/2$.

The filtered signal can be obtained multiplying $V(s)$ (the signal in the frequency domain) by the transfer function $B(s)$ and then transforming back to the time domain:

$$V(t) \rightarrow \mathcal{L}^{-1}[V(s) \cdot B(s)] \tag{3.20}$$

where $V(s) = \mathcal{L}[V(t)]$ and $\mathcal{L}, \mathcal{L}^{-1}$ are the direct and inverse Laplace transforms.

We described and modeled all the steps that go from the thermistor temperature variation to the signal read by the ADC: the thermistor model is not exact but has a good accuracy in the region of interest, the biasing circuit and the Bessel filter are described exactly and, depending on the use, they can be solved with numerical algorithms. The remaining step, the expression of the thermistor temperature when energy is released in the crystal, is decribed in the next section.

3.2.4 Thermal model

In figure 3.9 the thermal circuit representing the system composed by crystal, crystal supports and thermistor is sketched. The crystal C_T is connected with the thermistor through the glue spots K_g and with the supports through a Kapitza conductance K_{ts}. A thermistor can be represented as a two stages system composed by the lattice and the electron gas, each one with its own capacity and connected between them by means of a conductance K_e. The lattice capacity is negligible and is not shown in the figure, so it can be assumed that the lattice directly discharges through the gold wires connected to the heat sink K_b. The electron gas capacity C_{el}, and conductance K_{el} are in parallel with the power generator P that represents the electrothermal feedback generated when the thermistor is heated (see section 2.2): its resistance varies and hence also the power generated through Joule effect varies, modifying the thermal response. On the left side of the circuit, we have the crystal supports that can be simply represented by means of their capacity C_s and conductance to the main bath K_s.

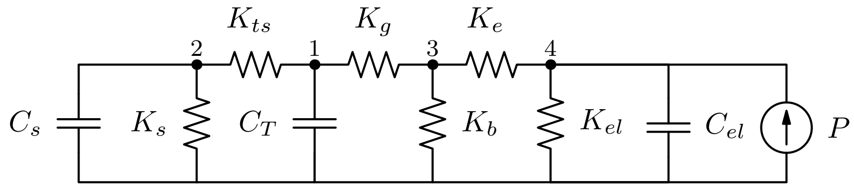

Figure 3.9. Thermal circuit of a bolometer.

Values for 5x5x5 Cuoricino bolometers are (K in W/K, C in J/K) [55]:

$$\begin{array}{lll} C_T = 2.29 \cdot 10^{-3}\, T^3 & C_{el} = 9.9 \cdot 10^{-9}\, T & C_s = 5 \cdot 10^{-9} \\ K_s = 2 \cdot 10^{-9} & K_{ts} = 1 \cdot 10^{-9} & K_g = 2.34 \cdot 10^{-3}\, T^3 \\ K_b = 4.8 \cdot 10^{-5} T^{2.4} & K_e = 0.7 \cdot T^{4.37} & K_{el} < 5 \cdot 10^{-11} \end{array} \tag{3.21}$$

The power $P(t)$ dissipated on the thermistor in static conditions is:

$$P_S = \left(\frac{V_B}{R_L + R_S}\right)^2 R_S\,, \tag{3.22}$$

using typical values of the parameters we have that $P_S \sim 1\,\text{pW}$. In dynamic conditions the power can be calculated from (3.11):

$$P(t) = \frac{V_{bol}(t)^2}{R(t)} = \left[\frac{c_p R_L V'_{bol}(t) - V_B}{R_L + R(t)}\right]^2 R(t) \tag{3.23}$$

that using (3.16) and (3.22) becomes:

$$P(t) = P_S \frac{\left[1 + \frac{1+\rho}{\rho}\frac{\Delta V(t)}{V_B\, G}\right]^2}{1 + \Delta\theta(t)}. \tag{3.24}$$

If instead of the full biasing equation (3.16) we use the approximation (3.17) the power becomes:

$$P(t) \simeq P_S \left(1 - \frac{c_p\, R_L\, V'(t)}{V_B\, G}\right)^2 (1 + \Delta\theta(t)). \tag{3.25}$$

3.2.5 Simplified model without temperature dependences

In this section we will find the solution of the thermal circuit neglecting the temperature dependence of each element. Even if we are not taking into account a real bolometer, finding such approximate solution is useful to get into the problem and

understand the dynamic behaviour that arises when particles release energy into the crystal.
Power conservation in the nodes 1,2,3 and 4 of figure 3.9 reads:

$$C_T \frac{dT_1}{dt} + K_{ts}\,(T_1 - T_2) + K_g\,(T_1 - T_3) = 0 \tag{3.26a}$$

$$C_s \frac{dT_2}{dt} + K_s\,T_2 + K_{ts}\,(-T_1 + T_2) = 0 \tag{3.26b}$$

$$K_b\,T_3 + K_g\,(-T_1 + T_3) + K_e\,(T_3 - T_4) = 0 \tag{3.26c}$$

$$C_{el} \frac{dT_4}{dt} - P(t) + K_{el}\,T_4 + K_e\,(-T_3 + T_4) = 0\ . \tag{3.26d}$$

Absolute temperatures in static conditions T_{i_0} can be found by omitting derivatives in (3.26), setting the electrothermal feedback to (3.22) and adding the base temperature T_B that can be considered as a common ground. Dynamic conditions arise when capacitors are heated at $t = 0$. Temperatures in each node can be expressed as the sum of the static ones plus an increase that includes time dependences. Substituting

$$T_i(t) = T_{i_0} + \Delta T_i(t) \tag{3.27}$$

into (3.26) leads to the same system of differential equations with ΔT_i in the place of T_i and the power $P(t)$ replaced by the dynamic part of the electrothermal feedback $\Delta P(t) = P(t) - P_S$. This term links the thermal circuit with the biasing circuit and in principle we should add equation (3.16) to the set of differential equations (3.26). However we will demonstrate in the following that if we decide to neglect the temperature dependence of conductances and capacitances we can decouple the thermal circuit from the electrical circuit. Using (3.25) and the fact that $c_p\,R_L\,V'(t)/V_B\,G \ll 1$, the power variation can be rewritten as:

$$\Delta P(t) \simeq P_S \left[\left(1 - 2\frac{c_p\,R_L\,V'(t)}{V_B\,G} \right) (1 + \Delta\theta(t)) - 1 \right] \tag{3.28}$$

that substituting the first order voltage and resistance variations

$$\Delta\theta \simeq -\eta \frac{\Delta T}{T_S} \qquad\qquad \Delta V \simeq \frac{V_B\,G}{R_L} R_S \Delta\theta \tag{3.29}$$

and neglecting second order terms, becomes:

$$\Delta P(t) \simeq -\frac{\eta\,P_S}{T_S} \Delta T(t) + 2\frac{\eta\,P_S\,c_p\,R_S}{T_S} \Delta T'(t)\,. \tag{3.30}$$

Substituting the above expression into the differential equation of the thermistor (3.26d)

$$C_{el}\,\Delta T_4' + K_{el}\,\Delta T_4 + K_e\,(-\Delta T_3 + \Delta T_4) + \frac{\eta\,P_S}{T_S} \Delta T_4 - 2\frac{\eta\,P_S\,c_p\,R_S}{T_S} \Delta T_4' = 0 \tag{3.31}$$

shows that the electrothermal feedback can be interpreted as a correction to the electrons capacitance and conductance:

$$C_{eff} = C_{el} - 2\frac{\eta\,P_S\,c_p\,R_S}{T_S} \qquad\qquad K_{eff} = K_{el} + \frac{\eta\,P_S}{T_S}\,. \tag{3.32}$$

Now that the electrothermal feedback has been included we can move to the solution of the system of differential equations. We turn into the Laplace domain that eases the calculations and has the advantage of including initial conditions directly into the equations:

$$s\,C_T\,\Delta T_1 - E_1 + K_{ts}\,(\Delta T_1 - \Delta T_2) + K_g\,(\Delta T_1 - \Delta T_3) = 0 \tag{3.33a}$$

$$s\,C_s\,\Delta T_2 - E_2 + K_s\,\Delta T_2 + K_{ts}\,(-\Delta T_1 + \Delta T_2) = 0 \tag{3.33b}$$

$$K_b\,\Delta T_3 + K_e\,(\Delta T_3 - \Delta T_4) = 0 \tag{3.33c}$$

$$s\,C_{eff}\,\Delta T_4 - E_4 + K_{eff}\,\Delta T_4 + K_e\,(-\Delta T_3 + \Delta T_4) = 0 \tag{3.33d}$$

where all the ΔT_i's depend on the Laplace frequency s and E_1, E_2, E_4 are the energies released in the capacitances at $t = 0$. In the condition of a particle releasing its energy E inside the crystal ($E_1 = E$, $E_2 = 0$, $E_4 = 0$) the thermistor temperature is:

$$\Delta T_4(s) = A' \frac{(s - z_1)}{(s - p_1)(s - p_2)(s - p_r)} \tag{3.34}$$

where $A' = E\frac{K_e K_g}{C_T C_{eff}(K_b + K_e + K_g)}$, $z_1 = \frac{K_s + K_{ts}}{C_s}$ and p_i's are the roots of the polynomial:

$$D(s) = d_0 + d_1 s + d_2 s^2 + s^3 \tag{3.35}$$

where the d_i parameters are complicated combinations of the circuit elements and are not reported explicitly. Given the circuit configuration one has that all the p_i poles are real and negative ($p_i = -\frac{1}{\tau_i}$). Transforming back in the time domain equation (3.34) we obtain:

$$\Delta T_4(t) = A' \cdot \left[\underbrace{\frac{z_1 - p_r}{(p_1 - p_3)(p_r - p_2)}}_{-a} e^{p_r t} + \underbrace{\frac{z_1 - p_1}{(p_1 - p_2)(p_r - p_1)}}_{b} e^{p_1 t} + \underbrace{\frac{z_1 - p_2}{(p_2 - p_1)(p_2 - p_r)}}_{c} e^{p_r t} \right] \tag{3.36}$$

It is useful for interpolation purposes to put in evidence independent parameters. We notice that $b + c = a$, so defining $\alpha = b/a$ and $A'\,a = A$ we finally obtain the expression of the thermistor temperature variation:

$$\Delta T_4(t) = A \left(-e^{-\frac{t}{\tau_r}} + \alpha e^{-\frac{t}{\tau_1}} + (1 - \alpha) e^{-\frac{t}{\tau_2}} \right) \tag{3.37}$$

where $0 < \alpha < 1$. The above equation describe a pulse with one rise time constant and two decay time constants.

3.2.6 Fit to data

We modeled all the elements from the energy release into the crystal that contribute to shape the acquired signal, putting them together we can derive a function to fit real pulses. The weakest element is the thermal model where we reduced the calculations to a simplified version without temperature dependences, moreover while we know R_S and the parameters of the biasing and read-out circuits (V_B, G, R_L, c_p, f_b) it is impossible to measure independently the elements of the thermal part. The measured parameters (3.21) are just approximate, and are not suitable to be included in the fit as constants. The effective parameters (A, τ_r, α, τ_1, τ_2) instead will be extracted from the data fit. Together with these parameters, we will also fit the onset time t_0 of the pulse in order to align the function with the data. The fit function is not writable analytically because not all the parts of the model can be solved analytically. The temperature of the thermistor (3.37) is analytically converted into resistance relative variations $\Delta\theta(t)$ using (3.9,3.10):

$$\Delta\theta(t) = e^{-\frac{\eta\Delta T(t)}{T_S}} - 1 \ . \tag{3.38}$$

We see that the unknown parameter η/T_S multiplies the parameter A that is going to be fitted, so we define the effective amplitude parameter $A_n = A\,\eta/T_S$ entering the resistance relative variation expression:

$$\Delta\theta(t) = \exp\left[-A_n\left(-e^{-\frac{t}{\tau_r}} + \alpha e^{-\frac{t}{\tau_1}} + (1-\alpha)e^{-\frac{t}{\tau_2}}\right)\right] - 1 \ . \tag{3.39}$$

To obtain the corresponding voltage variation we have to solve the biasing circuit equation (3.16) that unfortunately is not solvable analytically, $\Delta V(t)$ is therefore obtained form $\Delta\theta(t)$ using the numerical method Runge-Kutta [56]. Finally $\Delta V(t)$ is filtered with the Bessel (equation 3.20) by means of the FFT-convolution method described in [57]. The interpolation of a 2615 keV γ pulse on channel 4 is shown in figure 3.10 and the fitted values of the parameters are quoted in table 3.3.

Table 3.3. Parameters fitted on a signal of channel 4 generated by a 2615 γ particle.

t_0 (s)	1.011230	$\pm$	0.000028
A_n (A.U)	0.12346	$\pm$	0.00011
α	0.91533	$\pm$	0.00040
τ_{d1}(s)	0.15720	$\pm$	0.00018
τ_{d2} (s)	0.7487	$\pm$	0.0024
τ_r (s)	0.020897	$\pm$	0.000046

The fit performs pretty well on data except in the first part of the pulse. This is clearly visible in the plot of the residuals. This mismatch appears in different sizes on all channels making the fit imperfect. It could be due either to some error on the read-out circuit parameters or, more likely, to the fact that the thermal model does not include the temperature dependences of all elements and the electrothermal feedback. The shape parameters averaged over a large number of fits of all channels are quoted in table 3.4, we see that the average χ^2/ndf is never one as expected if the model were exact.

These results indicates that the model is pretty close to reality but not perfect. By adding new free parameters in the thermal part we could improve the χ^2/ndf but we would never know if the new model is better: the correlations between the parameters will increase without adding new independent information. Nevertheless, as it will be shown in the next sections, the model is sufficiently accurate as is, and is able to reproduce the main features of the observed data.

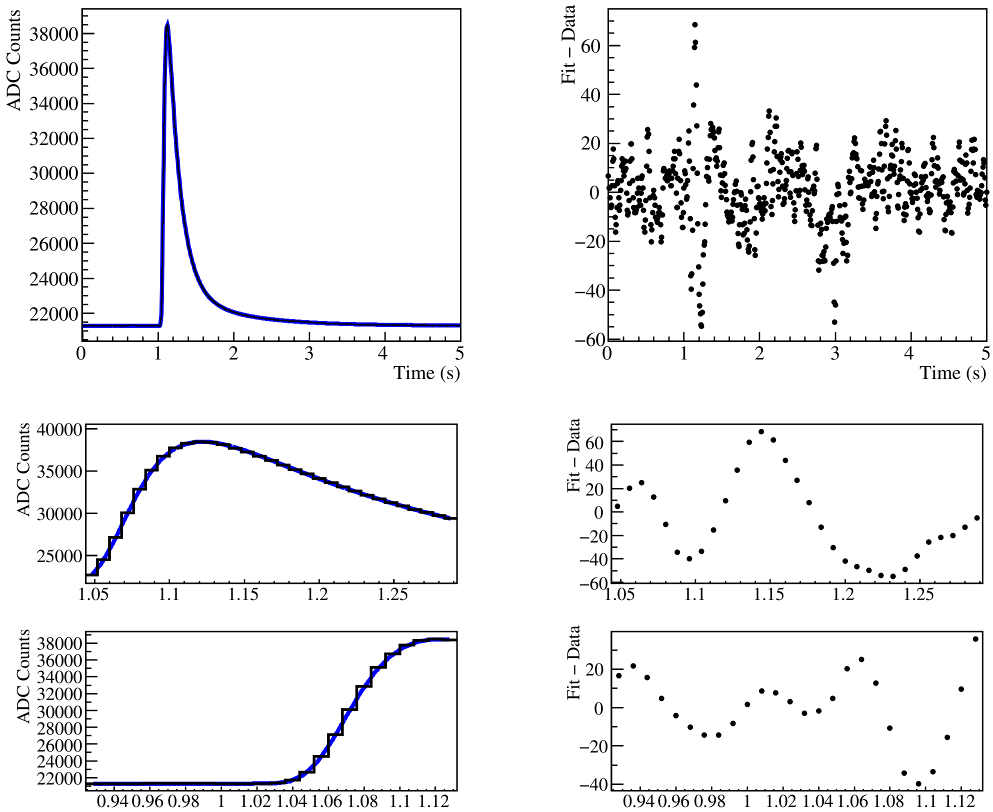

Figure 3.10. Interpolation of a 2615 keV pulse recorded on channel 4. Left column represents signal with superimposed fit function (top), zoom of the top (middle) and zoom of the rise (bottom). Right column represents the fit residuals.

Table 3.4. Average shape parameters fitted on 2615 keV pulses.

ch	τ_r (s)	α	τ_{d1} (s)	τ_{d2} (s)	χ^2/ndf
1	0.031804	0.83249	0.11205	0.9001	2.0
2	0.026263	0.87070	0.10898	0.8988	1.9
3	0.021362	0.94919	0.14726	0.7688	5.4
4	0.020702	0.91725	0.15822	0.7824	3.1
5	0.032546	0.90648	0.21780	0.8712	3.1
6	0.033858	0.91983	0.12191	0.6804	5.3
7	0.011843	0.94753	0.11998	0.8504	6.0

3.2.7 Response function simulation

One of the purposes of this work was to build a signal simulator, a tool that could be used to test the data-analysis algorithms, to define trigger parameters and estimate efficiencies. Pulses have been simulated using the measured parameters of table 3.1 and the estimated thermal parameters of table 3.4. With this set of parameters we have all the information needed to simulate pulses according to the model described in this work. To reproduce pulses of different energies, the amplitude A_n has been generated from the amplitude spectrum of each channel in order to match the measured amplitude.

From figure 3.11 we see that the rise time and the decay time of the real pulses, defined as the time difference between the 10% and the 90% of the pulse amplitude for the rise time, and between 90% and 30% for the decay time, show a clear correlation with the pulse amplitude.

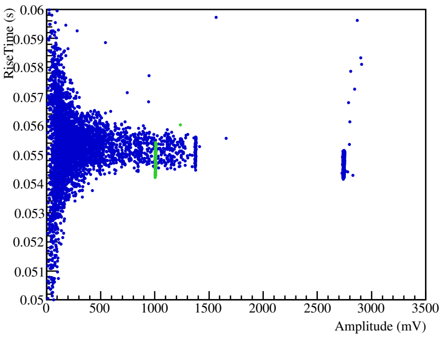

(a) Rise Time vs Amplitude

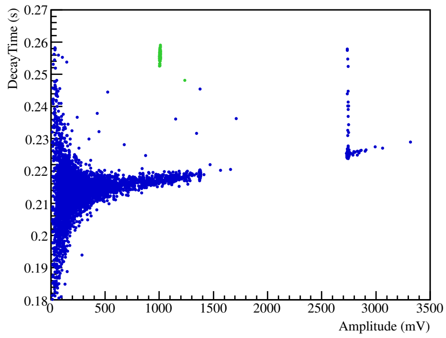

(b) Decay Time vs Amplitude

Figure 3.11. Pulse shape correlation with amplitude, signal (blue) and heater (green) pulses. The points at $\sim 2800\,\mathrm{mV}$ correspond to the 5407 keV α and the points at $\sim 1400\,\mathrm{mV}$ correspond to the 2615 keV γ. The shape of particle pulses has a manifest dependence on the pulse amplitude. The shape of the heater pulses is clearly different from that of particle ones.

To reproduce this behavior we should estimate the thermal parameters of (3.37) at each energy and not just at 2615 keV: we are lead to think this because the thermal shape $\Delta T(t)$ in principle contains an energy dependence due to the fact that each capacitance and conductance of the bolometer has a temperature dependence.
However the thermistor and biasing circuit models also contain a dependence of the pulse shape on its amplitude that seems to go in the same direction of the observed data. In the following we will demonstrate that most of the energy dependence is due to the fact that the thermal shape $\Delta T(t)$ is modified by the thermistor and the biasing circuit as they have a non linear response.

From expression (3.17), we have that the relationship between $\Delta V(t)$ and $\Delta\theta(t)$ can be rewritten as:

$$\Delta V(t) + [1 + \Delta\theta(t)]\frac{R_L c_p \rho}{1+\rho}\frac{\Delta V(t)}{dt} = \frac{\rho V_B G}{1+\rho}\Delta\theta(t) \tag{3.40}$$

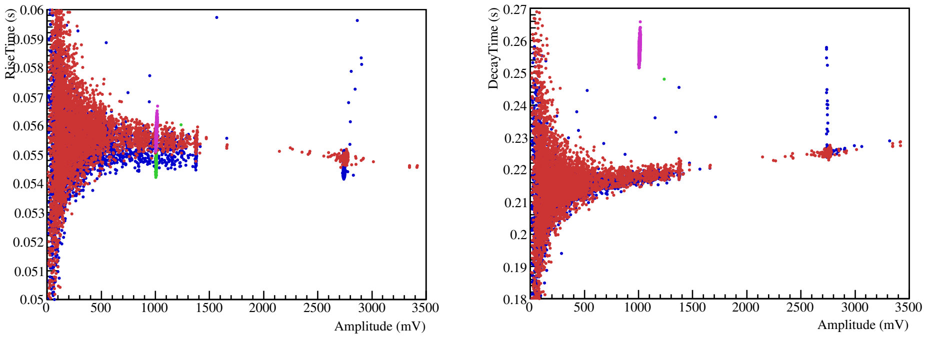

(a) Rise Time vs Amplitude (b) Decay Time vs Amplitude

Figure 3.12. Generated signal (red) and heater (magenta) pulses superimposed on data.

that can be interpreted as an RC filter with a cutoff

$$\omega_p(t) = \frac{1+\rho}{[1+\Delta\theta(t)]\, R_L\, c_p \rho} \tag{3.41}$$

that depends on the input signal $\Delta\theta(t)$. Reminding that $\Delta\theta(t)$ is negative, the cut off increases with the pulse amplitude making the signal $\Delta V(t)$ *faster*. On the other hand the form of $\Delta\theta(t)$ (see equation (3.39)) makes the signal *slower* at higher amplitudes. In principle these two effects compete in the modification of the rise time and decay time, however given that the decay time is much higher than $1/\omega_p$ the fastening effect applies mainly to the rise time.

The result of a simulation made with constant thermal parameters is shown in figure 3.12, where we see that the shape dependence on energy is well matched in the case of the decay time while there is a shift in the rise time. This shift might be due to the fact that, as already mentioned, the fit experiences problems in the first part of the pulse and will be investigated further in the next chapters.

3.2.8 Amplitude dependence on the working temperature

The bolometer working temperature varies in time because of normal fluctuations of the cryostat temperature. This variation ΔT_B shifts the working point of the bolometer modifying its response. Looking at the amplitude of the pulse there is a clear correlation with its baseline and hence with the working temperature (see figure 3.13).

As for the case of shape parameters this effect could be due to the fact that the thermal elements of the bolometer depend on the temperature, nevertheless we will show that the thermistor model can reproduce this effect without taking into account the thermal model at all.

When the base temperature changes, the resistance varies according to the expression (see equation 3.10):

$$\Delta R_B = R_S \Big[e^{-\eta \frac{\Delta T_B}{T_S}} - 1 \Big] \,. \tag{3.42}$$

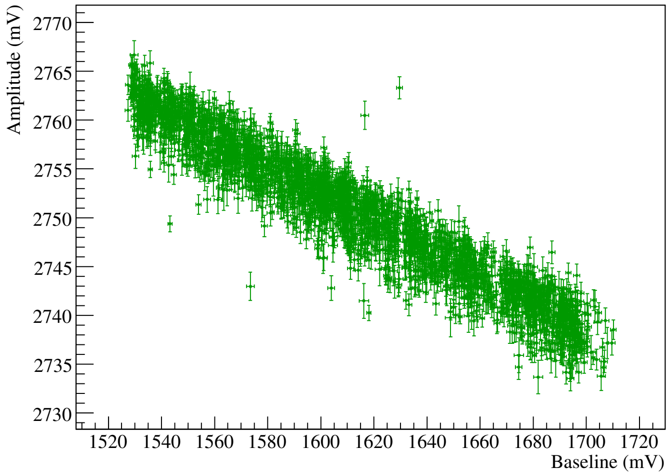

Figure 3.13. Correlation of the amplitude of 5.4 MeV pulses with baseline.

The total resistance variation due to a temperature variation ΔT_E caused by an energy release into the bolometer is then:

$$\Delta R_E^{tot} = R_S \left[e^{-\eta \frac{\Delta T_B + \Delta T_E}{T_S}} - 1 \right] . \tag{3.43}$$

However the amplitude measured in figure 3.13 refers to the height of the signal with respect to its baseline, that in terms of resistances variations is (see figure 3.14):

$$\Delta R_E = \Delta R_E^{tot} - \Delta R_B \, . \tag{3.44}$$

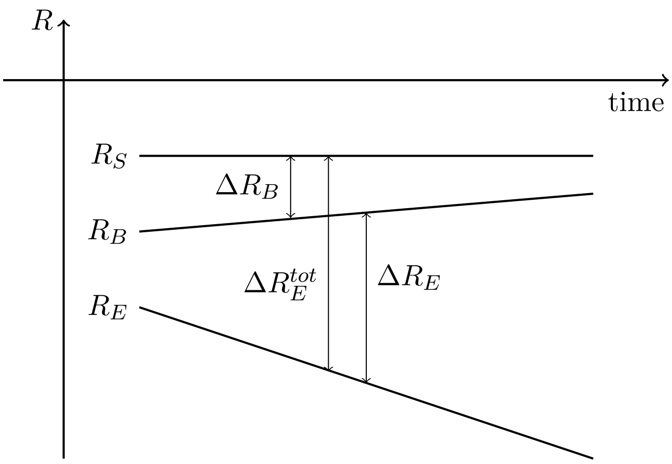

Figure 3.14. Resistance variations.

Under the hypothesis that the temperature increase ΔT_E does not depend on ΔT_B (that implies that the thermal elements do not depend on temperature) we have:

$$\Delta R_E(\Delta T^B) = e^{-\eta \frac{\Delta T^B}{T_S}} \Delta R_E(\Delta T^B = 0) \tag{3.45}$$

that in terms of the baseline resistance variation becomes:

$$\Delta R_E(\Delta R^B) = \left[1 + \frac{\Delta R^B}{R_S}\right] \Delta R_E(\Delta R^B = 0)\ . \tag{3.46}$$

The above equation describes a linear dependence of the resistance variation (and hence the pulse amplitude) on the baseline variation, the same effect that we have seen in the data.

Now if instead of treating ΔT_E as constant we suppose that it does depend on temperature, we could write the dependence in the generic form:

$$\Delta T_E(T) = \alpha\, T^\beta \tag{3.47}$$

where β is the effective and unknown exponent generated by the thermal circuit. Expanding at the first order around T_S we obtain the dependence of the thermal amplitude on the baseline temperature variation:

$$\Delta T_E(T_S + \Delta T_B) = \Delta T_E(T_S) + \alpha\, \beta T_S^{\beta-1} \Delta T_B \tag{3.48}$$

or equivalently

$$\Delta T_E(T_S + \Delta T_B) = (1 + \beta \frac{\Delta T_B}{T_S}) \Delta T_E(T_S)\ . \tag{3.49}$$

Introducing the above equation into (3.44) and approximating at the first order, we obtain the expression of the resistance variation when ΔT_E depends on ΔT_B:

$$\Delta R_E(\Delta R^B) \simeq \left[1 + \frac{\eta - \beta}{\eta} \frac{\Delta R^B}{R_S}\right] \Delta R_E(\Delta R^B = 0)\ , \tag{3.50}$$

from which we conclude that the thermistor contribution is anyway the larger one because of the high value of the logarithmic sensitivity η (~ 9) with respect to any reasonable value of β (if simply $\Delta T_E = E/C_T$, from (3.21) we have $\beta = -3$).

3.2.9 Extraction of R_S from the relationship between amplitude and baseline

To give a proof of the fact that the thermistor model explains the amplitude vs baseline relationship we could make a simulation and compare it with real data, as we did for the shape parameters. We will instead develop a procedure to extract the bolometer resistance R_S from the relationship between amplitude and baseline. The obtained value of R_S will be compared with the measured one to check the accuracy of the model.
Dividing (3.46) by R_S and defining the constant:

$$C = \frac{\Delta R_E(\Delta R_B = 0)}{R_S}\ , \tag{3.51}$$

we rewrite the resistances relationship in terms of $\Delta\theta$:

$$\Delta\theta_E = (1 + \Delta\theta_B) C\ . \tag{3.52}$$

$\Delta\theta_E$ is the resistance variation corresponding to the amplitude of the pulse, where the signal is maximum, and $\Delta\theta_B$ corresponds to the baseline, where the signal is flat. In both cases the voltage derivative is zero and the biasing circuit equation (3.16) reduces to:

$$\left[\frac{1/\rho + 1 + \Delta\theta}{1 + \Delta\theta}\right]\left[\frac{1}{1/\rho + 1} + \frac{\Delta V}{V_B G}\right] - 1 = 0 \ . \tag{3.53}$$

Extracting $\Delta\theta$ out of the above equation we have:

$$\Delta\theta_B = -\frac{(1+\rho)^2}{\rho(1+\rho - V_B\, G/\Delta V^B)} \tag{3.54}$$

$$\Delta\theta_E + \Delta\theta_B = -\frac{(1+\rho)^2}{\rho(1+\rho - V_B\, G/(\Delta V^B + \Delta V^E))} \ . \tag{3.55}$$

While the voltage variation is well defined in the case of pulses (ΔV^E), being the height of the pulse with respect to the baseline, in the case of the baseline variation (ΔV^B) we need a reference voltage. This reference should be the baseline value (V_S) corresponding to V_{R_S} (see section 2.5.1), but unfortunately it has not been measured. We can use the baseline of the events acquired right after the R_S measurement as V_S, the baseline variation is then computed as:

$$\Delta V^B = V_{Base} - V_S \ . \tag{3.56}$$

Substituting $\Delta\theta_E$ and $\Delta\theta_B$ in terms of the voltage differences, equation (3.52) becomes:

$$\frac{(1+\rho)^2}{\rho(1+\rho - V_B\, G/(\Delta V^E + \Delta V^B))} = (C+1)\left(\frac{(1+\rho)^2}{\rho(1+\rho - V_B\, G/\Delta V^B)}\right) - C \tag{3.57}$$

from which we extract ΔV^E in terms of ΔV^B:

$$\Delta V^E = \frac{C\,\left(\Delta V^B + \Delta V^B\,\rho + V_B\, G\right)\,\left(\Delta V^B + \Delta V^B\,\rho - \rho\, G\, V_B\right)}{(1+\rho)\,\left((1+\rho+C\,\rho)\; V_B\, G - C\,\Delta V^B\;(1+\rho)\right)} \ . \tag{3.58}$$

To obtain the linear relation $\Delta V^E = m\,\Delta V^B + q$ seen on data we expand the above equation around $\Delta V^B = 0$:

$$q \;= \Delta V^E\big|_0 = -\frac{C\,\rho\, V_B G}{(1+\rho)(1+\rho+C\,\rho)} \tag{3.59}$$

$$m \;= \left.\frac{d\Delta V^E}{d\Delta V^B}\right|_0 = C\frac{1-(1+C)\,\rho^2}{(1+\rho+C\,\rho)^2} \ . \tag{3.60}$$

With the (q, m) parameters estimated from linear fits on data (see figure 3.15) we calculate back the value of ρ:

$$\rho = \frac{-m\,(V_B G)^2 - 2q^2 - V_B G\sqrt{(m\, V_B G)^2 + 4q^2 + 4mq^2}}{2(q^2 - q\, V_B G)}, \tag{3.61}$$

and finally the value of the working resistance:

$$R_S = \rho R_L \, . \tag{3.62}$$

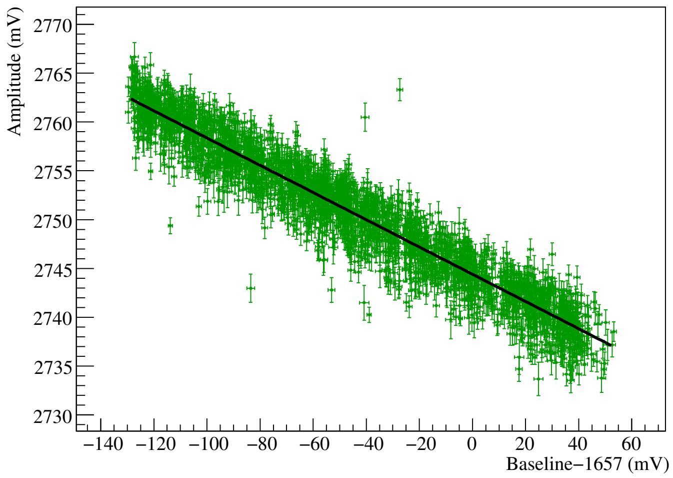

Figure 3.15. Fit of the Amplitude vs Baseline relationship for 5.4 MeV pulses triggered on channel 4.

Table 3.5. Working resistances estimated from amplitude vs baseline fits on data.

ch	q (mV)	m (10^{-2})	R_S^E (MΩ)	R_S (MΩ)	V_S (mV)
1	1580.06 ± 0.03	-6.22 ± 0.04	28.3 ± 0.2	26.6	1613
2	1727.91 ± 0.03	-7.13 ± 0.05	41.3 ± 0.3	39.2	1537
3	3474.51 ± 0.03	-20.26 ± 0.04	53.7 ± 0.1	50.8	1597
4	2744.40 ± 0.03	-13.95 ± 0.04	68.0 ± 0.2	65.3	1657
5	3032.20 ± 0.04	-14.63 ± 0.07	41.0 ± 0.2	40.2	1558
6	3343.82 ± 0.05	-13.62 ± 0.03	61.2 ± 0.1	55.3	1514
7	3962.94 ± 0.04	-15.49 ± 0.05	100.2 ± 0.3	96.8	1415

In table 3.5 the estimated value of the resistances (R_S^E) is compared with the measured one (R_S). The agreement is quite good considering that the error on R_S is unknown (see section 5.2), and proves that the thermistor model describes well the dependence of the response function with the baseline temperature.

With the model developed so far we have been able to build a tool to fit the pulses and extract the relevant parameters. Using these parameters we built a pulse simulator that is able to emulate the shape dependence on energy as well as the amplitude dependence on the base temperature.

Chapter 4

Thermal response analysis

It has been shown that the behavior of the data can be explained assuming that the thermal response ΔT does neither depend on the energy released in the bolometer nor on the variation of the bolometer temperature. The non-linearities of the voltage signal ΔV seems to be generated by the thermistor and by the biasing circuit. Here we propose an algorithm to extract ΔT from the measured ΔV, and we will make the data analysis using ΔT. Being the thermal response more regular than the voltage signal, an improvement is expected in the data analysis. This algorithm has the advantage that it does not take into account the thermal model at all, a topic in which our knowledge is very small, limiting the analysis just to a description of ΔT without trying to explain its origin. We will compare the data analysis based on ΔT with the standard analysis used so far with bolometers that is instead based on ΔV.

4.1 Data analysis procedure

The standard analysis of bolometer data is relatively simple, implying just few steps from the raw data to the energy spectrum. The first step is the pulse amplitude evaluation with the optimum filter algorithm [58]. The second step is the correction of the amplitude drift seen in the previous chapter that is removed de-correlating the dependence on the baseline. This is obtained by fitting with a line $A = m\,B + q$ the amplitude (A) versus baseline (B) relationship of a fixed energy pulse, for example the 5.4 MeV ^{210}Po, and applying the correction to the amplitude of all events:

$$A' = \frac{A}{m\,B + q} C \tag{4.1}$$

where C is an arbitrary constant usually set to 5000. When crystals are sufficiently old the intensity of the ^{210}Po (half-life = 138 days) becomes too low to probe the baseline with enough frequency, thus the heater is used to emulate pulses of fixed energy and frequency. In the CCVR run there was no need for the heater because the crystals were new and there was enough ^{210}Po to stabilize against it. The CUORE experiment will use crystals somewhat aged by the time spent in storage and hence will operate with the heater: looking forward we will do the analysis of the CCVR experiment using the heater instead of the ^{210}Po line.
The last step is the calibration. Calibration runs are usually performed at the beginning of the measurement inserting Thorium sources in the cryostat, the procedure is

usually repeated every 1-2 months. The calibration function and the issues related to it will be discussed later in this chapter.

4.2 The Thermal Response algorithm

In this section we describe a digital filter that, based on the model described in the previous chapter, transforms the voltage samples acquired by the ADC (ΔV) into samples proportional to the temperature variation of the thermistor (ΔT).

The first step consists in extracting the resistance relative variation $\Delta\theta$ from ΔV, using equation (3.16) we have that for each sampled point i:

$$\Delta\theta_i = -\frac{\Delta V_i(1+1/\rho) + R_L c_p \Delta V_i'}{\Delta V_i + R_L c_p \Delta V_i' - V_B G/(1+\rho)} \tag{4.2}$$

where the derivative at the i-th point $\Delta V_i'$ is estimated as:

$$\Delta V_i' = \frac{V_{i+1} - V_{i-1}}{2\Delta t} \tag{4.3}$$

and Δt is the sampling interval.
The temperature variation ΔT_i is then extracted from $\Delta\theta_i$ using (3.9,3.10):

$$\eta \frac{\Delta T_i}{T_S} = -\log(\Delta\theta_i + 1)\ . \tag{4.4}$$

The presence of the unknown quantity η/T_S is not a problem because it can be interpreted as a scale factor. Moreover, as our target is to substitute ΔT (or something proportional to it) into the same analysis chain used for ΔV, we rescale the left hand side of (4.4) as it is too small compared to ΔV (see table 3.2): the scale factor k that has been applied to all channels is 21000. We finally define the dimensionless quantity ΔS

$$\Delta S_i = -k\ \log\left(\Delta\theta_i + 1\right), \tag{4.5}$$

and the data based on it will be called "TR" (Thermal Response).

This algorithm has the advantage of being a one-to-one transformation of each ΔV sample into a ΔS sample, so there are no cases where it is not defined. Comparing a ΔS pulse (TR) with the original ΔV (STD) we observe that the TR pulse is faster than the STD and the high frequency noise is higher (see figure 4.1). Both effects are due to the fact that we removed the low pass filter generated by the parasitic capacitances. The TR algorithm can be thought as a digital, high-pass filter applied to the data sampled by the ADC.
One might worry that the higher noise worsen the resolution, nevertheless the optimum filter algorithm used to estimate the pulse amplitude is not sensitive to this effect: the expression of the signal (S) to noise (N) ratio (SNR) is indeed:

$$\mathrm{SNR}^2 = \int \frac{|S(\omega)|^2}{|N(\omega)|^2} d\omega\,, \tag{4.6}$$

so multiplying the signal and the noise by the same transfer function does not affect the resolution.

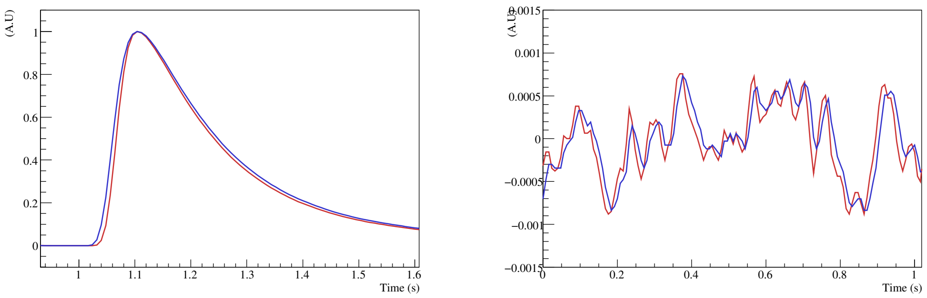

(a) signal (b) noise

Figure 4.1. Comparison between STD (blue) and TR (red) timelines. TR timelines have more high frequency components, as the low-pass filter generated by the bolometer resistance and the wires capacitance is removed.

4.3 Check of the TR algorithm on MonteCarlo data

Before the application of the TR analysis to data, we checked that it performs as expected on MonteCarlo simulations based on the model described in the previous chapter. Generated data contain all the features of the model: once the TR analysis is applied we expect no shape dependence on energy and no amplitude dependence on the baseline, moreover the resolution has to be the same of the STD analysis to be competitive with it. Data has been generated sampling amplitudes from an input spectrum measured with the STD analysis to check the shape correction. These data are not suitable for the resolution estimation because, being generated from measured spectra, contain peaks that are already smeared. To overcome this problem we generated heater events with monochromatic amplitude, without sampling from the real spectrum. As the generator reproduces the amplitude vs baseline drift, that also worsen the resolution, the intrinsic resolution has been evaluated on a separated set of data, generated without the amplitude drift. Finally the checked quantities are:

- slope of rise time vs energy, normalized to the rise time at zero energy.
- slope of decay time vs energy, normalized to the decay time at zero energy.
- slope of heater amplitude vs baseline.
- heater amplitude resolution (tested on data generated without the amplitude vs baseline feature).

The slopes are expected to be zero while the resolution should be the same obtained with the standard analysis.
In figure 4.2 the shape parameters of channel 4 are compared for the STD and the TR analysis, showing the expected performance of the TR analysis. Both the rise and the decay time have bad resolution at low energy, so the fit is limited in the [1.5,6] MeV range, where these parameters perform better.

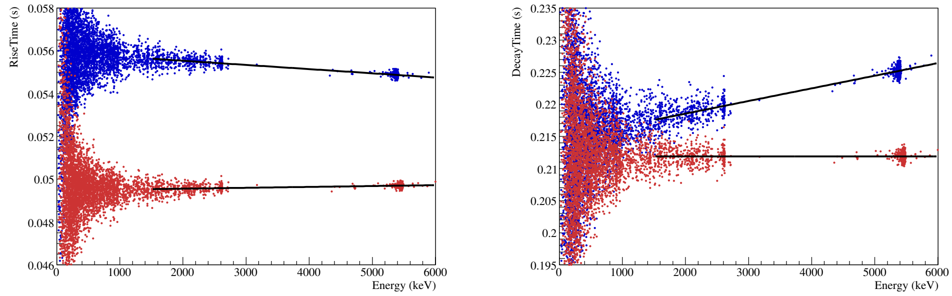

(a) rise time (b) decay time

Figure 4.2. Rise time (left) and decay time (right) vs energy in STD (blue) and TR (red) analyses, MonteCarlo of channel 4.

In figure 4.3 the amplitude vs baseline drift is shown for the STD analysis and for the corresponding TR analysis that perfectly corrects the drift. Finally in figure 4.4 the heater amplitude distribution is compared and fitted for both analyses.

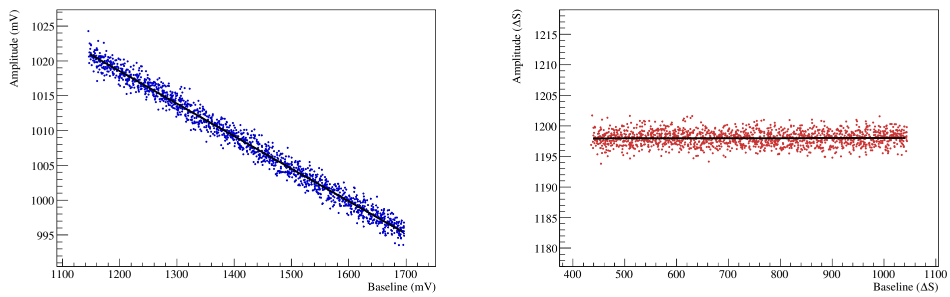

Figure 4.3. Correlation between heater amplitude and baseline in the non-stabilized STD (blue) and TR (red) analyses, Montecarlo of channel 4.

From the obtained results for all channels summarized in table 4.1 we can see that the TR analysis works well: it removes the decay time slope and the heater drift, and it mantains the same resolution. The rise time slope is not completely corrected, this effect is due to the error made by the derivative algorithm (4.3) and is discussed in section 4.6.1.

As probably noticed we did not remove the Bessel filter in the deconvolution path. This step should have been done on the voltage signal before the $\Delta\theta_i$ evaluation with equation (4.2). However it comes out that TR data have the expected features and hence we deduce that the Bessel filter somewhat *commutes* with equation (4.2). This is good because the FFT-deconvolution is a really difficult job with the risk of adding new noise in the output (not just amplifying the already present noise that would be canceled by the optimum filter). The net result of skipping this step is that our $\Delta\theta(t)$, and so $\Delta S(t)$, is the real $\Delta\theta(t)$ convoluted with the Bessel. This is a good feature because we do like the high-frequency noise removal that was originally

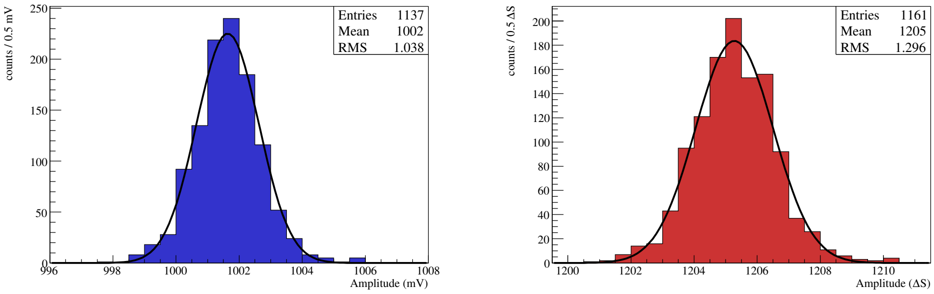

Figure 4.4. Heater resolution in STD (blue) and TR (red) analyses, Montecarlo of channel 4.

Table 4.1. TR analysis compared to the STD analysis on the MonteCarlo of all channels.

Algo	Rise Slope %/MeV	Decay Slope %/MeV	Heater Res. (%)	Heater Slope
		channel 1		
STD	-0.103 ± 0.012	0.539 ± 0.033	0.1402 ± 0.0035	-0.02563 ± 0.00018
TR	0.0031 ± 0.0089	-0.033 ± 0.030	0.1405 ± 0.0035	0.00024 ± 0.00018
		channel 2		
STD	-0.217 ± 0.010	0.550 ± 0.020	0.1534 ± 0.0037	-0.02524 ± 0.00014
TR	0.040 ± 0.011	0.013 ± 0.020	0.1550 ± 0.0045	0.00022 ± 0.00017
		channel 3		
STD	-0.6780 ± 0.0031	1.4675 ± 0.0062	0.1015 ± 0.0022	-0.05628 ± 0.00017
TR	0.1421 ± 0.0029	0.0087 ± 0.0051	0.1062 ± 0.0024	0.00041 ± 0.00018
		channel 4		
STD	-0.3634 ± 0.0049	0.9606 ± 0.0084	0.0991 ± 0.0024	-0.04671 ± 0.00015
TR	0.0841 ± 0.0045	0.0028 ± 0.0072	0.1026 ± 0.0025	0.00009 ± 0.00017
		channel 5		
STD	-0.4097 ± 0.0060	0.936 ± 0.016	0.1203 ± 0.0031	-0.05711 ± 0.00024
TR	0.0215 ± 0.0058	-0.019 ± 0.014	0.1233 ± 0.0032	0.00056 ± 0.00025
		channel 6		
STD	-0.4287 ± 0.0046	0.9790 ± 0.0092	0.0775 ± 0.0019	-0.04351 ± 0.00013
TR	0.0637 ± 0.0059	-0.0058 ± 0.0087	0.0807 ± 0.0020	-0.00016 ± 0.00014
		channel 7		
STD	-0.6639 ± 0.0037	0.9244 ± 0.0065	0.0895 ± 0.0021	-0.03137 ± 0.00014
TR	0.1090 ± 0.0039	-0.0284 ± 0.0057	0.0908 ± 0.0020	0.00050 ± 0.00017

present in the raw data.

4.4 Data analysis

If the model and the hypothesis that ΔT is constant are correct, we expect to obtain on data the same results we obtained on the MonteCarlo. The same quantities checked on the MonteCarlo are being checked on data except for the intrinsic resolution that cannot be checked because the amplitude drift is unavoidably present in real data. Together with the check of heater quantities we will also check the resolution and the drift of two energy lines: the 2615 keV γ line, because it is close to the 0νDBD region, and the 5.4 MeV α line, because of its high statistics and because, being more energetic, it is more sensitive to residual non-linearities. Being this line generated by an α particle, it might be that its pulse shape is slightly different from the rest of the spectrum that is generated by electromagnetic particles: the different shape of α's could be due to the different kind of interaction. Nevertheless it is still not demonstrated [59] that CUORE bolometers are sensitive to this and we will not investigate further this topic here. Another topic we have to take into account in the analysis of real data is the calibration function, that for the MonteCarlo studies done so far was assumed linear (without loss of generality): the data calibration issue is described in detail in the next section. The analyzed measurement was the first calibration measurement of the CCVR detector (run 5), lasted about 2.8 days.

In figure 4.5 the shape parameters of channel 4 are compared for the STD and the TR analysis, and the results on all channels are collected in table 4.2: the decay time is well corrected, showing a residual slope less than 0.2% on all channels except for channel 7, were the correction is less efficient. The rise time slope is instead overshot in the opposite direction, becoming positive: this bias is present on all channels and it could be due either to errors on the parameters entering the model or to some failure of the model itself, or to some bias in the algorithm (see later).

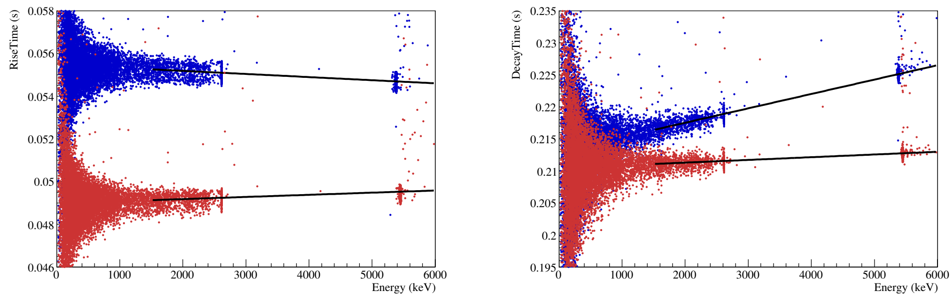

(a) rise time (b) decay time

Figure 4.5. Shape parameters vs energy for the STD (blue) and the TR (red) analysis, data of channel 4.

Concerning the amplitude vs baseline drift, (see channel 4 in figure 4.6 and all channels in tables 4.3, 4.4) the standard analysis perfectly corrects the heater drift with the stabilization algorithm, meaning that all the heater slopes are compatible

Table 4.2. Shape parameters dependence on energy, data of all channels.

ch	Rise Time Slope		Decay Time Slope	
	STD (%/MeV)	TR (%/MeV)	STD (%/MeV)	TR (%/MeV)
1	-0.0374 ± 0.0077	0.0942 ± 0.0062	0.764 ± 0.021	0.197 ± 0.019
2	-0.0445 ± 0.0051	0.1415 ± 0.0071	0.665 ± 0.016	0.115 ± 0.014
3	-0.3791 ± 0.0045	0.2711 ± 0.0074	1.5093 ± 0.0057	0.1516 ± 0.0026
4	-0.2606 ± 0.0070	0.1989 ± 0.0058	1.0478 ± 0.0088	0.1978 ± 0.0044
5	-0.2478 ± 0.0046	0.2306 ± 0.0077	1.005 ± 0.013	0.078 ± 0.011
6	-0.1051 ± 0.0047	0.3330 ± 0.0067	1.0772 ± 0.0064	0.1192 ± 0.0050
7	-0.3231 ± 0.0042	0.1203 ± 0.0046	1.1862 ± 0.0041	0.6941 ± 0.0046

with zero: the STD analysis slope must be zero by definition, because we are fitting with a line a distribution that was already corrected with a line. The heater drift is always different from zero in the TR analysis but as can be seen from the plot of channel 4 the correction is very good. Looking at the slope of the 5.4 MeV (see figure 4.7) we get the real comparison between STD and TR analysis on the drift of particles events: both of them do not perfectly correct the drift but the residual slope is contained in the resolution and hence not relevant. The drift of the STD analysis can be accounted to the fact that the stabilization is made with heater pulses that do not have the same shape of particles, and hence the amplitude estimation of heater pulses is biased.

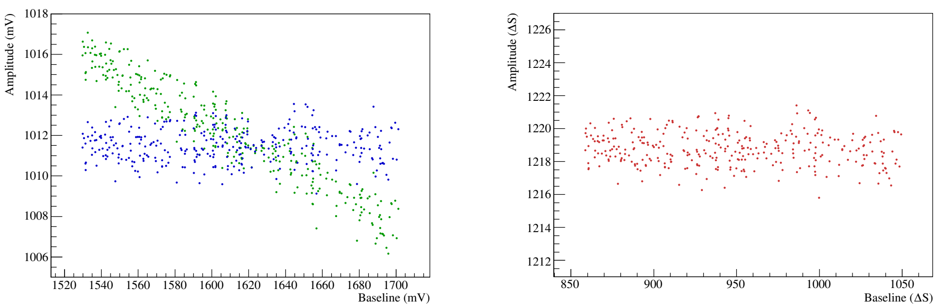

(a) (b)

Figure 4.6. Correlation between heater amplitude and baseline in the STD analysis before (green) and after (blue) the stabilization, and in the TR (red) analysis, data of channel 4.

A more synthetic quantity to estimate the goodness of the correction is the resolution of the peaks: if it is better or equal than the STD analysis it means that the residual drift is negligible otherwise there is an error. Resolutions of heater lines (figure 4.8), 2615 keV lines (figure 4.9) and 5.4 MeV lines (figure 4.10) are reported in tables (4.5, 4.6): the 2615 keV line is not sensitive to the residual slope (and this is good because it is close to our range of interest), the 5.4 MeV line reveals instead some residual slope, channel 7 for example is remarkably worse than other channels

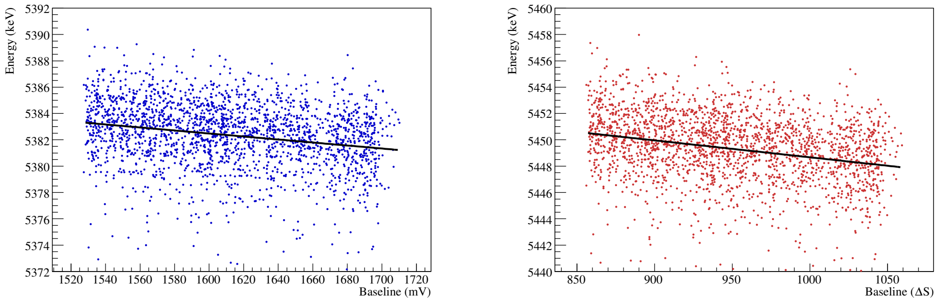

Figure 4.7. Correlation between amplitude and baseline of 5.4 MeV pulses in the STD (blue) and TR (red) analyses, data of channel 4.

Table 4.3. Heater slopes, data of all channels

ch	STD no stab	STD (1/mV)	TR
1	-0.02438 ± 0.00077	0.0021 ± 0.0057	0.00186 ± 0.00075
2	-0.02522 ± 0.00095	0.0000 ± 0.0076	0.00056 ± 0.00098
3	-0.0585 ± 0.0011	0.0000 ± 0.0049	-0.0003 ± 0.0012
4	-0.04944 ± 0.00094	0.0000 ± 0.0046	-0.0017 ± 0.0010
5	-0.0575 ± 0.0015	-0.0005 ± 0.0055	0.0013 ± 0.0015
6	-0.04131 ± 0.00056	0.0000 ± 0.0027	0.00281 ± 0.00061
7	-0.03723 ± 0.00087	0.0001 ± 0.0042	-0.0048 ± 0.0010

Table 4.4. 5.4 MeV slopes, data of all channels

ch	5.4 MeV Slope	
	STD (keV/mV)	TR (keV)
1	-0.0082 ± 0.0013	0.0082 ± 0.0015
2	-0.0083 ± 0.0017	0.0010 ± 0.0019
3	-0.0163 ± 0.0010	-0.00611 ± 0.00079
4	-0.01021 ± 0.00094	-0.01184 ± 0.00087
5	-0.0142 ± 0.0014	-0.0039 ± 0.0013
6	-0.01087 ± 0.00049	0.00784 ± 0.00054
7	-0.01275 ± 0.00068	-0.03164 ± 0.00087

that are compatible with the STD analysis. As channel 7 performed bad also in the decay time correction, we suspect that some input parameter of the model is wrong. Reminding that the TR algorithm has no free parameters, it is important to understand what is the effect generated by the error on the input parameters: this important issue is discussed in section 4.6.

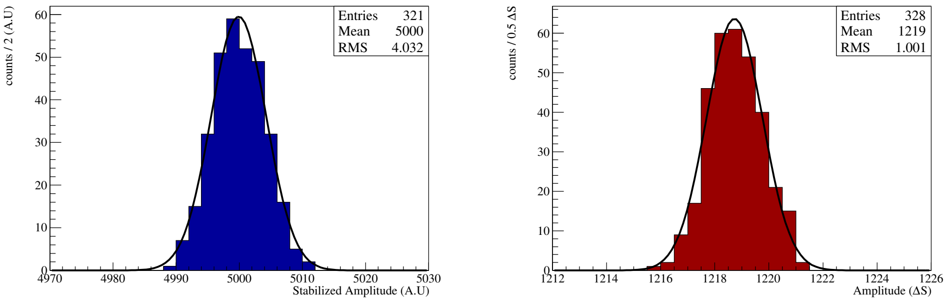

Figure 4.8. Heater amplitude distribution of the STD (blue) and the TR (red) analysis, data of channel 4.

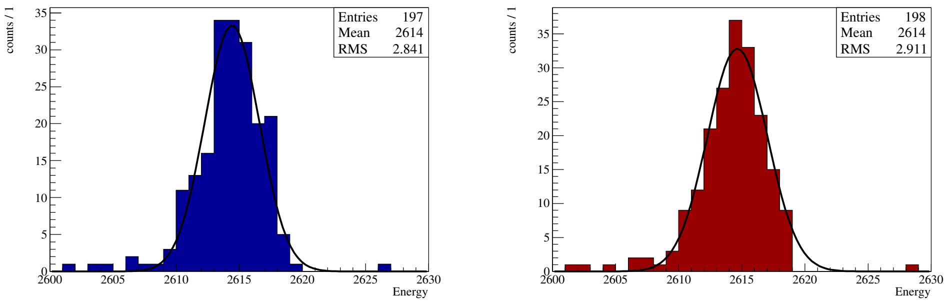

Figure 4.9. 2615 keV line of the STD (blue) and the TR (red) analysis, data of channel 4.

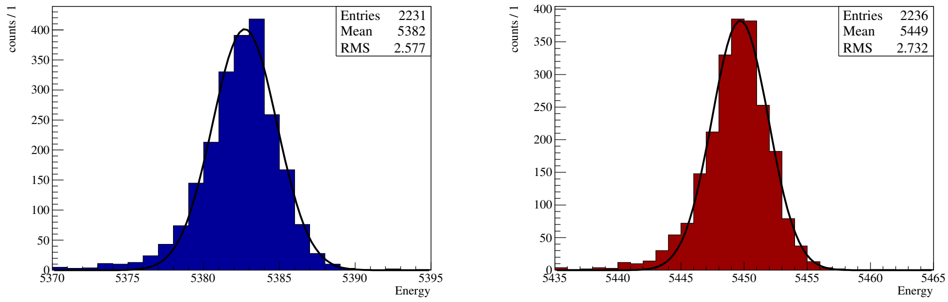

Figure 4.10. 5407 keV line of the STD (blue) and the TR (red) analysis, data of channel 4.

Table 4.5. Heater resolutions comparison, data of all channels.

ch	Heater Resolution STD ‰	Heater Resolution TR ‰
1	1.289 ± 0.067	1.319 ± 0.065
2	1.355 ± 0.073	1.279 ± 0.070
3	0.756 ± 0.031	0.815 ± 0.038
4	0.841 ± 0.039	0.822 ± 0.034
5	1.009 ± 0.046	0.993 ± 0.045
6	0.607 ± 0.032	0.657 ± 0.036
7	0.712 ± 0.032	0.767 ± 0.034

Table 4.6. Particle resolutions comparison, data of all channels.

ch	2.615 keV Resolution		5.4 MeV Resolution	
	STD (keV)	TR (keV)	STD ‰	TR ‰
1	3.05 ± 0.29	3.07 ± 0.24	0.580 ± 0.014	0.601 ± 0.014
2	3.35 ± 0.23	3.50 ± 0.26	0.581 ± 0.013	0.590 ± 0.014
3	1.98 ± 0.14	1.92 ± 0.13	0.4238 ± 0.0069	0.3971 ± 0.0067
4	2.17 ± 0.13	2.38 ± 0.18	0.4112 ± 0.0073	0.4329 ± 0.0079
5	2.55 ± 0.16	2.52 ± 0.17	0.517 ± 0.014	0.482 ± 0.011
6	1.64 ± 0.10	1.654 ± 0.099	0.3096 ± 0.0062	0.2941 ± 0.0052
7	1.747 ± 0.094	1.643 ± 0.079	0.3054 ± 0.0061	0.3947 ± 0.0070

4.4.1 Calibration

After the amplitude evaluation and, only in the STD analysis case, after the stabilization, the amplitude spectrum is calibrated. The evaluation of the coefficients of the calibration function is performed with the most prominent peaks generated by the Thorium source. In figure 4.11 the spectrum obtained with the two analyses is shown, indicating the nominal energy (in keV) of the used peaks.

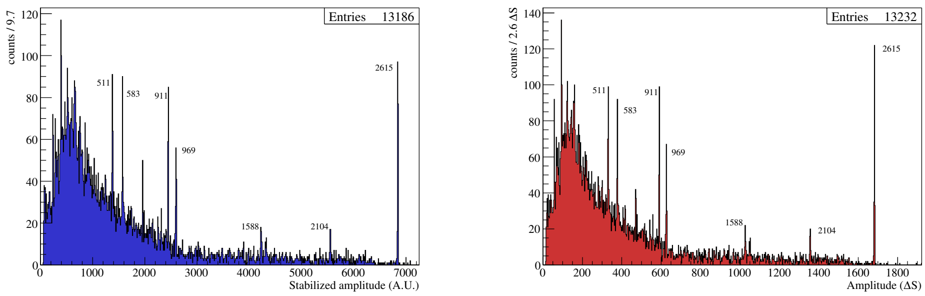

(a) STD analysis (b) TR analysis

Figure 4.11. Amplitude spectrum before calibration, the peaks of the Thorium source used for the evaluation of the calibration function are tagged with their nominal energy (in keV).

The calibration function used to calibrate the amplitude x in the STD analysis is:

$$E = e^{c_1}\, x^{c_2 + c_3 \log(x)} \ . \tag{4.7}$$

For the TR analysis we use instead a second order polynomial

$$E = a\,x + b\,x^2 \tag{4.8}$$

because we expect small deviations from linearity. The calibration routine looks for the peaks in the spectrum, fits their positions x_i with the expected p.d.f. for each peak (gaussian or gaussian + different types of background), and finally evaluate the calibration function coefficients from the E (nominal) vs x plot. The fit residuals of channel 4 are shown in figure 4.12 and the fitted parameters with the χ^2/ndf of each channel are reported in tables (4.7,4.8): the TR analysis performs better than the STD one as the chi-squares are lower.

The 5407 keV α line is not included in the estimation of the coefficients and is very far from the last calibration point (2615 keV), hence it is a good line to check how close is the calibration function to the ideal calibration function. From the summed energy spectrum over all channels (see figure 4.13) we see that the TR analysis is much more consistent among channels than the STD analysis. However the peak is shifted of about 40 keV; this shift could be either due to an error of the calibration function or to an intrinsic alpha quenching. At this level it is impossible to distinguish between the two effects.

The last comparison we performed is the deviation from linearity of the calibrations of the two analysis. The chi-squares of the simple fit $E = c\,x$ are reported in table 4.9, where we see that the TR analysis is much closer to linearity than the STD one, but it cannot be assumed linear yet.

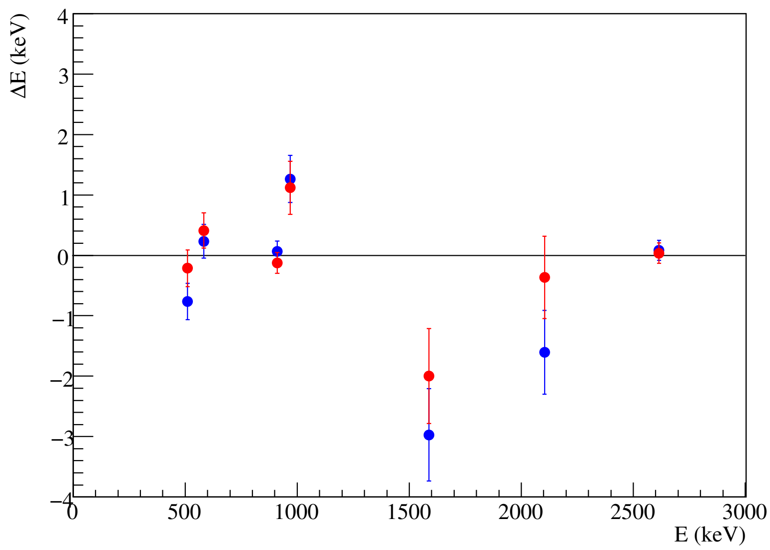

Figure 4.12. Residuals of the calibration function of the STD (blue) and the TR (red) analysis.

Table 4.7. Coefficients of the STD analysis calibration function, $E = e^{c_1}\,x^{c_2+c_3\log(x)}$.

ch	c_0	c_1	c_3	χ^2/ndf
1	-0.4634 ± 0.0088	0.8944 ± 0.0020	0.00712 ± 0.00012	2.0
2	-0.715 ± 0.041	0.9301 ± 0.0099	0.00495 ± 0.00060	3.2
3	-0.3919 ± 0.0059	0.7711 ± 0.0014	0.015733 ± 0.000080	22
4	-0.4669 ± 0.0068	0.8522 ± 0.0016	0.010380 ± 0.000091	9.7
5	-0.4232 ± 0.0078	0.8724 ± 0.0018	0.00923 ± 0.00011	8.9
6	-0.6192 ± 0.0046	0.8515 ± 0.0011	0.010370 ± 0.000065	18
7	-0.7428 ± 0.0047	0.8301 ± 0.0011	0.011466 ± 0.000063	22

Table 4.8. Coefficients of the TR analysis calibration function, $E = a\,x + b\,x^2$.

ch	a (keV)	b (10^{-6} keV)	χ^2/ndf
1	3.7296 ± 0.0012	12.9 ± 1.8	1.7
2	3.22396 ± 0.00092	11.3 ± 1.3	0.94
3	1.00517 ± 0.00018	6.882 ± 0.076	3.3
4	1.53999 ± 0.00036	8.41 ± 0.23	3.3
5	1.57197 ± 0.00038	4.87 ± 0.25	2.8
6	1.51001 ± 0.00022	8.44 ± 0.14	2.7
7	1.24302 ± 0.00017	11.237 ± 0.093	4.0

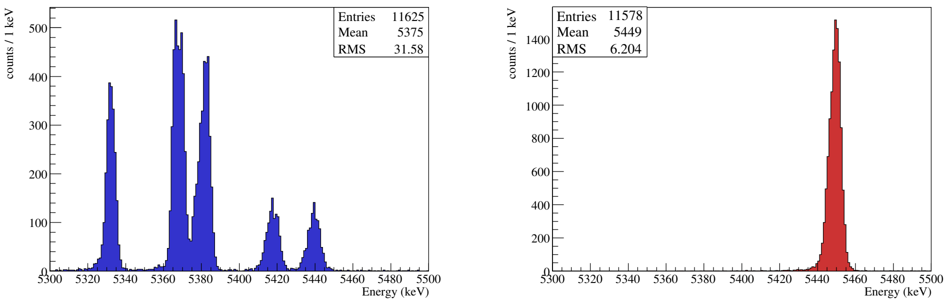

(a) STD (b) TR

Figure 4.13. 5407 keV lines summed over all channels.

Table 4.9. χ^2/ndf of the linear calibration function $E = c\,x$ on all channels.

Channel	1	2	3	4	5	6	7
STD	256	464	10381	2186	1996	8372	9806
TR	15	14	1150	105	54	417	1597

4.5 Residual drift in time

Since the time the detector is calibrated, background data begins to be acquired for long time (one or more months). During this time the baseline moves and if the drift is too high there is the risk that the resolution gets worse; moreover if the drift is not symmetric the peaks could significantly loose the position they had at the calibration time. Due to some difficulties in the cryostat stabilization, the baseline drifted considerably during the first weeks of the CCVR data taking. This is not good in general but give us the opportunity to check the residual amplitude drift.

Plotting the position of the 5.4 MeV line against the baseline of each single run we can have an idea of what is the magnitude of the residual drift; from figure 4.14 we see that after the calibration run (5), the peak position drifts in the TR analysis, while in the STD analysis it is stable. We have seen before that also in the STD analysis there is a residual drift inside a run, nevertheless, since the stabilization procedure is applied to each single run, the average position is taken back every run to the same value: instead of a single drift there is something like a sawtooth shape. In table 4.10 the 5.4 MeV peak positions of the calibration run are compared with the average positions over the four subsequent background runs: it turns out that in the TR analysis the drift is more evident.

At some point between run 9 and run 10 something uncontrolled happened to the baselines, as shown in figure 4.15 the baseline jump is evident between the end of run 9 and the beginning of run 10. It is not clear if what happened was due to the cryogenics or to the electronics. Looking at the residual drift for both analyses (shown in figure 4.16), we see that the TR analysis was much more *resistant* to this event; after run 11 the heater was disconnected so the STD analysis with the heater

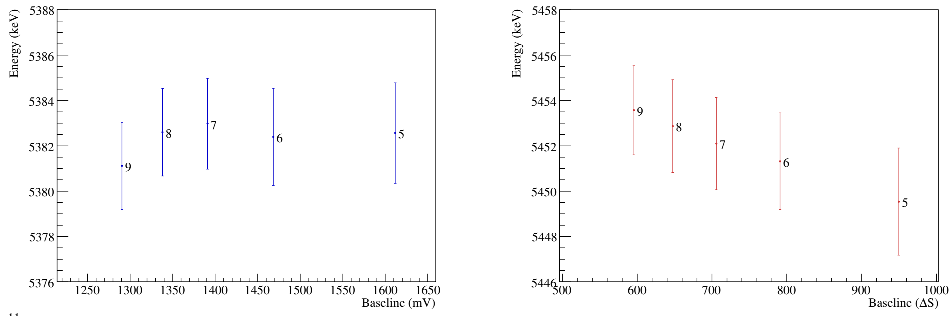

(a) STD analysis (b) TR analysis

Figure 4.14. Position of the 5.4 MeV line over runs, error bars corresponds to the resolution of the peak, channel 4.

Table 4.10. Position of the 5.4 MeV line in the calibration run (5) and in the four background runs after.

ch	STD		TR	
	Run 5	Runs 6,7,8,9	Run 5	Runs 6,7,8,9
1	5439.4	5438.8	5450.5	5445.7
2	5417.5	5417.0	5449.6	5451.2
3	5332.1	5334.6	5446.8	5447.7
4	5382.6	5382.6	5449.5	5452.5
5	5378.4	5378.8	5445.9	5447.1
6	5369.7	5371.5	5450.5	5445.9
7	5366.1	5367.8	5451.1	5456.3

could not be performed anymore. In table 4.11 the average positions of the 5.4 MeV peak are compared for the two runs before and after the baseline jump, the TR analysis performs better on all channels and the peak shift is comparable with the the residual drift seen in normal conditions.
Looking at the plot in figure 4.17, the heater energy after run 9 increased of about 0.2%, probably because of a grounding problem of the electronics. An instability of the heater energy worsen the resolution and the calibration in the STD analysis, as the amplitude spectrum is scaled by a non constant factor. This is the cause of the 5.4 MeV peak shift in the STD analysis. The TR analysis instead was not affected by this heater shift because it was not used to stabilize the data.
After this event the CCVR run went on because of the presence of the 5.4 MeV line that can be used to stabilize in place of the heater. With bolometers without the ^{210}Po contamination (like CUORE bolometers), if the heater position changes, a re-calibration of the detector is necessary with the STD analysis, while it seems not necessary with the TR analysis.

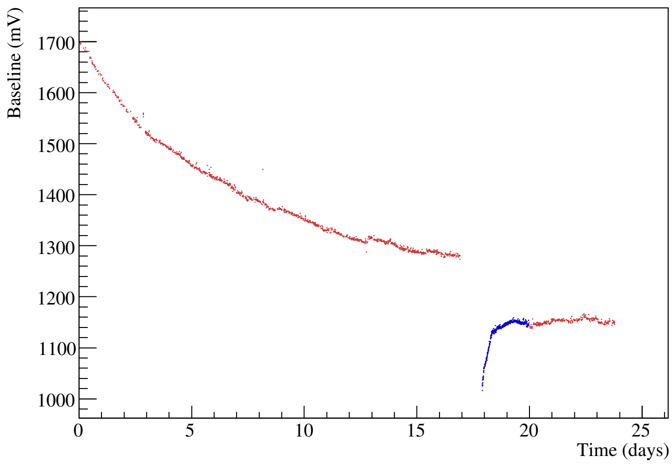

Figure 4.15. Baseline vs time of channel 4, the jump between run 9 and run 10 (in blue) is evident.

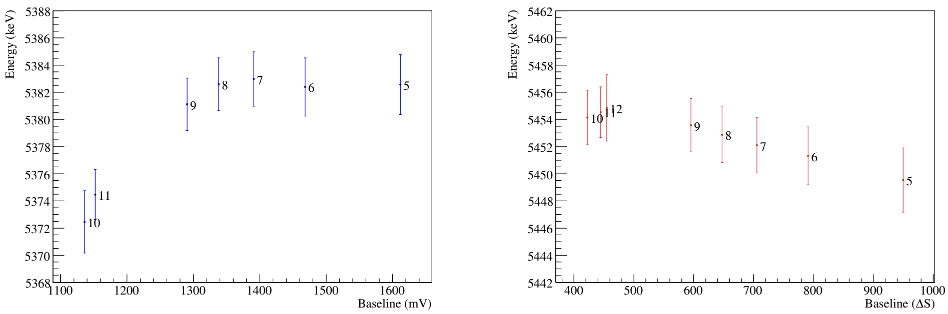

(a) STD analysis

(b) TR analysis

Figure 4.16. Residual drift up to run 12.

Table 4.11. Positions of the 5.4 MeV line before and after run 10.

ch	STD		TR	
	Runs 8,9	Runs 10,11	Runs 8,9	Runs 10,11
1	5438.9	5428.3	5444.8	5441.5
2	5417.2	5406.3	5452.0	5450.5
3	5334.6	5328.1	5447.9	5447.7
4	5381.7	5374.0	5453.2	5454.4
5	5378.0	5370.5	5447.4	5445.0
6	5372.0	5362.5	5444.9	5441.6
7	5368.0	5358.3	5457.7	5460.0

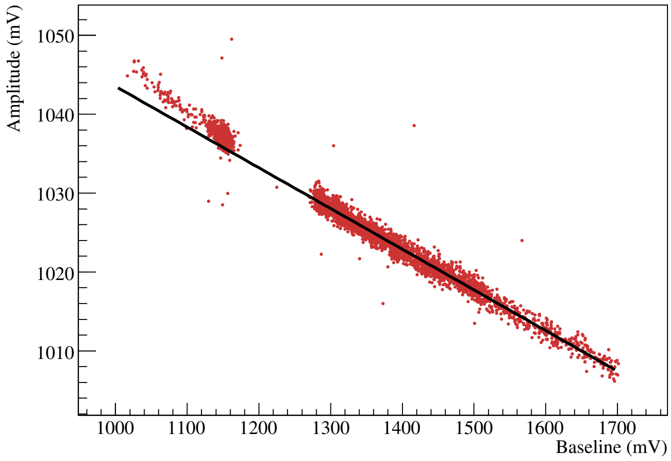

Figure 4.17. Non-stabilized heater amplitude in the STD analysis. The baseline jump from 1280 to 1150 mV is accompanied by a shift of the heater amplitude. This shift is not fully compatible with a temperature variation, as the data do not lie on the same line.

4.6 Sources of systematic errors

The TR analysis and the underlying model are very close to remove all the unwanted non-regularities of the response function. We have seen that there is some residual drift in the shape parameters and in the amplitude vs baseline relationship. In this section we will investigate how the uncertainty on the parameters used in the TR analysis affects the resulting response function. The quantities entering equation (4.2) are ρ, V_B, G, R_L, c_p, and the derivative algorithm used to estimate $\Delta V'$ from the sampled ΔV signal. We will first analyze the effect of the derivative algorithm and finally the effect generated by the uncertainty on the biasing circuit and read-out circuit parameters. The analyses have been performed on MonteCarlo data checking rise time, decay time, heater slope and heater resolution (see section 4.3).

4.6.1 Choice of the derivative algorithm

There are many numerical methods in literature [60] to compute the derivative of a discrete function. The simpler algorithms are the 2-point Eulero's formulas:

$$V_i' = \frac{V_i - V_{i-1}}{\Delta t} \qquad \epsilon = \frac{\Delta t}{2} V_i'' \qquad [2P] \tag{4.9a}$$

$$V_i' = \frac{V_{i+1} - V_i}{\Delta t} \qquad \epsilon = -\frac{\Delta t}{2} V_i'' \qquad [2PF] \tag{4.9b}$$

where Δt is the sampling interval and ϵ is the error of the approximation. The error can be reduced using formulas with more points, the class of 3-point formulas is:

$$V_i' = \frac{-3V_i + 4V_{i+1} - V_{i+2}}{2\Delta t} \qquad \epsilon = \frac{\Delta t^2}{3} V_i''' \qquad [3PF] \qquad (4.10a)$$

$$V_i' = \frac{V_{i+1} - V_{i-1}}{2\Delta t} \qquad \epsilon = -\frac{\Delta t^2}{6} V_i''' \qquad [3P] \qquad (4.10b)$$

$$V_i' = \frac{3V_i - 4V_{i-1} + V_{i-2}}{2\Delta t} \qquad \epsilon = \frac{\Delta t^2}{3} V_i''' \qquad [3PB] \qquad (4.10c)$$

When dealing with the limits of the acquisition window some equation cannot be used and the other equations in the set are used: if for example the data are processed with the symmetric algorithm (4.10b), the first and the last point are processed with 4.10a and 4.10c respectively. The last formulas we will test are the 5 points formulas:

$$V_i' = \frac{-25V_i + 48V_{i+1} - 36V_{i+2} + 16V_{i+3} - 3V_{i+4}}{12\Delta t} \qquad \epsilon = \frac{\Delta t^4}{5} V_i^V \qquad [5PF] \qquad (4.11a)$$

$$V_i' = \frac{-3V_{i-1} - 10V_i + 18V_{i+1} - 6V_{i+2} + V_{i+3}}{12\Delta t} \qquad \epsilon = -\frac{\Delta t^4}{20} V_i^V \qquad (4.11b)$$

$$V_i' = \frac{V_{i-2} - 8V_{i-1} + 8V_{i+1} - V_{i+2}}{12\Delta t} \qquad \epsilon = \frac{\Delta t^4}{30} V_i^V \qquad [5P] \qquad (4.11c)$$

$$V_i' = \frac{3V_{i+1} + 10V_i - 18V_{i-1} + 6V_{i-2} - V_{i-3}}{12\Delta t} \qquad \epsilon = -\frac{\Delta t^4}{20} V_i^V \qquad (4.11d)$$

$$V_i' = \frac{25V_i - 48V_{i-1} + 36V_{i-2} - 16V_{i-3} + 3V_{i-4}}{12\Delta t} \qquad \epsilon = \frac{\Delta t^4}{5} V_i^V \qquad [5PB] \qquad (4.11e)$$

In principle best algorithms are those with more points, however one has to deal also with the stability of the algorithm that is something depending on the data being analyzed and not predictable a priori; it is known that algorithms with more points work better when the function is smooth but experience problems when the function is stiff. As our data have both fast (rise time) and slow (decay time) features and there is also the presence of the noise, it is hard to define whether we are dealing with a stiff or a smooth function, hence we will test each algorithm on the MonteCarlo. From the results reported in table A.1 it turns out that the algorithms performing better are 2P, 3P and 5P; forward algorithms are instead the worst ones and so we did not try the 5PF. The choice between 2P, 3P, and 5P is not simple because none of them stands out with respect to others: 2P is the best in the correction of the rise time and the worst in the correction of the decay time, 3P is slightly better in the rise time correction than 5P, that instead is slightly better in the decay time correction. The resolution is slightly worst with respect to the standard analysis but not relevant in all cases, and the residual drift of the heater is slightly better in 3P and 5P than in 2P. It turns out that the number of bolometers is too small or the model is not sensitive to the difference between these algorithms to decide which one is better. We chose the 3P algorithm, keeping in mind that also the 2P and 5P algorithms should be revisited with future detectors.

4.6.2 Error on the biasing and read-out circuits parameters

To put in evidence the dependence of the TR algorithm on the biasing and read-out circuits parameters we take the approximated expression of equation (3.16):

$$\Delta V(t) + [1 + \Delta\theta(t)] \frac{R_L c_p \rho}{1+\rho} \frac{\Delta V(t)}{dt} = \frac{\rho V_B G}{1+\rho} \Delta\theta(t) \ . \tag{4.12}$$

As shown in section 2.5.1 the estimation of R_S and hence of ρ (see equation 3.15) is made measuring the amplified thermistor voltage $V^G_{R_S} = V_{R_S} G_S$. Substituting the measured quantity

$$\frac{\rho}{1+\rho} = \frac{V^G_{R_S}}{2 V_B G_S} \tag{4.13}$$

we obtain:

$$\underbrace{\frac{2G_S}{G V^G_{R_S}}}_{1/m_1} \Delta V(t) + [1 + \Delta\theta(t)] \underbrace{\frac{R_L c_p}{V_B G}}_{m_2} \frac{\Delta V(t)}{dt} = \Delta\theta(t) \, . \tag{4.14}$$

We see that the there are two independent quantities that are possible source of errors, the multiplication factor of ΔV, $(1/m_1)$, and the multiplication factor of $\Delta V'$, (m_2). Varying these two parameters in the TR analysis of MonteCarlo data we can estimate the effect on the usual quantities: rise time slope, decay time slope, heater slope and heater resolution . The expected error is about 10% for $1/m_1$, due to the error on the gains, and about 20% for m_2, dominated by the error on the load resistances. From the results reported in tables (A.2,A.3) we see that the residual drift of the amplitude we have seen on data is compatible with the drifts generated by the uncertainties on m_1 and m_2, the residual drift on the rise time instead cannot be explained. Concerning the residual drift on the decay time it cannot be fully explained, however being the correction somehow very effective with respect to the STD analysis it is not the main problem in this phase.

The needed precision on the parameters should be at percent level on m_1 and below 10% on m_2.

Chapter 5

Thermal response analysis on the Three Towers detector

The bolometer model we have developed is able to describe the main features of the response function of CUORE bolometers. The TR algorithm, based only on measurable parameters, proved to be a powerful tool to remove the unwanted non-regularities of the response function, but still it is not perfect. The rise time behavior is not fully understood as well as there is a small residual correlation between amplitude and baseline, compatible with the uncertainty on the parameters entering the model. Without this residual drift the proposed analysis could be competitive with the standard analysis that suffers from heater instabilities. Moreover, being the pulse shape less dependent on energy, the pulse shape discrimination, a topic we will not cover, becomes simpler. The correctness of the model is also enhanced by the fact that the TR data are closer to a linear calibration than the raw data.
The residual drift could be removed changing by hand the model parameters, however we prefer to examine the model deeper and measure these parameters on the detector. These measurements were not performed for the CCVR run and the nominal values of gains, bias voltages and load resistors were used. In this chapter the model will be validated on the Three Towers detector, where the parameters have been measured with the required accuracy.

5.1 The Three Towers detector

This detector has been built to test three different cleaning techniques of the copper holding the crystals, and select the best in terms of α's contamination. Each tower contains 12 crystals, some of them equipped with two thermistors. A few thermistors and heaters is broken so that some crystal is not readable at all and about half of them does not have the heater. Since the used crystals do not have the ^{210}Po contamination, when the heater is not present there is no way to stabilize the data. To overcome this problem a permanent ^{40}K source has been faced to the detector, and the photopeak of its 1461 keV γ line has been used to stabilize the data. Heaters and thermistors could have been repaired before the cooling down, however the earthquake in L'Aquila [61] caused big delays to the assembly of this detector. Given that the number of alive crystals is sufficient to compare the copper contamination of the towers, and given that the stabilization is preformed with the ^{40}K, the lost channels were not repaired. The Three Towers detector started the data taking the 4th of September 2009.

The current configuration is listed in table B.1, where it can be seen that the number of thermistors is 39. A subset of channels (16) is plugged to the "cold electronics" (see section 2.6). The main difference with the warm electronics, the one used in CCVR, is that pre-amplifiers and load resistances are inside the cryostat, at about 110 K. It was set-up in the past to check if the noise coming from load resistors and pre-amplifiers affected the bolometers, nevertheless it was found that the resolution in the 0νDBD region did not improve. CUORE will not use cold electronics, however in the Three Towers we were forced to use it since in the hall A cryostat the availability of warm channels is limited.

5.2 Measurements of model parameters

The MonteCarlo studies (see section 4.6.2) showed that the error on the model parameters should be at percent level on $V_{R_S}^G, G$ and G_S, and less than 10% on R_L, c_p and V_B. Rewriting the $\Delta\theta$ expression (4.2) in terms of these parameters:

$$\Delta\theta(t) = -\frac{\frac{V_B G_S}{V_{R_S}^G}\Delta V(t) + R_L c_p \Delta V'(t)}{\frac{G}{G_S}(V_{R_S}^G - V_B G_S) + \Delta V(t) + R_L c_p \Delta V'(t)} \tag{5.1}$$

it turns out that they are not all independent. The independent quantities instead are $V_{R_S}^G$, G/G_S, $R_L c_p$, $V_B G_S$ and their precision should be:

Parameter	Precision needed
$V_{R_S}^G$	$< 2 \div 3\,\%$
G/G_S	$< 2 \div 3\,\%$
$V_B G_S$	$< 10\,\%$
$R_L c_p$	$< 10\,\%$

The amplified thermistor voltage $V_{R_S}^G$ is usually measured with a multimeter, the data instead are acquired with the DAQ. To be unaffected by the intercalibration of the two instruments, $V_{R_S}^G$ should be measured with the DAQ. The nominal gain values provided by the FE board specifications have a precision of order 5%, therefore the ratio G/G_S could have an even higher error. The measurement of this parameter is then necessary. Concerning the parameter $V_B G_S$, the nominal values of bias voltages (V_B) provided by the FE boards specifications have a precision of order 5% that is enough for our purposes. However, even if the precision on the gain is less than 5%, the absolute value of G_S is not only the gain provided by the amplifier of the FE board, but it contains also the gain of the Bessel Filter, the gain of the DAQ, and any possible signal attenuation (like cables couplings, grounding problems, etc...). It is then important to measure also the $V_B G_S$ parameter. The vendor specifications of load resistances (R_L) report a nominal value of 54 GΩ with a precision of order 10%. This value is then at limit, and some resistance could not have the needed precision. The parasitic capacitance (c_p) generated by the wires used to bias and read the thermistor depend on the detector and on the cryostat set-up so they must be measured for each new detector configuration.

In conclusion all the parameters of the model need dedicated measurements. In this section the measurements made on the Three Towers detector will be presented.

5.2.1 Measurement of $V_{R_S}^G$ and V_S

As already stated, the measurements of the working resistances R_S are usually done right after the detector cooling and before the start of the data acquisition to check what is the rough temperature of the detectors. For our purposes the precision of the usual procedure is not enough (or better is undefined). Moreover the baseline value V_S associated to the measured resistance is not recorded, and is needed to compute $\Delta V(t) = V(t) - V_S$ in equation (5.1). To overcome this problem an automated tool to measure the thermistor voltage $V_{R_S}^G$ and V_S of each channel with the data acquisition system has been developed, following the procedure described in section 2.5.1. The measurement is broken down in four steps. For each step five baseline events, each of them lasting five seconds, are acquired with the DAQ. Once the baselines are acquired the system modify the FE parameters for the next step. These steps are (see figure 5.1):

- Step V_S^1 : Offset, gain G, bias voltage V_B and bias polarity are the same of the data acquisition phase.
- Step V^-: The additional offset is removed and the gain is lowered to G_S.
- Step V^+: Same configuration of the step V^- but the polarity is inverted.
- Step V_S^2 : Back to the normal configuration, same conditions of the step V_S^1.

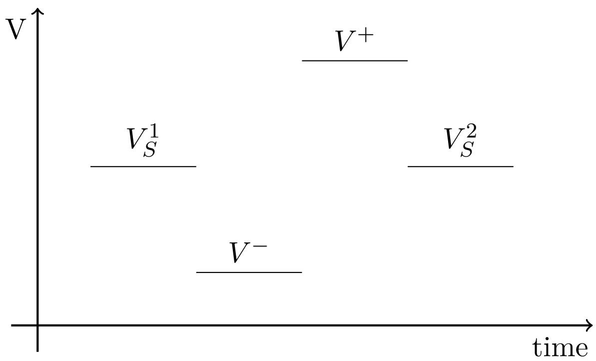

Figure 5.1. The four steps needed to measure the thermistor voltage and the associated baseline.

The baseline events are then averaged to obtain a good estimate of the voltage of each step (V_S^1, V^-, V^+, V_S^2). The thermistor voltage $V_{R_S}^G$ is then obtained as:

$$V_{R_S}^G = \frac{V^+ - V-}{2} \; . \tag{5.2}$$

During the measurement the global temperature of the detector could change. This implies that V^+ and V^- could not refer to the same temperature. Assuming that the drift in temperature is constant in time, the error on $V_{R_S}^G$ can be (over) estimated from the voltage variation between the beginning and the end of the measurement as:

$$\sigma_{V_{R_S}^G} = \left| V_S^1 - V_S^2 \right| \frac{G_S}{G} \, . \tag{5.3}$$

Finally V_S is estimated as the average between V_S^1 and V_S^2:

$$V_S = \frac{V_S^1 + V_S^2}{2} \, . \tag{5.4}$$

Using the measured values of R_L and $V_B \, G_S$ (see sections 5.2.3 and 5.2.4), the thermistor resistance can also be extracted using equation (2.24):

$$R_S = \frac{R_L}{V_B G_S / V_{R_S}^G - 1} \, . \tag{5.5}$$

An example of the baselines acquired with this procedure is shown in figure 5.2. The measured values are listed in table B.2 where it can be seen that $\sigma_{V_{R_S}^G}$ is always less than 0.2%.

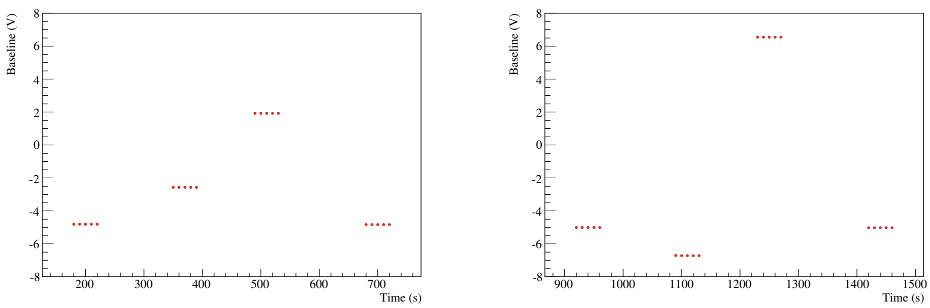

(a) Channel 26 (b) Channel 47

Figure 5.2. Measurement of the thermistor voltage and the associated baseline for a low resistance thermistor (a) and a high resistance one (b). Each dot represents the baseline of the acquired window.

5.2.2 Measurement of G/G_S

The ratio between the gain G used during the data acquisition and the gain G_S used to measure $V_{R_S}^G$ can be estimated by measuring the amplitude of a pulse of fixed energy in these gain configurations. The 1461 keV pulses generated by the ^{40}K source have been used for this purpose. For each channel, about 20 pulse amplitudes have been measured using the gain G and about the same have been measured using the gain G_S. The parameter G/G_S has been simply calculated as:

$$\frac{G}{G_S} = \frac{\text{Amplitude measured with gain } G}{\text{Amplitude measured with gain } G_S} \, . \tag{5.6}$$

The measured values are reported in table B.3, where it can be seen that the error is always smaller than 0.2%. The departure from the nominal value (see table B.1) is shown in figure 5.3, the dispersion is about 0.3% and the average difference is about −0.6%. Given that the needed precision should be less than 2%, one could also use the nominal value in this case.

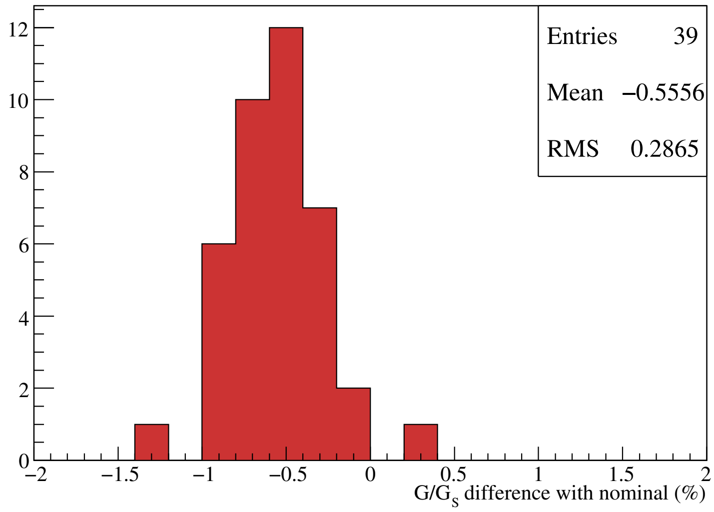

Figure 5.3. Departure of the measured G/G_S parameter from its nominal value, all channels of the Three Towers detector.

5.2.3 Measurement of R_L

Resistances higher than GΩ's cannot be measured with a common multimeter, being too high. The technique consists instead in biasing the resistance with a known voltage V, measuring the current I flowing into it with a pico-ammeter and computing its value using the Ohm's law $R = V/I$. The load resistances have been biased with a DC voltage of 10 V and the current flowing into them has been measured with a Keithley device. Since the current in the circuit is very small, of order 100 pA, the resistances were housed in a grounded metal shield to prevent currents generated by electromagnetic interferences (see figure 5.4).

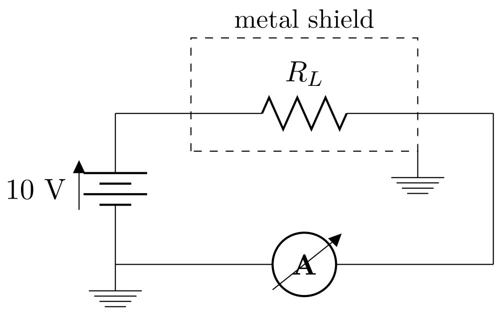

Figure 5.4. Experimental setup of the load resistances measurement.

Unfortunately only warm electronics resistances were measured, because unsoldering the cold electronics resistances could severely damage the rest of the circuit. The systematic error of the measurement, dominated by the environmental setup, has been evaluated to be less than 2%. The measured values are reported in table B.3. The difference with the nominal value (see table B.1) is about zero and the dispersion is about 4% (see figure 5.5)

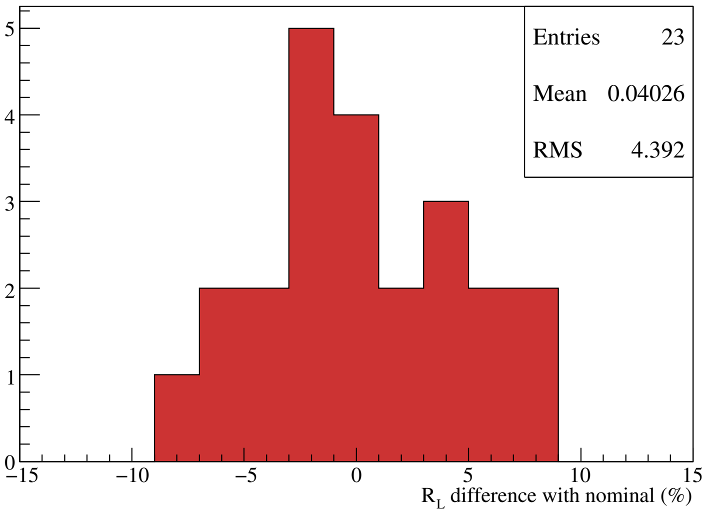

Figure 5.5. Departure of the measured R_L parameter from its nominal value, warm electronics channels of the Three Towers.

5.2.4 Measurement of $V_B G_S$

The FE boards provide the possibility of switching the biasing circuit from the bolometer resistance to a couple of resistances (R_G) shorted to ground.
They are high precision resistances (tolerance less than 0.5%) used to test the boards in the production phase and their value is $R_G = 1.1\,\mathrm{M}\,\Omega$. Biasing them in the same way of the thermistor, the voltage across the resistances can be expressed as:

$$V_{2R_G} = \frac{2R_G}{R_L + 2R_G} V_B G_S \ . \tag{5.7}$$

Measuring it with the same procedure described in section 5.2.1 we can extract the $V_B G_S$ parameter:

$$V_B G_S = V_{2R_G} \frac{R_L + 2R_G}{2R_G} \tag{5.8}$$

where we used the measured value of R_L. The values of $V_B G_S$ are reported in table (B.3), the estimation error is dominated by the systematic error on R_L (about 2%). Unfortunately it is not possible to short to ground the biasing circuit of cold electronics channels, so the measurement was only made with warm electronics. The departure from the nominal value (see table B.1) is shown in figure 5.6, where it can be seen that the dispersion is about 0.6% and the average difference is about −1%, consistent with the systematic error on R_L. Given that the needed precision should be less than 10%, one could also use the nominal value in this case.

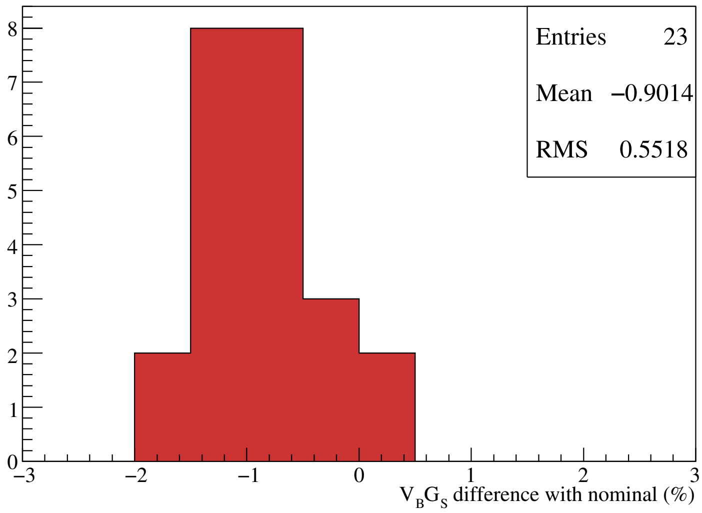

Figure 5.6. Departure of the measured $V_B G_S$ parameter from its nominal value, warm electronics channels of the Three Towers.

5.2.5 Measurement of c_p

For each bolometer the connection to the pre-amplifier contained in the FE board consists of three couples of wires in series (see section 2.5), each with its own capacitance: the wires connecting the bolometer to the socket above the 1-K pot (c_p^k), the wires carrying the signal from the 1-K pot out of the cryostat (c_p^c), and the Fisher cables connecting the cryostat to the FE boards (c_p^f). For cold electronics channels the wire path stops in the middle of the cryostat, where are the pre-amplifiers.

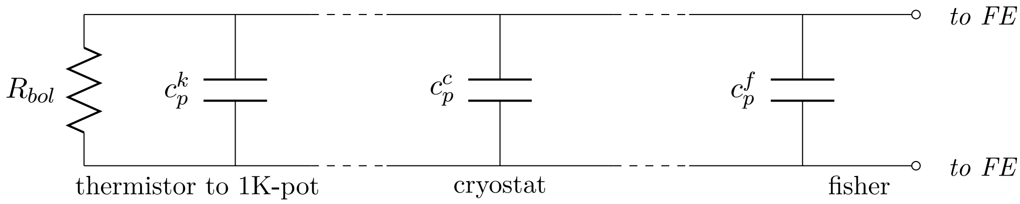

Figure 5.7. Scheme of the wires connecting the bolometer to the Front-End board.

The total capacitance (c_p) is the sum of all these capacitances plus the input capacitance of the FE board (c_p^{FE}):

$$c_p = c_p^t + c_p^c + c_p^f + c_p^{FE} \tag{5.9}$$

The values of c_p^c and c_p^f have been measured for every channel using a capacitance meter with a precision of 2 pF. The c_p^{FE} parameters is available in the FE board specifications, it is the same for each channel and equal to 15 pF.

The c_p^t value, instead, cannot not be measured directly for each channel. The couple of wires connecting the bolometer to the 1-K pot sockets are already connected to the bolometer in the assembly phase and their length is not the same as in the operating phase. When the tower is afterwards hanged to the cryostat, the wires are cut at the correct length before being plugged. Measuring the capacitance is then impossible because they are shorted to the thermistor, that at room temperature has a resistance of few Ohms. Nevertheless the resistance of the series composed by the two wires and by the thermistor is a measurable parameter. As both capacitance and resistance scale with length, it can be assumed that capacitance scales with resistance, then the c_p^t parameter can be extracted from the measurement of the resistance of the bolometer wire at room temperature (R^t). The $c_p^t - R^t$ characterization has been done measuring wires of variable length of the same type of the wires used to assemble detector. The parameters estimated from the linear fit (see figure 5.8):

$$c_p^t = a_c + b_c\,R^t \tag{5.10}$$

are $a_c = -2.2 \pm 0.8\,\mathrm{pF}$ and $b_c = 0.251 \pm 0.003\,\mathrm{pF}/\Omega$. The error on the capacitances estimated with this method has been computed from the residuals of the fit (see figure 5.8) to be approximately 2 pF.

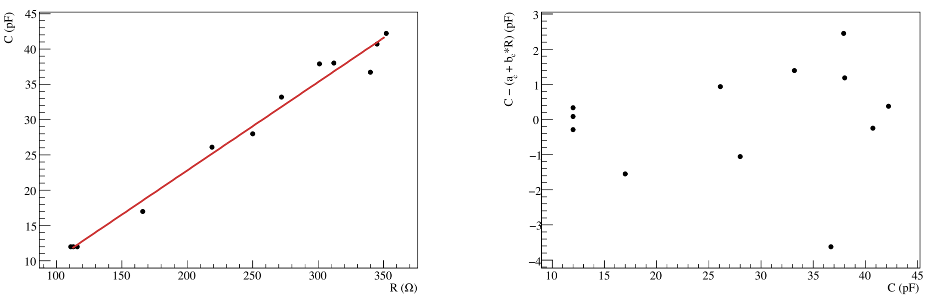

(a) (b)

Figure 5.8. Relationship between the resistance and the capacitance of a bunch of test wires (a). Residuals of the linear fit $C = a_c + b_c\,R$ (b).

The capacitances measured fore each channel are listed in table (B.4) and the average values are summarized in table (5.1) where it can be seen that the obtained precision is about 2% for cold electronics and 1% for warm electronics.

Table 5.1. Average wires capacitance of the Three Towers detector, values are in pF.

electronics	c_p^t	c_p^c	c_p^f	c_p^{FE}	c_p	σ_{c_p}
cold	19	114	0	0	132	3
warm	19	261	80	15	376	4

In conclusion the precision reached on all parameters is much better than what was needed (see table 5.2). For what concern cold electronics, the R_L and $V_B G_S$ parameters could not be measured, so their nominal values will be used.

Table 5.2. Summary of the model parameter measurements.

Parameter	Precision needed	Actual Precision	
$V_{R_S}^G$	$< 2 \div 3\%$	0.2%	
G/G_S	$< 2 \div 3\%\%$	0.2%	
$V_B G_S$	$< 10\%$	2%	(only warm electronics)
R_L	$< 10\%$	2%	(only warm electronics)
c_p	$< 10\%$	$1 \div 2\%$	

5.3 Results on calibration data

In this section the comparison between the STD and the TR analyses made on the Three Towers detector is presented. The comparison of shape parameters, amplitude slope and calibration function is made using the data of the first calibration. The amplitude drift in time is instead evaluated on background data (see next section), as we did for the analysis of the CCVR detector.

The dependence of the pulse rise time on amplitude is shown in figure 5.9, where it can be seen that the TR algorithm reduces the average slope of a factor $\sim 50\%$. The same result is obtained for the decay time, shown in figure 5.10.

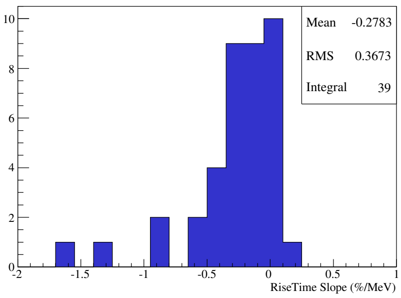

(a) STD analysis

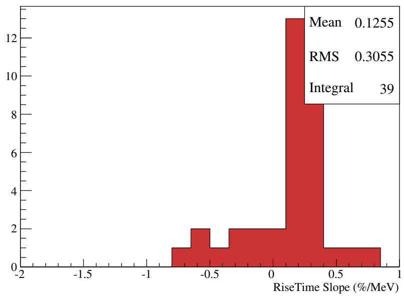

(b) TR analysis

Figure 5.9. Rise time slope of all channels, data of the first calibration of the Three Towers detector.

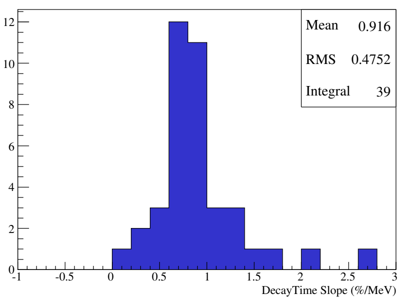

(a) STD analysis

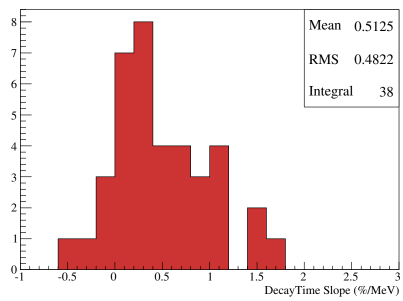

(b) TR analysis

Figure 5.10. Decay time slope of all channels, data of the first calibration of the Three Towers detector. The outlier of the TR distribution is channel 63 with a decay time slope of 3.2 %/MeV and will be discussed in section 5.5.

As already stated the crystals of this detector are sufficiently aged so that the ^{210}Po contamination is not enough to evaluate the amplitude dependence on baseline using the 5407 keV α line. The evaluation has been made using the events of the 2615 keV γ line, the highest line in the calibration spectrum. The comparison

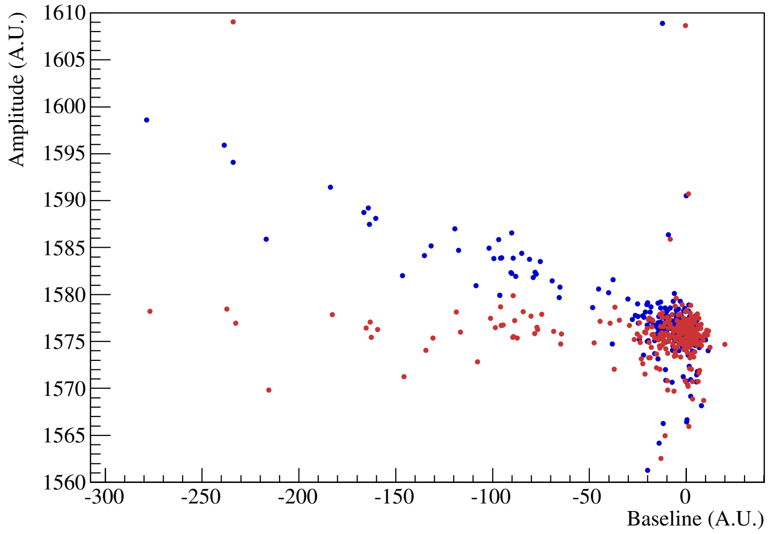

Figure 5.11. Slope of the 2615 keV line in the STD analysis before stabilization (blue) and in the TR one (red). Data from the first calibration runs of the Three Towers detector, channel 1.

between STD and TR data of channel 1 is shown in figure 5.11 where it can be seen that slope of TR data is negligible. The comparison of the amplitude slopes on all channels is shown in figure 5.12, the average slope is almost zero in the TR analysis case, while in the STD case it is about 3.5%.

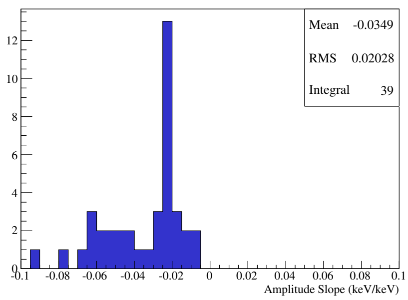

(a) STD analysis

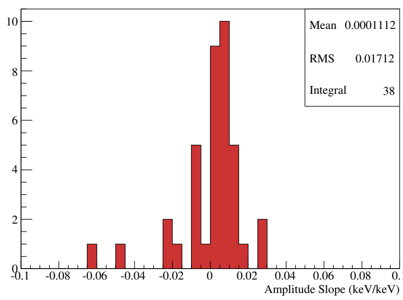

(b) TR analysis

Figure 5.12. Slope of the 2615 keV γ line, data from the first calibration runs of the Three Towers detector. The outlier of the TR distribution is channel 57 with a slope of -0.13 (keV/keV), and will be discussed in section 5.5.

The linearity of the calibration function has been evaluated fitting the positions of the energy peaks with a line ($E = c\,x$) and computing the χ^2 of the residuals (see section 4.4.1). The residuals of channel 1 are shown in figure 5.13, where it can be seen that the TR data are much closer to linearity than STD data. This result is obtained almost on all channels, as shown in figure 5.14.

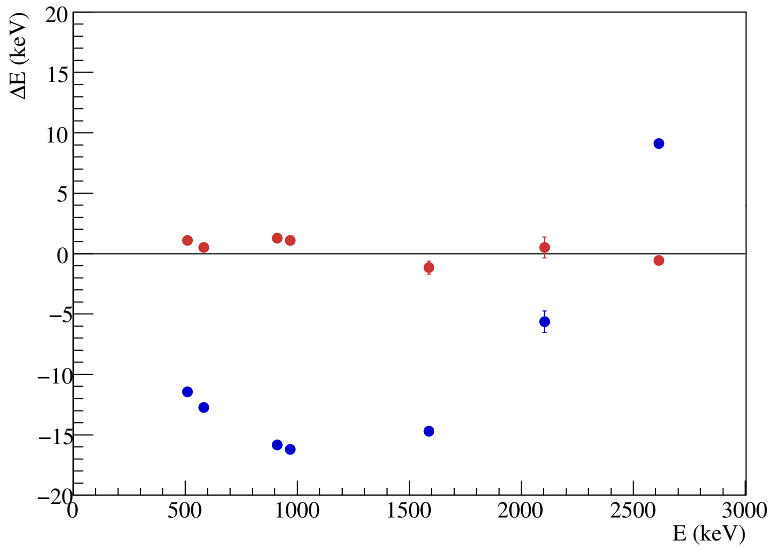

Figure 5.13. Residuals of a linear calibration function applied to STD data (blue) and TR data (red). The χ^2/ndf is 3500 and 22 respectively.

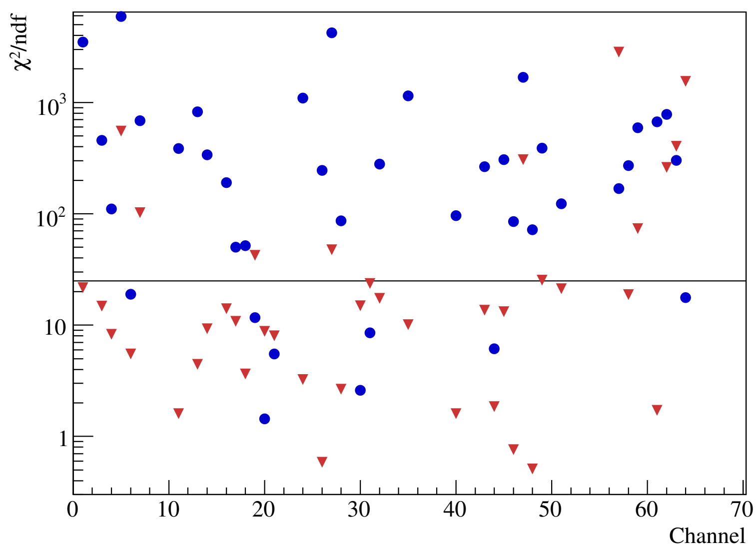

Figure 5.14. χ^2/ndf of a linear calibration function on all channel in the STD (blue) and TR (red) analysis. The threshold to reject a calibration is usually set to 25.

In conclusion the shape dependence on energy is reduced with respect to STD data, the amplitude dependence on baseline is close to zero and the calibration function is a close to a line almost on all channels. A few channels (about 15%) are not well corrected and will be discussed in section 5.5.

Concerning the STD analysis, we have seen that the 1461 keV line of a ^{40}K source is used to perform the stabilization. This line is in the middle of the calibration spectrum and the dependence of the amplitude with the baseline worsens its resolution and shifts its position. These effects makes this line difficult to recognize in a reliable way and make the stabilization step hard or even impossible in some case. This problem was not present in the analysis of CCVR, where the 5407 keV line of ^{210}Po stands out in the energy spectrum. TR data on the other hand are not sensitive to baseline variations so that the peak position is constant in time. Given this advantage and the better calibration function, it was decided to use the TR as official analysis in place of the STD one. Given that the 1461 keV line is easy to recognize with TR data, it was used to stabilize the TR data itself, removing the residual amplitude drift.

One of the purposes of this work was to evaluate the possibility of avoiding the use of the stabilization. In CUORE it will be made with the heater, that can be a source of instabilities (see section 4.5). In the next section we will compare the results obtained with the TR analysis stabilized with ^{40}K (TR-stabilized) and TR analysis without stabilization (TR).

5.4 Results on background data

The residual amplitude drift has been evaluated checking the position of the 1461 keV line in each run. An example is shown in figure 5.15, where the amplitude drifts of a good channel and a bad one are plotted.

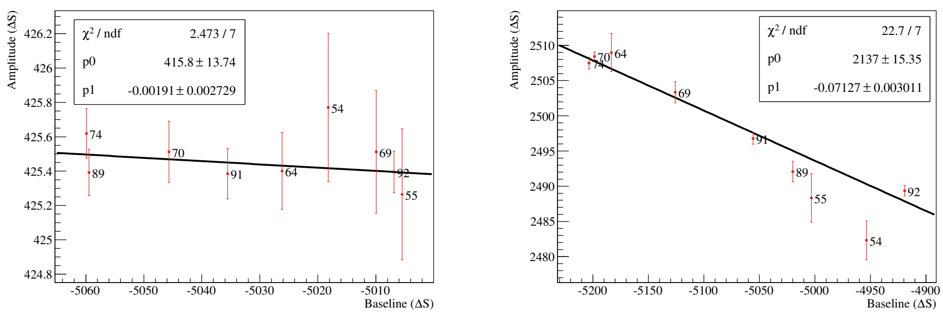

(a) Channel 46 (b) Channel 57

Figure 5.15. Evaluation of the residual slope of the 1461 keV γ line, example of a good (left) and a bad (right) channel. Background runs corresponding to the first 15 days of data taking of the Three Towers detector.

From the slope distribution on all channels shown in figure 5.16, we can see that almost all channels are contained in a 0.5% band, meaning that for a 100 keV baseline variation the amplitude variation is less then 0.5 keV. The outlying channels, in particular channels 47, 57 and 64, are of particular interest since they will be useful to understand the missing pieces of the model (see section 5.5).

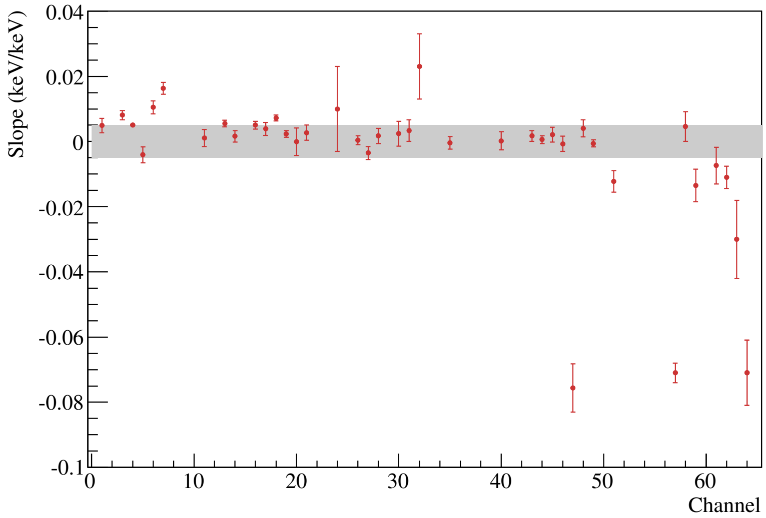

Figure 5.16. Residual slope of the 1461 keV γ line on all channels, background data acquired in the first 15 days of data taking of the Three Towers detector. Almost all channel are contained in a ± 0.005 range, the few outliers are described in section 5.5.

As final result we compare the resolution obtained on the 2615 keV γ line visible in the background. This line comes from the natural ^{232}Th contamination of the environment and has a very low rate. The sum spectrum of this line over all crystals gives an idea of what is the effective resolution in the 0νDBD region, the resolution that affects the final result of the CUORE experiment. From the distributions shown in figure 5.17, the resolution is evaluated to be 4.7 ± 0.5 keV FWHM for the TR analysis with stabilization and 6.3 ± 0.7 keV FWHM for the TR analysis without stabilization.

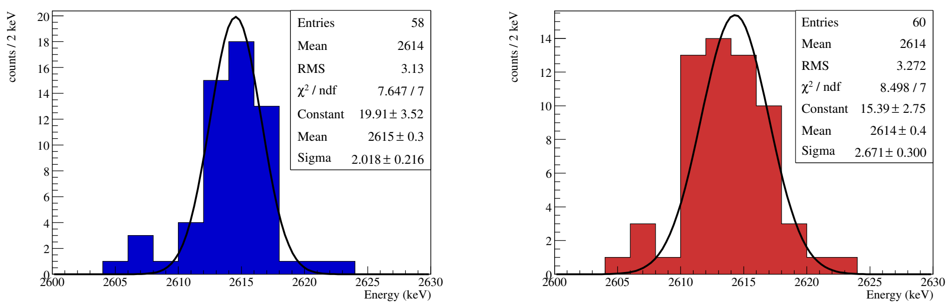

(a) TR-stabilized analysis (b) TR analysis

Figure 5.17. Distribution of the 2615 keV γ line summed over all crystals for the stabilized TR analysis (left) and the non stabilized one (right). Background data acquired in the first 15 days of data taking of the Three Towers detector.

5.5 Future developments

We have seen that the TR algorithm removes almost all the non linearities of the data. A few channels is not corrected, effect that is particularly evident in the linearity of the calibration function and in the amplitude slope. Looking at the distribution of the χ^2 of the linear calibration function shown in figure 5.14 and at the distribution of the amplitude slope shown in figure 5.16, we see that when the amplitude slope is high, also the linear calibration χ^2 is high. As the model parameters have been measured with precision, this effect reveals an incompleteness of the model.

Comparing the TR pulse of a well corrected channel and of a bad one, we see that the shape of the latter exhibits a strange behavior (see figure 5.18). After reaching its maximum the pulse goes down and then up again, as if there was an undershooting. The corresponding STD pulse does not exhibits this behavior since it is masked by the RC cutoff created by the parasitic capacitances and the bolometer resistance.

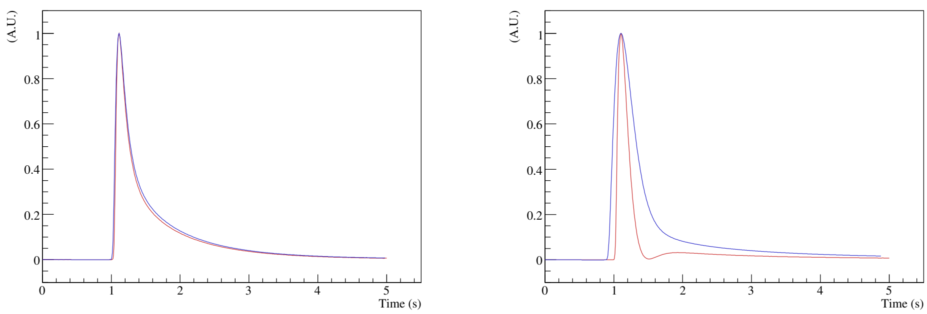

(a) Channel 46 (b) Channel 57

Figure 5.18. Comparison between the average pulse made on STD data (blue) and TR data (red). On the left a channel with small amplitude slope, on the right a channel with high amplitude slope (see figure 5.15).

This effect is visible on channels 47, 57 and 64, the worst ones in terms of amplitude slope and calibration linearity. It can be addressed to the electrothermal feedback (see sections 2.2 and 3.2.4) and can be qualitatively interpreted as follows. When the temperature increases, the variation of the power injected in the thermistor is negative, if this variation is too high it can even decrease the signal. The electrothermal feedback hypothesis is also supported by the fact that this kind of pulses is visible when the bolometer operates after the inversion point of the load curve (see section 2.2). Crossing this point the thermistor is so warm that even if the current in it is higher, the resistance is smaller so that the net voltage decreases.

The next step of this model will be the inclusion of the electrothermal feedback and the study of the dependence on the position on the load curve.

Conclusions

In this Ph.D. work I developed a model of the response function of the CUORE bolometers. The non-linearity of bolometer signals has been found to be dominated by the thermistor and by the biasing circuit used to operate the thermistor. The model is based on the description of these elements, without including the thermal part of the bolometer that contains unmeasurable parameters.

A signal simulator has been developed. It is able to reproduce the non-linearities of the data, in particular it reproduces the pulse shape dependence on energy and the pulse amplitude dependence on the base temperature. This is the first simulation engine of the response function of TeO_2 bolometers and it is used by the collaboration to test trigger efficiencies and data analysis algorithms.

Given the good performances of the model in reproducing the data, I created a digital filter that is able to remove the non-linearities. This filter transforms the voltage samples acquired by the ADC into samples proportional to the temperature variation of the thermistor (TR), a much more linear quantity. The algorithm has been included in the official data analysis of the currently running Three Towers detector. This is the first time in the analysis of TeO_2 bolometers that the physics of the detector is used, leading to great improvements: the shape dependence on energy is halved, the amplitude dependence on base temperature is removed, and the calibration function is very close to a line.
Only 15% of the bolometers are not well linearized by this algorithm, and new tests have been planned to understand the missing piece of the model.

The analysis based on TR can avoid the use of the heater to remove the temperature dependence, the resolution is evaluated to be just 30% worse than what obtained with an ideal correction. This makes TR a valid alternative when the heater is broken or when grounding problems compromise its behavior and render the data unusable, reducing the live time of the experiment. A better behaving calibration function could also shorten the time needed to calibrate the detector, which is currently one of the biggest issues of CUORE.

Appendix A

Thermal response analysis on the CCVR detector

Table A.1. Shape parameters and resolution dependence on the derivative algorithm, MonteCarlo data.

Algo	Rise Slope $\%/MeV$	Decay Slope $\%/MeV$	Heater Res (%)	Heater Slope
channel 1				
STD	-0.103 ± 0.012	0.539 ± 0.033	0.1402 ± 0.0035	-0.02563 ± 0.00018
D2P	0.0024 ± 0.0098	-0.031 ± 0.030	0.1420 ± 0.0034	-0.00008 ± 0.00018
D3P	0.0031 ± 0.0089	-0.033 ± 0.030	0.1405 ± 0.0035	0.00024 ± 0.00018
D5P	0.0079 ± 0.0090	-0.031 ± 0.030	0.1398 ± 0.0034	0.00021 ± 0.00018
D2PF	-0.020 ± 0.013	-0.029 ± 0.030	0.1408 ± 0.0035	0.00058 ± 0.00018
D3PB	0.0105 ± 0.0095	-0.036 ± 0.030	0.1422 ± 0.0035	0.00016 ± 0.00018
D3PF	0.0143 ± 0.0089	-0.036 ± 0.030	0.1413 ± 0.0035	0.00018 ± 0.00018
channel 2				
STD	-0.217 ± 0.010	0.550 ± 0.020	0.1534 ± 0.0037	-0.02524 ± 0.00014
D2P	0.0063 ± 0.0075	0.018 ± 0.019	0.1547 ± 0.0047	-0.00029 ± 0.00018
D3P	0.040 ± 0.011	0.013 ± 0.020	0.1550 ± 0.0045	0.00022 ± 0.00017
D5P	0.030 ± 0.011	0.012 ± 0.021	0.1544 ± 0.0046	0.00017 ± 0.00017
D2PF	0.0646 ± 0.0090	-0.016 ± 0.019	0.1562 ± 0.0037	0.00067 ± 0.00014
D3PB	0.044 ± 0.012	0.011 ± 0.021	0.1548 ± 0.0046	0.00003 ± 0.00017
D3PF	0.044 ± 0.010	-0.006 ± 0.019	0.1566 ± 0.0037	0.00006 ± 0.00015
channel 3				
STD	-0.6780 ± 0.0031	1.4675 ± 0.0062	0.1015 ± 0.0022	-0.05628 ± 0.00017
D2P	0.0109 ± 0.0028	0.0501 ± 0.0048	0.1069 ± 0.0024	-0.00103 ± 0.00018
D3P	0.1421 ± 0.0029	0.0087 ± 0.0051	0.1062 ± 0.0024	0.00041 ± 0.00018
D5P	0.1870 ± 0.0026	0.0036 ± 0.0053	0.1063 ± 0.0024	0.00016 ± 0.00018
D2PF	0.2867 ± 0.0033	-0.0279 ± 0.0054	0.1064 ± 0.0024	0.00153 ± 0.00017
D3PB	0.1356 ± 0.0026	-0.0160 ± 0.0051	0.1070 ± 0.0024	-0.00041 ± 0.00017
D3PF	0.1734 ± 0.0023	-0.0089 ± 0.0051	0.1062 ± 0.0024	-0.00037 ± 0.00018
channel 4				
STD	-0.3634 ± 0.0049	0.9606 ± 0.0084	0.0991 ± 0.0024	-0.04671 ± 0.00015
D2P	0.0383 ± 0.0051	0.0435 ± 0.0069	0.1026 ± 0.0025	-0.00078 ± 0.00017
D3P	0.0841 ± 0.0045	0.0028 ± 0.0072	0.1026 ± 0.0025	0.00009 ± 0.00017
D5P	0.1004 ± 0.0046	0.0000 ± 0.0073	0.1026 ± 0.0025	-0.00003 ± 0.00017
D2PF	0.1901 ± 0.0039	-0.0410 ± 0.0076	0.1033 ± 0.0025	0.00083 ± 0.00016

Continued on Next Page...

Algo	Rise Slope $\%/MeV$	Decay Slope $\%/MeV$	Heater Res (%)	Heater Slope
D3PB	0.0850 ± 0.0049	-0.0102 ± 0.0073	0.1039 ± 0.0025	-0.00026 ± 0.00017
D3PF	0.1528 ± 0.0048	-0.0082 ± 0.0073	0.1025 ± 0.0024	-0.00025 ± 0.00017
channel 5				
STD	-0.4097 ± 0.0060	0.936 ± 0.016	0.1203 ± 0.0031	-0.05711 ± 0.00024
D2P	0.0156 ± 0.0067	-0.013 ± 0.014	0.1231 ± 0.0032	-0.00066 ± 0.00025
D3P	0.0215 ± 0.0058	-0.019 ± 0.014	0.1233 ± 0.0032	0.00056 ± 0.00025
D5P	0.0363 ± 0.0058	-0.018 ± 0.014	0.1235 ± 0.0032	0.00040 ± 0.00025
D2PF	0.0254 ± 0.0052	-0.023 ± 0.014	0.1236 ± 0.0032	0.00175 ± 0.00025
D3PB	0.0690 ± 0.0060	-0.020 ± 0.014	0.1237 ± 0.0032	0.00003 ± 0.00025
D3PF	0.0614 ± 0.0056	-0.018 ± 0.014	0.1232 ± 0.0033	0.00009 ± 0.00025
channel 6				
STD	-0.4287 ± 0.0046	0.9790 ± 0.0092	0.0775 ± 0.0019	-0.04351 ± 0.00013
D2P	-0.0111 ± 0.0070	0.0142 ± 0.0086	0.0809 ± 0.0020	-0.00092 ± 0.00014
D3P	0.0637 ± 0.0059	-0.0058 ± 0.0087	0.0807 ± 0.0020	-0.00016 ± 0.00014
D5P	0.0836 ± 0.0062	-0.0085 ± 0.0088	0.0808 ± 0.0020	-0.00027 ± 0.00014
D2PF	0.1230 ± 0.0062	-0.0143 ± 0.0089	0.0808 ± 0.0020	0.00049 ± 0.00014
D3PB	0.0835 ± 0.0062	-0.0163 ± 0.0090	0.0808 ± 0.0020	-0.00040 ± 0.00014
D3PF	0.1277 ± 0.0064	-0.0136 ± 0.0088	0.0806 ± 0.0020	-0.00045 ± 0.00014
channel 7				
STD	-0.6639 ± 0.0037	0.9244 ± 0.0065	0.0895 ± 0.0021	-0.03137 ± 0.00014
D2P	0.0469 ± 0.0026	0.0546 ± 0.0057	0.0912 ± 0.0020	-0.00007 ± 0.00018
D3P	0.1090 ± 0.0039	-0.0284 ± 0.0057	0.0908 ± 0.0020	0.00050 ± 0.00017
D5P	0.1111 ± 0.0041	-0.0227 ± 0.0057	0.0907 ± 0.0020	0.00037 ± 0.00017
D2PF	0.1615 ± 0.0035	-0.1365 ± 0.0059	0.0913 ± 0.0020	0.00085 ± 0.00016
D3PB	0.0991 ± 0.0047	-0.0023 ± 0.0055	0.0912 ± 0.0020	0.00018 ± 0.00017
D3PF	0.1275 ± 0.0046	-0.0209 ± 0.0056	0.0913 ± 0.0020	0.00014 ± 0.00017

Table A.2. Shape parameters and resolution dependence on the error on $1/m_1$, MonteCarlo data.

Error (%)	Rise Slope $\%/MeV$	Decay Slope $\%/MeV$	Heater Res (%)	Heater Slope
channel 1				
-9	-0.0038 ± 0.0091	-0.087 ± 0.030	0.1681 ± 0.0038	0.00298 ± 0.00018
-6	0.0001 ± 0.0086	-0.064 ± 0.029	0.1570 ± 0.0033	0.00198 ± 0.00018
-3	0.0011 ± 0.0093	-0.042 ± 0.031	0.1514 ± 0.0033	0.00107 ± 0.00018
0	0.0034 ± 0.0090	-0.033 ± 0.030	0.1487 ± 0.0035	0.00024 ± 0.00018
3	0.0027 ± 0.0090	-0.020 ± 0.030	0.1495 ± 0.0035	-0.00047 ± 0.00018
6	0.0017 ± 0.0090	-0.001 ± 0.030	0.1528 ± 0.0036	-0.00124 ± 0.00018
9	0.0005 ± 0.0091	0.013 ± 0.030	0.1571 ± 0.0037	-0.00196 ± 0.00018
channel 2				
-9	0.039 ± 0.011	-0.056 ± 0.019	0.1677 ± 0.0030	0.00308 ± 0.00015
-6	0.043 ± 0.011	-0.026 ± 0.019	0.1533 ± 0.0031	0.00206 ± 0.00017
-3	0.045 ± 0.011	-0.009 ± 0.021	0.1538 ± 0.0032	0.00110 ± 0.00017
0	0.040 ± 0.011	0.015 ± 0.020	0.1497 ± 0.0030	0.00022 ± 0.00017
3	0.012 ± 0.010	0.009 ± 0.018	0.1481 ± 0.0029	-0.00063 ± 0.00017
6	0.025 ± 0.011	0.047 ± 0.020	0.1515 ± 0.0030	-0.00143 ± 0.00017
9	0.018 ± 0.011	0.049 ± 0.019	0.1554 ± 0.0027	-0.00220 ± 0.00015

Continued on Next Page...

Error (%)	Rise Slope $\%/MeV$	Decay Slope $\%/MeV$	Heater Res (%)	Heater Slope
channel 3				
-9	0.1836 ± 0.0024	-0.1430 ± 0.0050	0.1517 ± 0.0025	0.00773 ± 0.00018
-6	0.1711 ± 0.0023	-0.0882 ± 0.0049	0.1270 ± 0.0022	0.00507 ± 0.00018
-3	0.1684 ± 0.0026	-0.0433 ± 0.0053	0.1097 ± 0.0019	0.00259 ± 0.00018
0	0.1417 ± 0.0028	0.0070 ± 0.0051	0.1029 ± 0.0019	0.00041 ± 0.00018
3	0.1277 ± 0.0037	0.0551 ± 0.0052	0.1053 ± 0.0019	-0.00171 ± 0.00018
6	0.0796 ± 0.0040	0.0999 ± 0.0052	0.1154 ± 0.0019	-0.00377 ± 0.00018
9	0.0767 ± 0.0040	0.1429 ± 0.0053	0.1308 ± 0.0022	-0.00574 ± 0.00018
channel 4				
-9	0.1012 ± 0.0044	-0.1060 ± 0.0072	0.1318 ± 0.0021	0.00608 ± 0.00017
-6	0.0957 ± 0.0043	-0.0688 ± 0.0070	0.1140 ± 0.0019	0.00392 ± 0.00017
-3	0.0913 ± 0.0045	-0.0391 ± 0.0073	0.1033 ± 0.0018	0.00194 ± 0.00017
0	0.0841 ± 0.0045	0.0028 ± 0.0072	0.0979 ± 0.0018	0.00009 ± 0.00017
3	0.0746 ± 0.0045	0.0358 ± 0.0073	0.1015 ± 0.0020	-0.00164 ± 0.00016
6	0.0583 ± 0.0042	0.0691 ± 0.0073	0.1106 ± 0.0021	-0.00332 ± 0.00017
9	0.0595 ± 0.0041	0.1013 ± 0.0073	0.1222 ± 0.0022	-0.00497 ± 0.00017
channel 5				
-9	0.0264 ± 0.0059	-0.114 ± 0.014	0.1490 ± 0.0028	0.00733 ± 0.00025
-6	0.0248 ± 0.0057	-0.079 ± 0.014	0.1319 ± 0.0026	0.00490 ± 0.00025
-3	0.0271 ± 0.0061	-0.043 ± 0.014	0.1222 ± 0.0023	0.00264 ± 0.00025
0	0.0209 ± 0.0058	-0.022 ± 0.014	0.1167 ± 0.0025	0.00056 ± 0.00025
3	0.0180 ± 0.0058	0.008 ± 0.014	0.1177 ± 0.0026	-0.00131 ± 0.00025
6	0.0150 ± 0.0058	0.035 ± 0.014	0.1228 ± 0.0027	-0.00315 ± 0.00025
9	0.0108 ± 0.0058	0.060 ± 0.014	0.1311 ± 0.0029	-0.00492 ± 0.00025
channel 6				
-9	0.0867 ± 0.0053	-0.1002 ± 0.0086	0.1066 ± 0.0019	0.00510 ± 0.00014
-6	0.0778 ± 0.0052	-0.0622 ± 0.0081	0.0912 ± 0.0017	0.00321 ± 0.00014
-3	0.0791 ± 0.0058	-0.0316 ± 0.0090	0.0814 ± 0.0015	0.00145 ± 0.00014
0	0.0631 ± 0.0058	-0.0057 ± 0.0086	0.0790 ± 0.0015	-0.00016 ± 0.00014
3	0.0506 ± 0.0060	0.0222 ± 0.0085	0.0833 ± 0.0016	-0.00158 ± 0.00014
6	0.0222 ± 0.0054	0.0493 ± 0.0086	0.0898 ± 0.0018	-0.00307 ± 0.00014
9	0.0219 ± 0.0051	0.0746 ± 0.0087	0.1017 ± 0.0019	-0.00449 ± 0.00014
channel 7				
-9	0.2127 ± 0.0047	-0.1854 ± 0.0056	0.1203 ± 0.0021	0.00538 ± 0.00017
-6	0.1999 ± 0.0046	-0.1221 ± 0.0054	0.1062 ± 0.0019	0.00362 ± 0.00017
-3	0.1495 ± 0.0044	-0.0783 ± 0.0057	0.0985 ± 0.0018	0.00201 ± 0.00017
0	0.1098 ± 0.0039	-0.0276 ± 0.0057	0.0941 ± 0.0017	0.00050 ± 0.00017
3	0.1053 ± 0.0039	0.0190 ± 0.0057	0.0947 ± 0.0017	-0.00095 ± 0.00017
6	0.0992 ± 0.0039	0.0722 ± 0.0056	0.0995 ± 0.0017	-0.00238 ± 0.00017
9	0.0907 ± 0.0039	0.1206 ± 0.0057	0.1050 ± 0.0018	-0.00375 ± 0.00017

Table A.3. Shape parameters and resolution dependence on the error on m_2, MonteCarlo data.

Error (%)	Rise Slope $\%/MeV$	Decay Slope $\%/MeV$	Heater Res (%)	Heater Slope
channel 1				

Continued on Next Page...

Error (%)	Rise Slope $\%/MeV$	Decay Slope $\%/MeV$	Heater Res (%)	Heater Slope
-20	-0.0248 ± 0.0096	-0.031 ± 0.030	0.1495 ± 0.0035	0.00047 ± 0.00018
-10	-0.0172 ± 0.0091	-0.032 ± 0.030	0.1489 ± 0.0035	0.00037 ± 0.00018
-05	-0.0065 ± 0.0090	-0.037 ± 0.030	0.1490 ± 0.0035	0.00033 ± 0.00018
00	0.0034 ± 0.0090	-0.033 ± 0.030	0.1487 ± 0.0035	0.00024 ± 0.00018
05	0.0099 ± 0.0090	-0.033 ± 0.030	0.1480 ± 0.0034	0.00017 ± 0.00018
10	0.0156 ± 0.0091	-0.032 ± 0.030	0.1488 ± 0.0036	0.00010 ± 0.00018
20	0.017 ± 0.010	-0.031 ± 0.030	0.1488 ± 0.0035	-0.00001 ± 0.00018
channel 2				
-20	-0.034 ± 0.010	0.010 ± 0.020	0.1529 ± 0.0031	0.00075 ± 0.00017
-10	0.021 ± 0.011	0.013 ± 0.020	0.1515 ± 0.0031	0.00050 ± 0.00017
-05	0.032 ± 0.011	0.014 ± 0.020	0.1502 ± 0.0030	0.00036 ± 0.00017
00	0.040 ± 0.011	0.015 ± 0.020	0.1497 ± 0.0030	0.00022 ± 0.00017
05	0.031 ± 0.011	0.014 ± 0.020	0.1481 ± 0.0029	0.00006 ± 0.00017
10	0.038 ± 0.011	0.013 ± 0.020	0.1487 ± 0.0030	-0.00009 ± 0.00017
20	0.095 ± 0.058	-0.09 ± 0.11	0.1470 ± 0.0025	-0.00040 ± 0.00015
channel 3				
-20	0.0293 ± 0.0024	0.0183 ± 0.0052	0.1107 ± 0.0019	0.00270 ± 0.00017
-10	0.0809 ± 0.0024	0.0104 ± 0.0051	0.1064 ± 0.0019	0.00153 ± 0.00018
-05	0.250 ± 0.012	0.026 ± 0.027	0.1049 ± 0.0019	0.00103 ± 0.00017
00	0.1417 ± 0.0028	0.0070 ± 0.0051	0.1029 ± 0.0019	0.00041 ± 0.00018
05	0.397 ± 0.021	0.021 ± 0.027	0.1017 ± 0.0019	-0.00019 ± 0.00018
10	0.1265 ± 0.0039	0.0098 ± 0.0052	0.1022 ± 0.0019	-0.00082 ± 0.00018
20	0.1778 ± 0.0038	0.0188 ± 0.0050	0.1069 ± 0.0020	-0.00207 ± 0.00018
channel 4				
-20	0.0330 ± 0.0048	-0.0026 ± 0.0073	0.1034 ± 0.0018	0.00192 ± 0.00016
-10	0.0517 ± 0.0044	-0.0078 ± 0.0073	0.1003 ± 0.0018	0.00099 ± 0.00016
-05	0.0675 ± 0.0044	-0.0029 ± 0.0072	0.0989 ± 0.0018	0.00057 ± 0.00016
00	0.0841 ± 0.0045	0.0028 ± 0.0072	0.0979 ± 0.0018	0.00009 ± 0.00017
05	0.0994 ± 0.0044	0.0114 ± 0.0073	0.0981 ± 0.0018	-0.00037 ± 0.00017
10	0.1006 ± 0.0041	0.0149 ± 0.0073	0.0994 ± 0.0019	-0.00087 ± 0.00017
20	0.1281 ± 0.0042	0.0440 ± 0.0072	0.1028 ± 0.0020	-0.00189 ± 0.00017
channel 5				
-20	-0.0576 ± 0.0061	-0.010 ± 0.014	0.1200 ± 0.0024	0.00194 ± 0.00025
-10	-0.0181 ± 0.0059	-0.016 ± 0.014	0.1171 ± 0.0024	0.00126 ± 0.00025
-05	0.0003 ± 0.0059	-0.020 ± 0.014	0.1163 ± 0.0024	0.00092 ± 0.00025
00	0.0209 ± 0.0058	-0.022 ± 0.014	0.1167 ± 0.0025	0.00056 ± 0.00025
05	0.0436 ± 0.0057	-0.021 ± 0.014	0.1164 ± 0.0025	0.00023 ± 0.00025
10	0.0684 ± 0.0057	-0.023 ± 0.014	0.1164 ± 0.0025	-0.00015 ± 0.00025
20	0.1260 ± 0.0057	-0.029 ± 0.014	0.1161 ± 0.0025	-0.00090 ± 0.00025
channel 6				
-20	-0.0535 ± 0.0053	0.0099 ± 0.0085	0.0806 ± 0.0015	0.00118 ± 0.00014
-10	0.0136 ± 0.0053	0.0019 ± 0.0086	0.0790 ± 0.0015	0.00052 ± 0.00014
-05	0.0371 ± 0.0055	-0.0030 ± 0.0087	0.0785 ± 0.0015	0.00018 ± 0.00014
00	0.0631 ± 0.0058	-0.0057 ± 0.0086	0.0790 ± 0.0015	-0.00016 ± 0.00014
05	0.0893 ± 0.0060	-0.0050 ± 0.0086	0.0796 ± 0.0016	-0.00048 ± 0.00014
10	0.0813 ± 0.0051	-0.0063 ± 0.0086	0.0796 ± 0.0016	-0.00082 ± 0.00014
20	0.1249 ± 0.0054	-0.0057 ± 0.0088	0.0817 ± 0.0015	-0.00153 ± 0.00014
channel 7				
-20	0.1010 ± 0.0047	-0.1330 ± 0.0055	0.1026 ± 0.0018	0.00285 ± 0.00016
-10	0.1330 ± 0.0047	-0.0918 ± 0.0057	0.0974 ± 0.0018	0.00167 ± 0.00017

Continued on Next Page…

Error (%)	Rise Slope $\%/MeV$	Decay Slope $\%/MeV$	Heater Res (%)	Heater Slope
-05	0.1505 ± 0.0048	-0.0589 ± 0.0055	0.0950 ± 0.0018	0.00110 ± 0.00017
00	0.1098 ± 0.0039	-0.0276 ± 0.0057	0.0941 ± 0.0017	0.00050 ± 0.00017
05	0.1159 ± 0.0039	0.0093 ± 0.0056	0.0939 ± 0.0017	-0.00011 ± 0.00017
10	0.1234 ± 0.0039	0.0599 ± 0.0057	0.0940 ± 0.0017	-0.00073 ± 0.00017
20	0.1400 ± 0.0040	0.1744 ± 0.0059	0.0973 ± 0.0017	-0.00209 ± 0.00018

Appendix B

Precision measurements on the Three Towers detector

Table B.1. Bolometers setup of the Three Towers detector. The biasing circuit parameters (V_B, G, G_S, R_L) are nominal.

Ch	Tower	Crystal	V_B (V)	G V/V	G_S V/V	R_L G Ω
1	1	B10	4.940	4133	448	54
3	1	B49	6.787	7520	448	54
4	1	B34	8.631	10009	448	54
5	2	B15	2.164	1942	448	54
6	2	B15	3.628	10009	448	54
7	2	B35	3.005	2938	448	54
11	3	B39	4.940	6324	448	54
13	1	B53	8.631	10009	448	54
14	1	B52	7.121	10009	448	54
16	1	B55	4.628	10009	448	54
17	1	B41	7.998	10009	448	54
18	2	B25	4.284	10009	448	54
19	2	B25	7.685	10009	448	54
20	2	B46	7.998	10009	448	54
21	2	B46	7.998	10009	448	54
24	3	B7	4.284	4731	448	54
26	1	B12	7.685	10009	448	54
27	1	B12	4.940	5428	448	54
28	1	B49	6.787	10009	448	54
30	1	B10	8.962	10009	448	54
31	1	B51	4.628	10009	448	54
32	1	B23	5.250	10009	448	54
35	2	B64	4.940	5030	448	54
40	2	B24	6.152	10009	448	54
43	1	B53	7.998	10009	448	54
44	1	B38	9.636	10009	448	54
45	1	B52	5.873	7918	448	54
46	1	B55	5.873	10009	448	54
47	1	B41	1.519	2241	448	54
48	1	B57	6.472	6922	448	54
49	1	B57	4.628	6922	448	54
51	2	B68	3.337	7520	448	54
57	3	B2	1.199	2241	448	54
58	3	B7	7.364	10009	448	54
59	3	B13	3.628	4731	448	54
61	3	B39	4.628	5030	448	54
62	3	B40	4.940	4432	448	54
63	3	B8	3.337	2540	448	54
64	3	B20	3.337	2540	448	54

Table B.2. Measured thermistor parameters of the Three Towers detector

Ch	V_S (mV)	$V_{R_S}^G$ (mV)	$\sigma_{V_{R_S}^G}$ (mV)	R_S (M Ω)
1	5166.91 ± 0.57	4023.80 ± 0.29	0.66	98.359
3	-4944.55 ± 0.83	3045.685 ± 0.073	0.14	54.145
4	-4821.75 ± 0.11	2489.145 ± 0.020	0.62	34.7844
5	-4989.200 ± 0.096	5683.035 ± 0.037	0.31	318.414
6	-5239.0 ± 1.1	3121.685 ± 0.086	0.30	103.914
7	-4872.920 ± 0.091	4404.645 ± 0.023	1.8	177.2578
11	-4803.76 ± 0.25	3546.100 ± 0.015	1.1	86.6635
13	-4805.56 ± 0.38	2225.005 ± 0.013	0.98	31.0910
14	-4896.57 ± 0.37	2297.565 ± 0.013	0.92	38.9184
16	-4730.64 ± 0.43	2473.125 ± 0.046	2.2	64.489
17	-4710.26 ± 0.54	2666.815 ± 0.023	1.6	40.2208
18	-4778.45 ± 0.24	3603.862 ± 0.071	1.3	101.590
19	-5129.62 ± 0.17	2764.795 ± 0.015	0.45	43.3994
20	-4507.79 ± 0.42	2328.135 ± 0.024	0.32	35.1096
21	-4695.86 ± 0.26	2919.3150 ± 0.0065	1.5	44.03214
24	-5083.21 ± 0.97	3576.19 ± 0.15	0.83	100.809
26	-4816.90 ± 0.34	2249.780 ± 0.017	1.3	34.5604
27	-5013.23 ± 0.35	3407.750 ± 0.018	0.97	82.8221
28	-4929.6 ± 1.0	2982.440 ± 0.063	0.92	50.003
30	-4923.82 ± 0.49	2249.88 ± 0.18	0.087	29.206
31	-4975.9 ± 5.2	2619.93 ± 0.94	4.0	68.11
32	-4952.2 ± 1.1	3335.095 ± 0.017	0.31	82.3535
35	-5028.47 ± 0.33	3597.025 ± 0.016	0.27	87.7890
40	-4871.47 ± 0.61	2841.785 ± 0.032	0.28	54.7916
43	-5012.83 ± 0.26	2391.6850 ± 0.0090	0.19	38.7590
44	-5007.14 ± 0.38	1752.245 ± 0.026	1.5	23.7096
45	-4984.29 ± 0.41	3479.720 ± 0.013	0.91	70.2485
46	-5199.14 ± 0.90	3341.415 ± 0.040	0.27	63.7081
47	-5019.66 ± 0.23	6632.500 ± 0.052	2.6	509.519
48	-5350.27 ± 0.47	3978.535 ± 0.025	0.25	77.3896
49	-5208.87 ± 0.35	3573.580 ± 0.023	0.76	90.8930
51	-5303.80 ± 0.72	3360.225 ± 0.027	0.44	128.071
57	-4956.82 ± 0.69	5329.895 ± 0.045	2.2	536.575
58	-4580.59 ± 0.58	2369.320 ± 0.069	0.80	38.829
59	-5014.77 ± 0.36	4644.570 ± 0.051	0.50	162.184
61	-4872.25 ± 0.36	3383.415 ± 0.043	0.069	92.376
62	-4949.21 ± 0.40	3211.795 ± 0.041	0.59	80.010
63	-5084.62 ± 0.45	6816.00 ± 0.13	1.2	253.543
64	-4570.3 ± 1.2	7430.72 ± 0.35	12	285.37

Table B.3. Measured FE boards parameters of the Three Towers detector.

Ch	$V_B G_S$ (V)	G/G_S (V/V)	R_L (± 1 GΩ)
1	N/A	9.1931 ± 0.0041	N/A
3	N/A	16.747 ± 0.014	N/A
4	N/A	22.236 ± 0.012	N/A
5	N/A	4.30459 ± 0.00073	N/A
6	N/A	22.297 ± 0.021	N/A
7	N/A	6.5527 ± 0.0047	N/A
11	N/A	13.931 ± 0.021	N/A
13	N/A	22.149 ± 0.010	N/A
14	N/A	22.173 ± 0.011	N/A
16	N/A	22.208 ± 0.013	N/A
17	N/A	22.195 ± 0.015	N/A
18	N/A	22.2493 ± 0.0092	N/A
19	N/A	22.1620 ± 0.0094	N/A
20	N/A	22.124 ± 0.022	N/A
21	N/A	22.187 ± 0.020	N/A
24	N/A	10.5237 ± 0.0061	N/A
26	3394 ± 68	22.193 ± 0.019	52.1
27	2180 ± 44	12.0247 ± 0.0070	52.9
28	3003 ± 60	22.220 ± 0.015	50.3
30	3970 ± 79	22.230 ± 0.014	51.5
31	2072 ± 41	22.137 ± 0.037	53.8
32	2356 ± 47	22.423 ± 0.049	58.1
35	2196 ± 44	11.1967 ± 0.0091	53.5
40	2731 ± 55	22.174 ± 0.022	52.6
43	3532 ± 71	22.288 ± 0.015	57.2
44	4296 ± 86	22.172 ± 0.017	58.1
45	2639 ± 53	17.5822 ± 0.0095	53.2
46	2600 ± 52	22.240 ± 0.013	49.5
47	674 ± 13	4.9728 ± 0.0027	51.3
48	2878 ± 58	15.374 ± 0.015	55.9
49	2064 ± 41	15.3380 ± 0.0091	52.4
51	1486 ± 30	16.641 ± 0.016	56.5
57	528 ± 11	4.9720 ± 0.0049	52.6
58	3267 ± 65	22.160 ± 0.012	53.5
59	1597 ± 32	10.5142 ± 0.0070	55.6
61	2062 ± 41	11.192 ± 0.012	56.2
62	2183 ± 44	9.8640 ± 0.0046	54.3
63	1475 ± 29	5.6412 ± 0.0023	54.6
64	1486 ± 30	5.6371 ± 0.0021	56.8

Table B.4. Measured capacitances of the wires of the Three Towers detector. The c_p parameter is the sum of all contributions.

ch	R^t (Ω)	c_p^t (± 2 pF)	c_p^c (± 2 pF)	c_p^f (± 2 pF)	c_p^{FE} (± 2 pF)	c_p (pF)
1	100	10.3	118	0	0	128 ± 3
3	125	13.4	118	0	0	131 ± 3
4	105	10.9	116	0	0	127 ± 3
5	170	19.0	118	0	0	137 ± 3
6	180	20.3	118	0	0	138 ± 3
7	190	21.5	116	0	0	138 ± 3
11	293	34.4	116	0	0	150 ± 3
13	103	10.7	112	0	0	123 ± 3
14	128	13.8	111	0	0	125 ± 3
16	137	14.9	112	0	0	127 ± 3
17	105	10.9	111	0	0	122 ± 3
18	180	20.3	111	0	0	131 ± 3
19	174	19.5	110	0	0	130 ± 3
20	187	21.2	111	0	0	132 ± 3
21	202	23.1	111	0	0	134 ± 3
24	292	34.3	111	0	0	145 ± 3
26	108	11.3	250	83	15	359 ± 4
27	108	11.3	249	83	15	358 ± 4
28	126	13.5	250	83	15	362 ± 4
30	96	9.8	250	83	15	358 ± 4
31	127	13.7	251	70	15	350 ± 4
32	96	9.8	253	70	15	348 ± 4
35	222	25.6	252	70	15	363 ± 4
40	168	18.8	258	70	15	362 ± 4
43	100	10.3	263	86	15	374 ± 4
44	109	11.4	260	86	15	372 ± 4
45	130	14.0	259	86	15	374 ± 4
46	133	14.4	258	86	15	373 ± 4
47	102	10.5	259	86	15	371 ± 4
48	92	9.3	259	86	15	369 ± 4
49	96	9.8	267	83	15	375 ± 4
51	222	25.6	268	83	15	392 ± 4
57	260	30.3	272	86	15	403 ± 4
58	284	33.3	271	86	15	405 ± 4
59	294	34.6	270	86	15	406 ± 4
61	288	33.8	268	73	15	390 ± 4
62	293	34.4	267	73	15	389 ± 4
63	273	31.9	277	73	15	397 ± 4
64	253	29.4	274	73	15	391 ± 4

Bibliography

[1] J. Davis, Raymond, D. S. Harmer, and K. C. Hoffman, "Search for neutrinos from the sun," *Phys. Rev. Lett.*, vol. 20, pp. 1205–1209, 1968.

[2] P. Anselmann *et al.*, "Solar neutrinos observed by GALLEX at Gran Sasso," *Physics Letters B*, vol. 285, pp. 376–389, 1992.

[3] J. N. Abdurashitov *et al.*, "Measurement of the Solar Neutrino Capture Rate by SAGE and Implications for Neutrino Oscillations in Vacuum," *Physical Review Letters*, vol. 83, pp. 4686–4689, 1999, astro-ph/9907131v2.

[4] Q. R. Ahmad *et al.*, "Direct evidence for neutrino flavor transformation from neutral-current interactions in the Sudbury Neutrino Observatory," *Phys. Rev. Lett.*, vol. 89, p. 011301, 2002, nucl-ex/0204008.

[5] K. Eguchi *et al.*, "First results from KamLAND: Evidence for reactor anti- neutrino disappearance," *Phys. Rev. Lett.*, vol. 90, p. 021802, 2003, hep-ex/0212021.

[6] S. Abe *et al.*, "Precision Measurement of Neutrino Oscillation Parameters with KamLAND," *Phys. Rev. Lett.*, vol. 100, p. 221803, 2008, 0801.4589.

[7] Y. Fukuda *et al.*, "Evidence for oscillation of atmospheric neutrinos," *Phys. Rev. Lett.*, vol. 81, pp. 1562–1567, 1998, hep-ex/9807003.

[8] L.-L. Chau and W.-Y. Keung, "Comments on the Parametrization of the Kobayashi-Maskawa Matrix," *Phys. Rev. Lett.*, vol. 53, p. 1802, 1984.

[9] T. Schwetz, M. Tortola, and J. W. F. Valle, "Three-flavour neutrino oscillation update," 2008, 0808.2016.

[10] C. Kraus *et al.*, "Final Results from phase II of the Mainz Neutrino Mass Search in Tritium β Decay," *Eur. Phys. J.*, vol. C40, pp. 447–468, 2005, hep-ex/0412056.

[11] V. M. Lobashev *et al.*, "Direct search for neutrino mass and anomaly in the tritium beta-spectrum: Status of 'Troitsk neutrino mass' experiment," *Nucl. Phys. Proc. Suppl.*, vol. 91, pp. 280–286, 2001.

[12] G. Drexlin, "KATRIN: Direct measurement of a sub-eV neutrino mass," *Nucl. Phys. Proc. Suppl.*, vol. 145, pp. 263–267, 2005.

[13] A. Monfardini *et al.*, "The microcalorimeter arrays for a rhenium experiment (MARE): A next-generation calorimetric neutrino mass experiment," *Prog. Part. Nucl. Phys.*, vol. 57, pp. 68–70, 2006, hep-ex/0509038.

[14] S. R. Elliott, A. A. Hahn, and M. K. Moe, "Direct evidence for two-neutrino double-beta decay in Se- 82," *Phys. Rev. Lett.*, vol. 59, pp. 2020–2023, 1987.

[15] R. N. Mohapatra and P. B. Pal, *Massive Neutrinos in Physics and Astrophysics.* World Scientific, 3rd ed., 2004. ISBN: 98123807101.

[16] J. Schechter and J. W. F. Valle, "Neutrinoless double-β decay in SU(2)$\times$U(1) theories," *Phys. Rev. D*, vol. 25, pp. 2951–2954, Jun 1982.

[17] I. Avignone, Frank T., S. R. Elliott, and J. Engel, "Double Beta Decay, Majorana Neutrinos, and Neutrino Mass," *Rev. Mod. Phys.*, vol. 80, pp. 481–516, 2008, 0708.1033.

[18] A. Strumia and F. Vissani, "Neutrino masses and mixings and.," 2006, hep-ph/0606054.

[19] I. Ogawa *et al.*, "Search for neutrino-less double beta decay of Ca-48 by CaF-2 scintillator," *Nucl. Phys.*, vol. A730, pp. 215–223, 2004.

[20] H. V. Klapdor-Kleingrothaus *et al.*, "Latest Results from the Heidelberg-Moscow Double Beta Decay Experiment," *Eur. Phys. J.*, vol. A12, pp. 147–154, 2001, hep-ph/0103062.

[21] H. V. Klapdor-Kleingrothaus, I. V. Krivosheina, A. Dietz, and O. Chkvorets, "Search for neutrinoless double beta decay with enriched 76Ge in Gran Sasso 1990-2003," *Phys. Lett.*, vol. B586, pp. 198–212, 2004, hep-ph/0404088.

[22] R. Arnold *et al.*, "First results of the search of neutrinoless double beta decay with the NEMO 3 detector," *Phys. Rev. Lett.*, vol. 95, p. 182302, 2005, hep-ex/0507083.

[23] R. Arnold *et al.*, "Double beta decay of Zr-96," *Nucl. Phys.*, vol. A658, pp. 299–312, 1999.

[24] F. A. Danevich *et al.*, "Search for 2 beta decay of cadmium and tungsten isotopes: Final results of the Solotvina experiment," *Phys. Rev.*, vol. C68, p. 035501, 2003.

[25] C. Arnaboldi *et al.*, "Results from a search for the $0\nu\beta\beta-$decay of ^{130}Te," *Phys. Rev.*, vol. C78, p. 035502, 2008, 0802.3439.

[26] R. Bernabei *et al.*, "Investigation of beta beta decay modes in Xe-134 and Xe-136," *Phys. Lett.*, vol. B546, pp. 23–28, 2002.

[27] . J. Argyriades, "Measurement of the Double Beta Decay Half-life of 150-Nd and Search for Neutrinoless Decay Modes with the NEMO-3 Detector," 2008, 0810.0248.

[28] J. Menendez, A. Poves, E. Caurier, and F. Nowacki, "Deformation and the Nuclear Matrix Elements of the Neutrinoless Double Beta Decay," 2008, 0809.2183.

[29] F. T. Avignone, G. S. King, and Y. G. Zdesenko, "Next generation double-beta decay experiments: Metrics for their evaluation," *New J. Phys.*, vol. 7, p. 6, 2005.

[30] N. Scielzo *et al.*, "Double beta decay Q-values of ^{130}Te, ^{128}Te, and ^{120}Te," *Physical Review C*, vol. 80, no. 2, 2009.

[31] S. R. Elliott and P. Vogel, "Double beta decay," *Ann. Rev. Nucl. Part. Sci.*, vol. 52, pp. 115–151, 2002, hep-ph/0202264.

[32] C. E. Aalseth *et al.*, "The Igex 76ge Neutrinoless Double-Beta Decay Experiment: Prospects for Next Generation Experiments," *Phys. Rev.*, vol. D65, p. 092007, 2002, hep-ex/0202026.

[33] A. Staudt, K. Muto, and H. V. Klapdor-Kleingrothaus, "Calculation of 2nu and 0nu double-beta decay rates," *Europhys. Lett.*, vol. 13, pp. 31–36, 1990.

[34] H. V. Klapdor-Kleingrothaus, A. Dietz, H. L. Harney, and I. V. Krivosheina, "Evidence for Neutrinoless Double Beta Decay," *Mod. Phys. Lett.*, vol. A16, pp. 2409–2420, 2001, hep-ph/0201231.

[35] R. Arnold *et al.*, "Technical design and performance of the NEMO 3 detector," *Nucl. Instrum. Meth.*, vol. A536, pp. 79–122, 2005, physics/0402115.

[36] V. A. Rodin, A. Faessler, F. Simkovic, and P. Vogel, "Assessment of uncertainties in QRPA 0nu beta beta-decay nuclear matrix elements," *Nucl. Phys.*, vol. A766, pp. 107–131, 2006, 0706.4304.

[37] I. Abt *et al.*, "A new Ge-76 double beta decay experiment at LNGS," 2004, hep-ex/0404039.

[38] V. E. Guiseppe *et al.*, "The Majorana Neutrinoless Double-Beta Decay Experiment," 2008, 0811.2446.

[39] R. Gaitskell *et al.*, "White paper on the Majorana zero-neutrino double-beta decay experiment," 2003, nucl-ex/0311013.

[40] C. Arnaboldi *et al.*, "CUORE: A cryogenic underground observatory for rare events," *Nucl. Instrum. Meth.*, vol. A518, pp. 775–798, 2004, hep-ex/0212053.

[41] R. Ardito *et al.*, "CUORE: A cryogenic underground observatory for rare events," 2005, hep-ex/0501010.

[42] F. Piquemal, "The SuperNEMO project," *Phys. Atom. Nucl.*, vol. 69, pp. 2096–2100, 2006.

[43] M. Danilov *et al.*, "Detection of very small neutrino masses in double-beta decay using laser tagging," *Phys. Lett.*, vol. B480, pp. 12–18, 2000, hep-ex/0002003.

[44] M. K. Moe, "New approach to the detection of neutrinoless double-beta decay," *Phys. Rev.*, vol. C44, pp. 931–934, 1991.

[45] E. Fiorini and T. O. Niinikoski, “Low temperature calorimetry for rare decays,” *Nucl. Instr. Meth.*, vol. A224, p. 83, 1984.

[46] A. Alessandrello *et al.*, “New experimental results on double beta decay of Te-130,” *Physics Letters B*, vol. 486, pp. 13–21, 2000.

[47] N. F. Mott and J. H. Davies, “Metalinsulator transition in doped semiconductors,” *Philosophical Magazine B*, vol. 42, pp. 845–858, 1980.

[48] A. Miller and E. Abrahams, “Impurity conduction at low concentrations,” *Physical Review*, vol. 120, pp. 745–755, 1960.

[49] K. M. Itoh et al., “Neutron transmutation doping of isotopically engineered Ge,” *Applied Physics Letters*, vol. 64, pp. 2121–2123, 1994.

[50] C. Arnaboldi, G. Pessina, and E. Previtali, “A programmable calibrating pulse generator with multi- outputs and very high stability,” *IEEE Trans. Nucl. Sci.*, vol. 50, pp. 979–986, 2003.

[51] C. Arnaboldi *et al.*, “The programmable front-end system for CUORICINO, an array of large-mass bolometers,” *IEEE Trans. Nucl. Sci.*, vol. 49, pp. 2440–2447, 2002.

[52] C. Arnaboldi *et al.*, “A Calorimetric Search on Double Beta Decay of 130Te,” *Phys. Lett.*, vol. B557, pp. 167–175, 2003, hep-ex/0211071.

[53] V. A. Rodin, A. Faessler, F. Šimkovic, and P. Vogel, “Erratum: Assessment of uncertainties in QRPA $o\nu\beta\beta$-decay nuclear matrix elements,” 2007, 0706.4304v1 [nucl-th]. `0706.4304v1 [nucl-th]`.

[54] M. Kortelainen and J. Suhonen, “Nuclear matrix elements of neutrinoless double beta decay with improved short-range correlations,” *Physical Review C*, vol. 76, p. 024315, 2007, 0708.0115 [nucl-th]. `0708.0115 [nucl-th]`.

[55] A. Alessandrello *et al.*, “An electrothermal model for large mass bolometric detectors,” *IEEE Transactions On Nuclear Science*, vol. 40, no. 4, pp. 649–656, 1993.

[56] M. Abramowitz and I. A. Stegun, *Handbook of Mathematical Functions with Formulas, Graphs, and Mathematical Tables.* New York: Dover, ninth dover printing, tenth gpo printing ed., 1964.

[57] W. H. Press, S. A. Teukolsky, W. T. Vetterling, and B. P. Flannery, *Numerical recipes in C (2nd ed.): the art of scientific computing.* New York, NY, USA: Cambridge University Press, 1992.

[58] E. Gatti and P. F. Manfredi, “Processing the signals from solid state detectors in elementary particle physics,” *Riv. Nuovo Cim.*, vol. 9N1, pp. 1–146, 1986.

[59] A. Alessandrello *et al.*, “The bolometers as nuclear recoil detectors,” *Nuclear Instruments and Methods in Physics Research Sec.A*, vol. 409, pp. 451–453, May 1998.

[60] B. P. Demidovitch and I. Maron, *Éléments de calcul numérique.* Ed. Mir, 1973.

[61] Wikipedia, "2009 l'aquila earthquake," April 2009.